

UCSF

UC San Francisco Electronic Theses and Dissertations

Title

Development of Three-Compartment Breast Imaging for Clinical Applications in Dual Energy X-ray Absorptiometry

Permalink

<https://escholarship.org/uc/item/9ht12182>

Author

Avila, Jesus Ismael

Publication Date

2018

Peer reviewed|Thesis/dissertation

Development of Three-Compartment Breast Imaging for Clinical Applications in Dual Energy X-ray Absorptiometry

by

Jesus Ismael Avila

DISSERTATION

submitted in partial satisfaction of the requirements for the degree of

DOCTOR OF PHILOSOPHY

in

BIOENGINEERING

in the

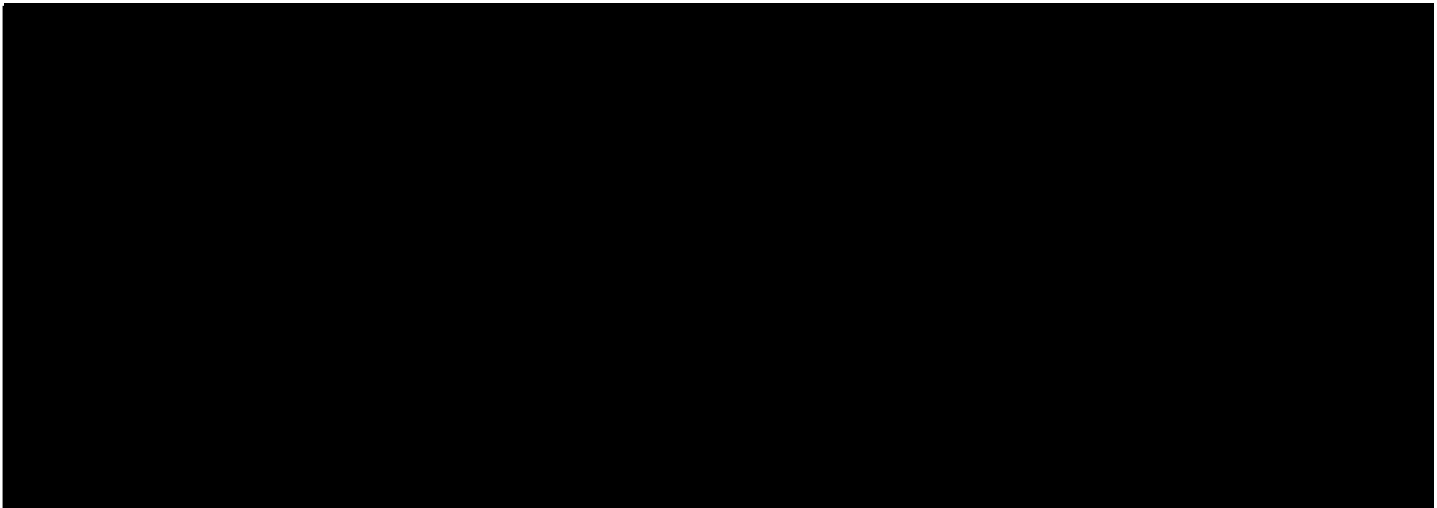
GRADUATE DIVISION

of the

UNIVERSITY OF CALIFORNIA, SAN FRANCISCO

AND

UNIVERSITY OF CALIFORNIA, BERKELEY



Dedication

This work is the collection of the countless number of folks who supported me throughout my life; the list would be too long.

- **To Dr. Dennis Lee Portis:** for inspiring my curiosity in engineering, mentoring me, and believing in me. You will always be missed.
- **To Major Fennell:** thank you for mentoring at-risk youth. You changed my life.
- **To my brother and sister:** thank you for bringing so much joy to my life.
- **To my second family, the Vices:** thank you for sharing your love.
- **To my uncle, Joel:** for your creative methods of motivation during my teenage years.
- **To my mom,** who always put her family first: you are my hero.
- **To my wife, Nikky:** you're my best friend. Thank you for your unending warmth.
- **To my labmates, Bennet, Lisa, Ben, Bo, Leila, Serghei, Pasha, *et al.*:** thank you for your support and the countless laughs.
- **To my PI, Dr. John A. Shepherd:** thank you for always pushing and believing in me, and thank you for all the engineering techniques I learned in your lab.

I would like to especially thank the funding sources that made my research possible: the **National Institutes of Health Individual Predoctoral Fellowships to Promote Diversity in Health-Related Research (F31)**, supplement to **NIH Research Project Grant Program (R01)**.

Acknowledgements

Parts of this dissertation are reprints of publications, which are listed below. The co-authors listed below directed and supervised the research that forms the basis for the dissertation/thesis.

1. Avila, J.I, Malkov, S., Giger, M.L., Drukker, K., and Shepherd, J.A., 2018. Energy dependence of dual-energy mammography calibration. *Medical Physics*, *In Review*.

JIA helped design and conduct the research, analyze data, draft the manuscript, and review and approve the final manuscript.

2. Avila, J., Malkov, S., Giger, M., Drukker, K. and Shepherd, J.A., 2016, June. Energy Dependence of Water and Lipid Calibration Materials for Three-Compartment Breast Imaging. In *International Workshop on Digital Mammography* (pp. 554-563). Springer, Cham.

JIA helped design and conduct the research, analyze data, draft the manuscript, and review and approve the final manuscript.

3. Xie, B.*, Avila, J.I.*, Ng, B.K., Fan, B., Loo, V., Gilsanz, V., Hangartner, T., Kalkwarf, H.J., Lappe, J., Oberfield, S. and Winer, K., 2015. Accurate body composition measures from whole-body silhouettes. *Medical physics*, 42(8), pp.4668-4677.

*Co-first author

JIA helped design and conduct the research, analyze data, draft the manuscript, and review and approve the final manuscript.

I also contributed to the following papers during my graduate studies:

1. Drukker, K., Giger, M.L., Joe, B.N., Kerlikowske, K., Greenwood, H., Drukteinis, J.S., Niell, B., Fan, B., Malkov, S., Avila, J.I., Kazemi, L, and Shepherd, J.A., 2018. Combined benefit of quantitative three-compartment breast image analysis and mammography radiomics in the classification of breast masses on clinical dataset. *Radiology*.

JIA helped conduct the research and analyze data, and review and approve the final manuscript.

2. Drukker, K., Huynh, B.Q., Giger, M.L., Malkov, S., Avila, J.I., Fan, B., Joe, B., Kerlikowske, K., Drukteinis, J.S., Kazemi, L. and Pereira, M.M., 2017, March. Deep learning and three-compartment breast imaging in breast cancer diagnosis. In *Medical Imaging 2017: Computer-Aided Diagnosis* (Vol. 10134, p. 101341F). International Society for Optics and Photonics.

JIA helped conduct the research and analyze data, and review and approve the final manuscript.

3. Malkov, S., Avila, J., Fan, B., Joe, B., Kerlikowske, K., Giger, M., Drukker, K., Drukteinis, J., Kazemi, L., Pereira, M. and Shepherd, J., 2016, June. Calibration

procedure of three component mammographic breast imaging. In *International Workshop on Digital Mammography* (pp. 211-218). Springer, Cham.

JIA helped design and conduct the research, analyze data, and review and approve the final manuscript.

4. Drukker, K., Malkov, S., Avila, J., Kerlikowske, K., Joe, B., Krings, G., Creasman, J., Drukteinis, J.S., Pereira, M.M., Kazemi, L. and Shepherd, J., 2016, March. Identification, segmentation, and characterization of microcalcifications on mammography. In *Medical Imaging 2016: Computer-Aided Diagnosis* (Vol. 9785, p. 97850S). International Society for Optics and Photonics.

JIA helped conduct the research and analyze data, and review and approve the final manuscript.

Abstract

Development of Three-Compartment Breast Imaging for Clinical Applications in Dual Energy X-ray Absorptiometry

by

Jesus Ismael Avila

Problem

Approximately 75% of the breast cancer biopsies performed after recommendations from diagnostic mammography are benign, making it clear that specificity for diagnostic mammography still needs significant improvements. A novel three-compartment breast (3CB) composition technique developed by Laidevant *et al.* seeks to improve the specificity of diagnostic digital mammography, but it is prone to estimate incorrect compositional estimates for patient lesions. The focus of this thesis was to further develop this three-compartment technique for clinical applications in dual-energy X-ray imaging modalities.

Methods

Three potential sources of error in the 3CB technique were studied: (1) attenuation coefficient differences in biological materials—for which 3CB is estimating compositional estimates—and their calibration equivalents, (2) nonuniformities in full-field digital mammography (FFDM) from X-ray source spectra, and (3) initial intensity I_0 differences between biological and calibration images. Initial developments for 3CB applications in digital breast tomosynthesis were also investigated, and these were in two areas: (1) dose measurements and estimates were made for high energy 3CB digital breast tomosynthesis (DBT) images and (2) derivation of potential variables of interest as predictors of breast thickness from raw DBT projections. Lastly, a novel technique for measuring body composition from 2D optical images to help monitor and

maintain healthy body weight was investigated, which could potentially aid in monitoring adipose and muscular tissues to monitor and maintain a lean weight to reduce risk of cancer for postmenopausal women in low-resource settings.

Results

To reduce error in the attenuation coefficient differences between biological and calibration materials, linear mappings were created using bovine and chicken phantoms. This linear mapping corrected negative 3CB compositional estimates in a population study. To reduce error in nonuniformities in FFDM source spectra, polynomial flat-fielding models were created. These reduced nonuniformities to at or below imaging noise levels. To reduce I_0 differences between biological and calibration images, two I_0 correction models made it possible to obtain similar log-signal values between breast and calibration images.

To make the 3CB applicable to DBT, two areas were investigated. Firstly, dose measurements and estimates were made for HE 3CB DBT images. It was found that a copper filter of 0.4064 mm (16 mils) seems to be optimal in terms of meeting dose requirements, availability, and CNR. In addition, imaging at 71 mAs seems to optimize CNR while satisfying dose requirements. Secondly, investigations sought to derive potential variables of interest as predictors of breast thickness from raw DBT projections. It was found that variables derived from sinograms could be potentially useful in estimating breast thickness from raw DBT projections.

The last topic discussed in this thesis focused on developing a novel body composition technique from optical images. This proof-of-concept study showed that it

may be possible to determine fat mass index, fat-free mass index, and percent-fat from 2D optical images.

Conclusion

Two of the three major works in this study advanced the 3CB imaging technique to become more clinically practical in dual-energy absorptiometry applications. The last focus of this thesis may make it easier to monitor body composition in low-resource settings.

Abbreviations

2CCP	Two-Compartment Calibration Phantom	DXA	Dual-Energy X-ray Absorptiometry
2CIP	Two-Compartment Intermediate Phantom	FFDM	Full-field Digital Mammography
3CB	Three-Compartment Breast	FFMI	Fat-Free Mass Index
AGD	Average Glandular Dose	FMI	Fat Mass Index
ASM	Active Shape Model	Gd	Gadolinium
BCT	Breast Computed Tomography	HE	High Energy
BIA	Bioelectrical Impedence Analysis	HVL	Half-Value Layer
BIRADS	Breast Imaging Reporting and Data System	kVp	Peak kiloVolts
BMDCS	Bone Mineral Density in Children Study	LE	Low Energy
BMI	Body Mass Index	mAs	milliAmps-seconds
BMIZ	BMI Z-scores	MGD	Mean Glandular Dose
CDMAM	Contrast Detail Mammography	MRI	Magnetic Resonance Imaging
CE	Contrast-Enhanced	NCI	National Cancer Institute
CEM	Contrast-enhanced Mammography	NICHD	National Institute for Children's Health and Diseases
CIRS	Computer Imaging Reference Systems	PCA	Principal Component Analysis
CNR	Contrast-to-Noise Ratio	PPV	Positive Predictive Value
CT	Computed Tomography	RMSE	Root-Mean-Squared Error
Cu	Copper	RMSEN	Normalized RMSE
DBT	Digital Breast Tomosynthesis	RMSEP	Percent RMSE
DC	Direct Current	SBC	Schwarz Bayesian criterion
DE-CEDM	Dual-energy Contrast-Enhanced Digital Mammography	SE	Standard Error
		SEER	Surveillance, Epidemiology, and End Results Program
		SXA	Single X-ray Absorptiometry
		WLP	Water, Lipid, Protein

Table of Contents

Chapter 1 Background	1
Breast Cancer	1
Breast Cancer Screening with X-ray Mammography	2
Limitations of X-ray Mammography.....	3
Potential Solutions to Limitations	4
Contrast-Enhanced Mammography.....	4
Magnetic Resonance Imaging and Ultrasound.....	5
Breast CT and Tomosynthesis	5
Dual-Energy X-ray Imaging	6
Three-Compartment Compositional Imaging	7
Chapter 2 Energy dependent considerations: measuring three components of tissue for cancer lesion quantification	8
Introduction.....	8
Monoenergetic Case.....	9
Polyenergetic Case.....	12
Polyenergetic Case and Varying kVp	13
Application	14
Methods.....	15
Population.....	15
Oil & Water Validation Experiment	15
3CB Images and Bovine Calibration.....	16

Phantoms.....	17
Results	19
Population Description.....	19
Corrections with Biological Phantoms	20
Oil Experiments	34
Population Corrections	36
Discussion	38
Chapter 3 Studies on Other Error Sources	41
Flat-Fielding.....	41
Methods	41
Results.....	43
Discussion	49
Initial Intensity (I_0) Correction	51
Methods	51
Results.....	52
Discussion	59
Chapter 4 3CB Tomosynthesis	60
Introduction.....	60
Part I: Optimizing filter and imaging parameters for high-energy projections.....	61
Methods	62
Results.....	64

Discussion	71
Part II: Methodology for determining 3D breast thickness from tomosynthesis projections	72
Methods	72
Results	75
Discussion	79
Chapter 5 Accurate body composition estimates from whole-body silhouettes	80
Introduction.....	80
Methods.....	83
Participants	83
DXA acquisition	83
Silhouette images	85
Active Shape Modeling	85
Statistics	89
Results	90
Discussion	96
Chapter 6 Future Directions.....	99
Chapter 7 Conclusions.....	101
References.....	103
Appendix A: Code Availability	114

List of Tables

Table 2.1 Demographics of study participants.....	20
Table 2.2 Composition of Bovine Phantom tissue samples by % weight and volume	21
Table 2.3 Bovine Phantom regions of interest compositions with estimated water, lipid, protein, and mineral ash components from laboratory analysis.	21
Table 2.4 Composition of Chicken Phantom tissue samples by % weight and volume	21
Table 2.5 Chicken Phantom regions of interest compositions with estimated water, lipid, protein, and mineral ash components from laboratory analysis.	22
Table 2.6 The matrix multiplication for each input vector is shown.....	25
Table 3.1 Scanner settings for BR50/50 CIRS phantoms for flat-fielding model	42
Table 3.2 Compositions of the two-compartment phantoms for testing the empirical <i>I0</i> model .	53
Table 4.1 Imaging Parameters for CNR Images	69
Table 5.1. Summary statistics of the test population separated by sex.	90
Table 5.2. Correlation of the most significant principal components with demographic and adiposity variables (R^2).....	92
Table 5.3 Prediction equations, R^2 adj. (see definition below table), and root-mean-square error (RMSE), for demographic variables, FFMI, FMI and Percent Fat from PCA modes and demographic information using the boys' data.	93
Table 5.4. Prediction equations, R^2 adj. (see definition below table), and root-mean-square error (RMSE), for demographic variables, FFMI, FMI and Percent Fat from PCA modes and demographic information using the girls' data.	94

List of Figures

Figure 2.1 The mammogram, water, lipid, and protein images of a breast sample are shown. These are derived using the 3CB method described above. The annotation outlined by a radiologist is also shown in each figure, along with three concentric regions spaced 2 mm apart.	17
Figure 2.2 The 51-point calibration phantom is shown on the left, and an X-ray projection of it is shown on the right. An X-ray projection of the SXA phantom is also shown on the right.....	18
Figure 2.3 The bovine phantom is shown on the left and its corresponding X-ray projection is shown on the right. This phantom was used to create a linear map between the 51-point CP and biological materials.	19
Figure 2.4 The chicken phantom is shown on the left and its corresponding X-ray projection is shown on the right.	19
Figure 2.5 This shows the different elements of the transfer function, a 3x3 matrix B , from calibration material space to bovine space as a function of kVp. Most of the elements are constant, but elements b_{31} , b_{32} , and b_{33} —which scale the protein vector P in the matrix multiplication—vary as a function of kVp.....	23
Figure 2.6 The chicken phantom transfer function components. This shows the different elements of the transfer function, a 3x3 matrix B , from calibration material space to chicken space as a function of kVp.	24
Figure 2.7 Bovine phantom ROI water thickness estimates vs. actual for each kVp. The top shows the estimates using only the calibration phantom, and the bottom plot shows estimates after a linear correction (3x3 matrix) was applied using data from the top plot.....	26
Figure 2.8 Bovine phantom ROI lipid thickness estimates vs. actual for each kVp. The top shows the estimates using only the calibration phantom, and the bottom plot shows estimates after a linear correction (3x3 matrix) was applied using data from the top plot.....	27

Figure 2.9 Bovine phantom ROI protein thickness estimates vs. actual for each kVp.
The top shows the estimates using only the calibration phantom, and the bottom plot shows estimates after a linear correction (3x3 matrix) was applied using data from the top plot.....28

Figure 2.10 Chicken phantom ROI water thickness estimates vs. actual for each kVp.
The top shows the estimates using only the calibration phantom, and the bottom plot shows estimates after a linear correction (3x3 matrix) was applied using data from the top plot.....29

Figure 2.11 Chicken phantom ROI water thickness estimates vs. actual for each kVp.
The top shows the estimates using only the calibration phantom, and the bottom plot shows estimates after a linear correction (3x3 matrix) was applied using data from the top plot.....30

Figure 2.12 Chicken phantom ROI water thickness estimates vs. actual for each kVp.
The top shows the estimates using only the calibration phantom, and the bottom plot shows estimates after a linear correction (3x3 matrix) was applied using data from the top plot.....31

Figure 2.13 The 3CB water thickness estimate for the fifteen ROIs of the bovine phantom are shown before and after linear correction was applied.....32

Figure 2.14 The 3CB lipid thickness estimate for the fifteen ROIs of the bovine phantom are shown before and after linear correction was applied.33

Figure 2.15 The 3CB protein thickness estimate for the fifteen ROIs of the bovine phantom are shown before and after linear correction was applied.33

Figure 2.16 The estimated lipid thicknesses for different regions of interest (ROIs), pre- and post-bovine correction.35

Figure 2.17 Estimated water, lipid, and protein thickness distributions of sampled population. The top figure shows distributions before and after bovine model corrections, and the bottom figure shows these for the chicken model corrections.	37
Figure 3.1 Flat-fielding surface fits for kVp = 29 (Mo/Mo anode/filter combinations), 1 cm (top plots) and 8 cm (bottom plots). For 1 cm plots, $\sigma_{SDN} = 0.59\%$, $RMSEN = 0.36\%$. For 8 cm plots, $\sigma_{SDN} = 0.83\%$, $RMSEN = 0.68\%$	45
Figure 3.2 Flat-fielding surface fits for kVp = 32 (Mo/Rh anode/filter combinations), 1 cm (top plots) and 8 cm (bottom plots). For 1 cm plots, $\sigma_{SDN} = 0.79\%$, $RMSEN = 0.43\%$. For 8 cm plots, $\sigma_{SDN} = 1.06\%$, $RMSEN = 0.76\%$	46
Figure 3.3 Flat-fielding surface fits for kVp = 39 (Mo/Rh-Al anode/filters combinations), 1 cm (top plots) and 8 cm (bottom plots). For 1 cm plots, $\sigma_{SDN} = 1.53\%$, $RMSEN = 0.44\%$. For 8 cm plots, $\sigma_{SDN} = 2.22\%$, $RMSEN = 1.32\%$	47
Figure 3.4 Flat-fielding plots of σ_{SDN} and $RMSEN$ for 1 cm (top) and 8 cm (bottom) surface fits as a function of kVp.	48
Figure 3.5 Flat-fielding model coefficients for 29 kVp. Linear interpolation was used to create flat-fielding values for all thicknesses between 1 and 8 cm, so the “Fit Curve” directly overlays over the plot of the surface fit coefficient values.	49
Figure 3.6 The ROI sample location for the empirical I_0 model.	53
Figure 3.7 R vs. HE Plots of two-compartment phantoms before the empirical I_0 model was applied.	54
Figure 3.8 R vs. HE Plots of two-compartment phantoms before the empirical I_0 model was applied.	55
Figure 3.9 Located SXA ROIs phantom for estimating I_0 from the SXA phantom log-signal values.	56
Figure 3.10 LE calibration phantom and breast I_0 derived from SXA phantom.	57

Figure 3.11 HE calibration phantom and breast I_0 derived from SXA phantom	58
Figure 4.1 A projection of the GEN3 phantom showing sampled regions of interest.....	64
Figure 4.2 LE and HE AGD estimates for a 4 cm thick, 50 % glandularity breast for the first set of AGD measurements.	65
Figure 4.3 HVL estimation plots (air kerma vs. aluminum thickness) for first set of AGD measurements.....	66
Figure 4.4 LE and HE AGD estimates for 2, 4, and 6 cm thick, 50 % glandularity breasts for the second set of AGD measurements.	68
Figure 4.5 HVL estimation plots (air kerma vs. aluminum thickness) for second set of AGD measurements.....	69
Figure 4.6 The CNR and Normalized CNR for varying breast thicknesses.	71
Figure 4.7 ASTRA toolbox experiment imaging geometry and parameters.....	73
Figure 4.8 Example sinograms of a simple breast phantom for CT and DBT simulations. (a), (b), and (c) show the top, side, and front views of the geometry of the object. (d) shows a sinogram made from a simulated CT scan with 59 projections over a sweep angle $\theta = 180^\circ$ ($d\theta = 3.125^\circ$). (e) shows a sinogram made from a simulated DBT scan with 9 projections over a sweep angle $\theta = 25^\circ$ ($d\theta = 3.125^\circ$).	74
Figure 4.9 Cross-sectional view and sinogram of simple a breast object of varying thickness (top thickness = 20 mm, bottom thickness = 60 mm).	76
Figure 4.10 RMSE of a pre-selected breast sinogram and generated sinograms of varying breast parameters.	77
Figure 4.11 The RMSE between a sinogram of random breast parameters and a library of sinograms for an iterative method.	78
Figure 4.12 (Top) Breast sinograms of randomly generated thickness, diameter, and intensity parameters and (Bottom) the error between actual and iteratively-found estimates...	79

Figure 5.1. (left) Image of the high-energy attenuation portion of the DXA scan. Bone and the density of soft tissue can clearly be distinguished as shades of grey. (right) Silhouette representation of the same DXA image.....84

Figure 5.2. Delineation of 50 points of interest on silhouettes for active shape modeling.85

Figure 5.3. Silhouette representations of the first 10 (i.e. 0 to 9) modes used to model FFMI in both boys and girls. The average silhouette is shown in the middle and the silhouettes representing -3SD (left) and +3SD (right) are also shown.88

Figure 5.4. Comparison between FMI (top), FFMI (middle), and percent fat (bottom) values acquired from DXA scans and predicted by the PCA models constructed from silhouettes with boys (left) and girls (right).95

Chapter 1 Background

Breast Cancer

Worldwide, breast cancer is the second leading cause of cancer deaths, accounting for 11.6% of total cancer deaths. An estimated 6.6 million people will die from breast cancer in 2018.[1] “There is no treatment,” an ancient Egyptian text dating to about 3000 B.C. says about the disease.[2] Details of surgical intervention were first documented in the 1st century AD by Leonides of Alexandria.[3] More treatment options—such as endocrine surgery[4], radiation, and chemotherapy—became available in the 20th century, ushering a better outlook for patients.[5] Today, the overall average five-year and ten-year survival rates for breast cancer in the USA are 91% and 86%, respectively.[6] In the USA, breast cancer mortality has decreased from 32 per 100,000 to 21 per 100,000 from 1975 to 2010. Along with these advancements, however, overdiagnosis has now become a topic of interest in recent years, and many challenges remain before the fight against breast cancer is considered finished.

Breasts have milk-producing lobules that are interconnected through a tubular system of ducts. These lobules and ducts are embedded in the breast’s fatty tissue, and the ducts terminate at a reservoir just behind the nipple. Approximately 80% of breast cancers originate within the ducts and the remaining 20% within the lobules.[7] The precursor to breast cancer is thought to be an abnormal growth in either lobular or ductal cells, known as atypical hyperplasia. In a study published in 2007 that included over 9,000 women and 331 atypical hyperplasia cases, it was found that women who

have either atypical lobular hyperplasia or atypical ductal hyperplasia “have a lifetime risk of breast cancer that is about four times higher than that of women who don't have atypical hyperplasia.”[8] If this abnormal growth progresses, it can become invasive and affect normal human physiology, which can ultimately lead to death.

Breast Cancer Screening with X-ray Mammography

The first randomized prospective trial of breast cancer, and cancer in general, was conducted by the Health Insurance Plan of New York in 1963.[9] From this study and up until 2011, a total of more than 650,000 women have been part of several randomized prospective breast screening trials. Not without controversy, researchers have agreed that breast cancer screening reduces mortality for certain age groups (“15% for women aged 39-49 years, 14% for women aged 50-59, and 32% for women aged 60-69 years, with corresponding numbers needed to invite to screening to prevent 1 breast cancer death of 1,904, 1,339, and 377, respectively”). These trials were made possible with the development of a new mammography technique—since prior techniques had yielded poor image quality—introduced by Robert Egan and his colleagues in 1960.[10]

Today, breast cancer screening conducted by health care institutions is dependent on radiographic sources such as X-ray, ultrasound, and magnetic resonance. Though physical examination is also conducted, typical screening programs rely mostly on X-ray sources, because of the combination of its lower relative cost over MRI and higher specificity over ultrasound.[11] From 2015 data, over 65% of U.S. women aged 40 and over have had a mammogram within the past two years, and

approximately 22.6 million patients had a mammographic procedure within the past year.[12, 13] It is because of breast cancer's complexity, as it is in other cancers, that fights against it have turned to early detection and diagnosis, hoping to stop before it metastasizes. According to the National Cancer Institute's (NCI) Surveillance, Epidemiology, and End Results Program (SEER), the five-year survival rates for localized, regional (spread to regional lymph nodes), distant (cancer has metastasized) are 98.7%, 85.3%, and 27.0%, respectively. Today, X-ray screening mammography has become the standard of care. For women in the US, screening mammography is recommended to start at age 40 by the American College of Radiology (2010) and American College of Obstetricians and Gynecologists (2011).[14] Other major USA organizations recommend starting at either age 45 or 50. In other countries, this age is typically 50.[15]

Limitations of X-ray Mammography

As far as X-ray screening mammography performance, its sensitivity ranges from 83% to 95%; its specificity ranges from 90% to 98%.[16] For *diagnostic* X-ray mammography, the sensitivity was 85.8% and specificity was 87.7%. Although it has high specificity, approximately 75% of women who undergo biopsies after an initial finding during diagnostic mammography are benign, making it clear that specificity for diagnostic mammography still needs significant improvements.[17]

During a mammography exam, radiologist search for abnormalities in breast texture (e.g., spiculations), objects that resemble tumors, shape differences between the two breasts, and change in breast images over time.[18] Calcifications, or

microcalcifications, are often the only sign of breast cancer because tumors only have mild changes in the X-ray attenuation coefficient.[19] The X-ray attenuation coefficient of calcifications is higher, however, than fibroglandular and adipose tissues, so they appear bright in X-ray mammography images. Even so, it can be difficult to find microcalcifications in dense breast [20-22], reducing the sensitivity of mammography.

Potential Solutions to Limitations

To address some of the limitations of mammography, other imaging modalities and techniques have been used in conjunction with X-ray mammography. These are discussed here.

Contrast-Enhanced Mammography

Some advanced applications in digital X-ray mammography have sought to improve contrast between lesions and fibroglandular tissue. One such application is contrast-enhanced mammography (CEM). Contrast-enhanced techniques rely on the biological principle of tumoral angiogenesis.[23] Malignant vessels are more permeable to contrast agents, increasing contrast between tumors and their surrounding tissues.[24, 25] Iodine is used intravenously in all CEM techniques.[26] Although CEM techniques can have high sensitivity (pooled test sensitivity of 0.98, 95% CI: 0.96-1.00 for contrast-enhanced spectral mammography), specificity is typically low (0.58, 95% CI: 0.38 – 0.77). In addition to low specificity, another limitation to CEM techniques is adverse reactions to iodine, which can vary from renal impairment to life-threatening anaphylactic shock.[26, 27]

Magnetic Resonance Imaging and Ultrasound

Some non-ionizing imaging modalities are used as supplements to digital X-ray mammography. Contrast-enhanced magnetic resonance Imaging (MRI) for diagnostic imaging has been shown to have 94% sensitivity.[28, 29] Moreover, "...annual screening with MRI and mammography using a BI-RADS score of 4 or 5 to define positivity is currently the most accurate means of screening women with a strong familial or genetic predisposition to breast cancer. Limitations of MRI, however, include high cost, low availability, and relatively low specificity.

Ultrasonography has shown a higher sensitivity than mammography for diagnostic imaging, especially in high-density breasts.[30] In one study, diagnostic accuracy for digital mammography plus ultrasound was reported as 0.91 (95% CI, 0.84-0.96), while this figure was 0.78 (95% CI, 0.67-0.87) for digital mammography alone.[31] While diagnostic accuracy improved, the number of false positives substantially increased as well.

Breast CT and Tomosynthesis

Computed tomography (CT) is an imaging modality that acquires projections of an object to reconstruct its corresponding 3D volume. Individual 2D image "slices" can be viewed along any axis of the reconstructed volume. Although CT has been used in clinical practice since the 1970s, the first clinical trials for breast CT (BCT) happened in the past decade. BCT allows detection of lesions that could otherwise go undetected because of masking from dense fibroglandular tissues. A 2017 review of initial clinical trials of breast CT in Europe found that non-contrast breast CT and contrast-enhanced breast CT "was superior to mammography for the visualization of breast masses,

especially in patients with dense breast tissue.[32] The reported dose for breast CT in the studies was comparable to X-ray mammography dose, a mean glandular dose (MGD) of 9.4 mGy (SD = 3.1 mGy) for breast CT and 16.9 mGy (SD = 6.9 mGy) for digital X-ray mammography, though the number of views taken for X-ray mammography ranged from 2 to 11 breast.[33] In another study by Seifert *et al.*, the MGD was 10.7 mGy (SD = 3.0 mGy) for breast CT and 9.7 mGy (SD = 5.3. mGy) for digital X-ray mammography.

Digital breast tomosynthesis (DBT) has also seen increased research efforts in the past couple of decades, but it has garnered much more attention over BCT. DBT is similar to CT in that it creates a reconstructed volume by capturing X-ray projections across a sweep angle, but this sweep angle is typically smaller than 50°. This creates a pseudo-3D volume with individual “slices” in the z-direction (the axis perpendicular to the detector plane) but with blurred artifacts from objects outside the focal plane. Studies have similar or improved sensitivity and specificity over digital X-ray mammography (see 3CB Tomosynthesis for more details about DBT).

Dual-Energy X-ray Imaging

Dual-energy techniques rely on acquiring low energy (LE) and high-energy (HE) images to either improve contrast between tissues or for compositional measurements. A study with dual-energy contrast-enhanced digital mammography (DE-CEDM) found that the sensitivity of digital mammography alone was 0.80 (standard error = 0.04) while digital mammography plus DE-CEDM had sensitivity of 0.93 (SE = 0.03). For specificity, these were 0.50 (SE = 0.06) for digital mammography alone and 0.56 (SE = 0.06) for digital mammography plus DE-CEDM.

Three-Compartment Compositional Imaging

While the above imaging techniques have addressed some limitations of screening and diagnostic digital mammography, specificity still needs to be improved to reduce the number of unnecessary biopsies. One technique that has been developed recently uses a three-compartment model of the breast to determine breast composition and lesion characterization.[34] This novel technique resolves dual energy images, along with a third measurement of breast thickness, to create water, lipid, and protein thickness estimates at every pixel. This method is the focus of much of the rest of this dissertation. The long-term goal of this work is to improve the specificity of diagnostic digital mammography. While this technique can be easily adapted to diagnostic digital mammography scanners, many technical challenges exist. For example, initial estimates of lesion compositions sometimes yielded negative thickness estimates for the compartments, which is physically unreasonable. The focus of this dissertation is to further develop this three-compartment technique by addressing the errors needing to be resolved before clinical application of the method can be realized.

Chapter 2 Energy dependent considerations: measuring three components of tissue for cancer lesion quantification

Introduction

Measuring the mass or volume of a tissue while it is surrounded by similar tissues is a difficult problem for X-ray imaging methods. X-ray attenuation alone cannot isolate one tissue from another with similar characteristics. Edge detection allows for delineation but not the density or composition of the organ. Dual-energy X-ray tissue composition imaging techniques can quantify the unique composition of organs using the unique energy dependence of materials to enable separation of two masses in digital images. Examples of this technique include contrast-enhanced (CE) digital subtraction mammography[35], Dual-energy X-ray absorptiometry (DXA)[36], CE digital breast tomosynthesis[37], and dual-energy CT[38], which all operate on different X-ray peak energy bands. As Lehmann *et al.* mention, the physical phenomena that allow two materials to be solved using X-ray energies available in medical imaging are the photoelectric effect and Compton scattering.[39] Any material can be characterized by its photoelectric and Compton coefficients, a_p and a_c . Compositional images can be made by calibrating phantoms that have similar or equivalent coefficients and solving for their thicknesses. High and low X-ray energy images are acquired to capture these phenomena, typically acquired at fixed X-ray tube voltages because the attenuation coefficients are energy dependent. However, there are situations where one may want to use arbitrary high and low X-ray energies. This introduces complexity and practical difficulty in solving for the two biological materials, such as a three compartment breast

technique developed by Laidevant *et al.*[34, 40] Here, we outline the general solutions for dual-energy compositional imaging, outline calibration issues for practical devices, and outline one solution to the problem of arbitrary X-ray energies.

Monoenergetic Case

The simplest case for dual energy imaging is the use of a single-energy photon sources such as radioactive materials with monoenergetic emission, and gadolinium (Gd) has been used in medical imaging applications. Gd is unique in that it outputs two monochromatic emissions, X and Y. Using a discriminator, one can acquire monoenergetic attenuation signals simultaneously. Thus, all X-ray photons used for an image acquisition have the same energy. Concerning the composition of humans, water, lipid, and protein account for approximately 99% of the mass of many soft tissues.[41] Glycogen is mostly found in skeletal muscle and liver, and it accounts for approximately “1% and 2.2% of their respective wet weights in the form of glycogen.”[41-43] The remaining component, mineral ash, is mostly found in bone. It is often convenient, therefore, for certain X-ray compositional imaging techniques to assume that soft tissues are composed of only water, lipid, and protein. For a three-component material, the resulting intensity I is

$$I = I_0 e^{-(\mu_1(E_0)t_1 + \mu_2(E_0)t_2 + \mu_3(E_0)t_3)} \quad \text{Equation 2-1}$$

where μ_i for $i = 1, 2, 3$ is the linear attenuation coefficient for a particular material and is approximated by the equation

$$\mu_i = (a_{pi}f_p + a_{ci}f_c)\rho_i, \quad \text{Equation 2-2}$$

where ρ_i is the density of the material. As stated by Lehmann *et al.*, “ a_p and a_c are characteristic constants of the material and f_p and f_c are the energy dependencies of photoelectric absorption and Compton scattering, respectively.” In the log-signal form,

$$A(E_0) = -\ln\left(\frac{I}{I_0}\right) = \mu_1(E_0)t_1 + \mu_2(E_0)t_2 + \mu_3(E_0)t_3 \quad \text{Equation 2-3}$$

The total thickness of the material T is the sum of the component materials:

$$T = t_1 + t_2 + t_3 \quad \text{Equation 2-4}$$

Individual component thicknesses can be solved by acquiring a low energy (mostly a photoelectric effect with some Compton scattering) and a high-energy image (captures less of the photoelectric effect and more Compton scattering) using a system of linear equations. In matrix form we get

$$\boldsymbol{\mu} \mathbf{t} = \mathbf{A}, \text{ where} \quad \text{Equation 2-5}$$

$$\boldsymbol{\mu} = \begin{bmatrix} \mu_{1,LE} & \mu_{2,LE} & \mu_{3,LE} \\ \mu_{1,HE} & \mu_{2,HE} & \mu_{3,HE} \\ 1 & 1 & 1 \end{bmatrix}, \quad \mathbf{t} = \begin{bmatrix} t_1 \\ t_2 \\ t_3 \end{bmatrix}, \quad \mathbf{A} = \begin{bmatrix} A_{LE} \\ A_{HE} \\ T \end{bmatrix}$$

Solving for \mathbf{t} we get

$$\mathbf{t} = \boldsymbol{\mu}^{-1} \mathbf{A}. \quad \text{Equation 2-6}$$

If the attenuation coefficient values are known for the materials and energies, then with the measurement of overall tissue thickness T and LE and HE log-signals (A_{LE} and A_{HE}), the individual material thicknesses can be solved. However, the exact attenuation properties of tissue are often not known, and the attenuation coefficient

values need to be solved empirically. This is often using a calibration object with materials that represent the tissues of interests. The calibration materials are never the exact composition of the body tissues they represent and introduce errors in approximating the thickness of the body tissues. These errors, represented as ϵ_p and ϵ_c in the characteristic constants of a material, modify the attenuation coefficients in the following way:

$$\mu'_i = (\epsilon_{pi}a_{pi}f_p + \epsilon_{ci}a_{ci}f_c)\rho_i \quad \text{Equation 2-7}$$

Since ϵ_{pi} and ϵ_{ci} are fixed for each calibration material and component pair, μ'_i will also have a fixed total error ϵ_{Ti} such that μ'_i is a scaled version of μ_i , i.e.

$$\mu'_i = \epsilon_{Ti}\mu_i. \quad \text{Equation 2-8}$$

If the error ϵ_{Ti} is known, then the correct thickness estimates for the biological materials can be solved using linear coefficients of the calibration materials, so having an error creates a linear transformation between the two material spaces (biological and calibration). Deriving the correct thicknesses for biological materials in the monoenergetic case is straightforward, but in practice, X-ray systems have polyenergetic X-ray tubes. X-ray tubes typically have both sharp emissions at particular energies such as k-shell edges, but the dominant emission is often from Bremsstrahlung radiation—created from electrons losing kinetic energy as they decelerate when near the nucleus of an atom—and have, from inception, varying energies.[44] In the next section, we expand Equation 2-7 to include polyenergetic X-ray sources.

Polyenergetic Case

For the polyenergetic case, the entire spectrum must be considered; thus, our log-signal function for LE and HE becomes

$$A_j(E) = -\frac{I(E)}{I_0(E)} = \frac{\int I_0(E)e^{\mu_1(E)t_1 + \mu_2(E)t_2 + \mu_3(E)t_3} dE}{\int I_0(E)dE} \quad \text{Equation 2-9}$$

This cannot be solved analytically, but compartment thickness t_i can be modeled by a nonlinear function of energy and total thickness.[34, 39, 45]

$$t_i = \sum_{\alpha, \beta, \gamma \in N} b_{\alpha\beta\gamma, i} A_{HE}^\alpha R^\beta T^\gamma, \text{ where} \quad \text{Equation 2-10}$$

$R = \frac{A_{LE}}{A_{HE}}$ is the ratio of log-signal functions of low and high energies,
 $b_{\alpha\beta\gamma, i}$ is a coefficient of each term in the infinite series for each material i .

For a quadratic solution (degree two), we have the following:

$$t_i = a_{1, i} + a_{2, i}A_{HE} + a_{3, i}R + a_{4, i}T + a_{5, i}A_{HE}^2 + a_{6, i}R^2 + a_{7, i}T^2 \\ + a_{8, i}A_{HE}R + a_{9, i}A_{HE}T + a_{10, i}RT \quad \text{Equation 2-11}$$

Since the total thickness is known, one need only derive thicknesses—and thus the calibration coefficients $b_{\alpha\beta\gamma, i}$ —for two materials (and solve for the third algebraically).

Each term in the polynomial that has A_{HE} or R will have an error associated with material differences between biological and calibration materials, since these terms contain the linear attenuation coefficient μ_i . The linear attenuation coefficient for the polyenergetic case is as follows:

$$\mu_i(E) = (a_{pi}f_p(E) + a_{ci}f_c(E))\rho_i \quad \text{Equation 2-12}$$

And it follows, for calibration materials, that

$$\mu'_i(E) = (\epsilon_{pi}a_{pi}f_p(E) + \epsilon_{ci}a_{ci}f_c(E))\rho_i \quad \text{Equation 2-13}$$

It is important to note that although the errors ϵ_{pi} and ϵ_{ci} are *still* energy independent—since the photoelectric and Compton coefficients a_p and a_c are energy independent—the total error total error ϵ_{Ti} is not; thus, we have

$$\mu'_i(E) = \epsilon_{Ti}(E)\mu_i(E), \text{ where} \quad \text{Equation 2-14}$$

$$\mu'_i(E) = \frac{(\epsilon_{pi}a_{pi}f_p(E) + \epsilon_{ci}a_{ci}f_c(E))}{(a_{pi}f_p(E) + a_{ci}f_c(E))} \mu_i(E)$$

This error, of course, affects the solution for each material thickness t_i . A map, therefore, is needed to transform incorrect material thickness values t'_i to t_i , such that

$$t_i = T[t'_i]$$

Though mapping has been performed for breast composition in dual-energy mammography for determining calcification thickness and glandular ratio by Kappadath and Shaw, only two materials were considered.[46]

Polyenergetic Case and Varying kVp

This case is similar to the polyenergetic one but with varying LE kVp acquisitions. For full-field digital mammography (FFDM) scanners, for example, images are typically acquired in the 24-32 kVp range. The map between the two material spaces would need to be made for each kVp that is used to minimize the error between material spaces. Recently, Laidevant *et al.* developed a dual energy X-ray imaging method that uses a three-compartment breast model (3CB) to characterize tissue composition.[47] The 3CB

method represents breast tissue as the equivalent composition of the phantom materials—Delrin, Plastic Water®, and machinable wax. The 3CB model is derived by acquiring three measurements: a low-energy image, a high-energy image, and the total thickness of the breast at each pixel. By generating images of the water, lipid, and protein (WLP) content of the breast, it may be possible to get a characteristic signature of malignant and benign lesions. Drukker *et al.* recently used this technique in conjunction with breast morphometry features for classifying lesions and found improved classification vs. either technique alone.[48] Additionally, Malkov *et al.* found compositional differences in lesion classifications.[49]

Application

The 3CB technique relies on calibration materials for biological equivalents of lipid, water, and protein. Though compositional estimates have been made for breasts using the 3CB technique, there were negative protein estimates. This could be attributed to errors described above, since the relationship between actual breast tissue compartments of lipid, water, and protein differ from the phantom. We have modeled in a previous study that the major source of error could be attributed to energy-dependent differences between the calibration materials and their biological equivalents.[50] In this study, we derive a calibration method to correct for thickness errors using a biological phantom. We validate this method with lipid and water experiments, and we test its effect by applying it to participant data.

Methods

Population

Participants were part of the “Lesion Composition and Quantitative Imaging Analysis on Breast Cancer Diagnosis” investigator-initiated study to characterize the composition of invasive breast cancer lesions (R01CA166945, PIs Shepherd/Giger). Participants were recruited from women undergoing breast biopsy (BIRADS 4 or 5) to have additional diagnostic imaging. Images of the participant were acquired before their biopsy procedure. The following exclusion criteria were used: prior breast cancer, prior breast interventions (e.g., previous breast biopsy), breast alterations, and mammographically occult findings. Study radiologists delineated the breast lesions on the LE craniocaudal and mediolateral oblique views. From these delineations, compositional measures were derived using the area inside the delineation and the immediate periphery.[51] This study was approved by UCSF’s Institutional Review Board.

Oil & Water Validation Experiment

The purpose of this experiment is to show if the 3CB technique is energy independent; if so, 3CB thickness estimates of a sample should be the same regardless of the kVp of the LE image. A blue wax step phantom was placed inside a container and filled with canola oil until the total thickness of the oil reached 30 mm. A similar procedure was done for Plastic Water® and distilled water. These containers represented the lipid and water compartments, respectively. Images were acquired at 27 kVp and 30 kVp for both containers. The 3CB method was applied to different ROIs in the images, which

represented 0, 33, 50, and 67 % calibration material and 100, 67, 50, and 33 % canola oil or distilled water.[52]

3CB Images and Bovine Calibration

Hologic (Hologic, Inc., Bedford, MA) full-field digital mammography scanners were used to acquire the LE and HE images. A thickness map of the breast was then derived using the single X-ray absorptiometry (SXA) phantom. The 3CB technique was then applied to derive the three compositional thickness images—lipid, water, and protein (Figure 2.1). A bovine-derived affine transformation was then applied to these thickness images to correct for calibration material differences. The transformation is applied as follows:

$$[W' \quad L' \quad P'] = [W \quad L \quad P]B(kVP), \text{ where} \quad \text{Equation 2-15}$$

$$B = \begin{bmatrix} b_{11} & b_{12} & b_{13} \\ b_{21} & b_{22} & b_{23} \\ b_{31} & b_{32} & b_{33} \end{bmatrix},$$

and W , L , and P are initial water, lipid, and protein estimates from a 51-point calibration phantom. The elements b_{ij} of the affine transformation were derived using the least-squares fit between $[W' L' P']$ and $[W L P]$ from a bovine phantom of known composition.

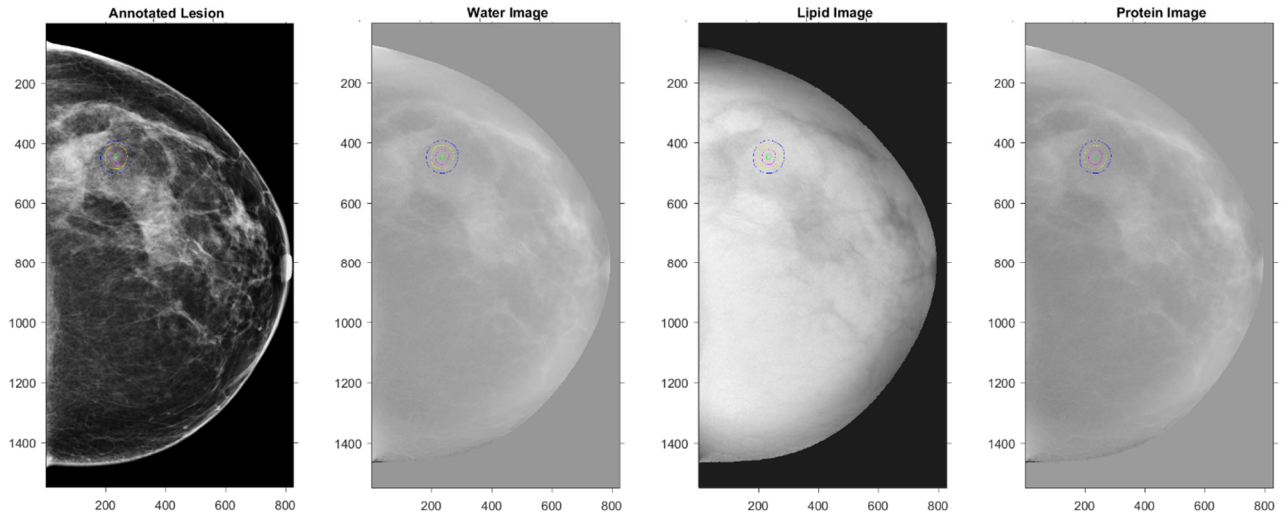


Figure 2.1 The mammogram, water, lipid, and protein images of a breast sample are shown. These are derived using the 3CB method described above. The annotation outlined by a radiologist is also shown in each figure, along with three concentric regions spaced 2 mm apart.

Phantoms

SXA Phantom

The SXA phantom was used to estimate the thickness of the breasts under compression, regardless of paddle tilt.[53] The phantom was placed near one of the corners of the field of view such that it would not interfere with the breast area in the image. A least-squares technique was used to locate the phantom and estimate paddle tilt, and from these a thickness map was generated for breasts at each pixel.

51-Point Calibration Phantom

This phantom contains the three calibration materials for lipid, water, and protein—blue wax, Plastic Water®, and Delrin (Figure 2.2). This is the main 3CB calibration phantom, and it contains 51 unique WLP regions of interests (ROIs). This phantom is used to derive the calibration coefficients $a_{\alpha\beta\gamma,i}$, and corresponding images are taken of the phantom for each breast that is imaged. The same imaging parameters as the breast

were used for the phantom LE and HE images. Most of the phantom was manufactured with fabrication tools in-lab, and a portion of it was fabricated by a local machine shop.

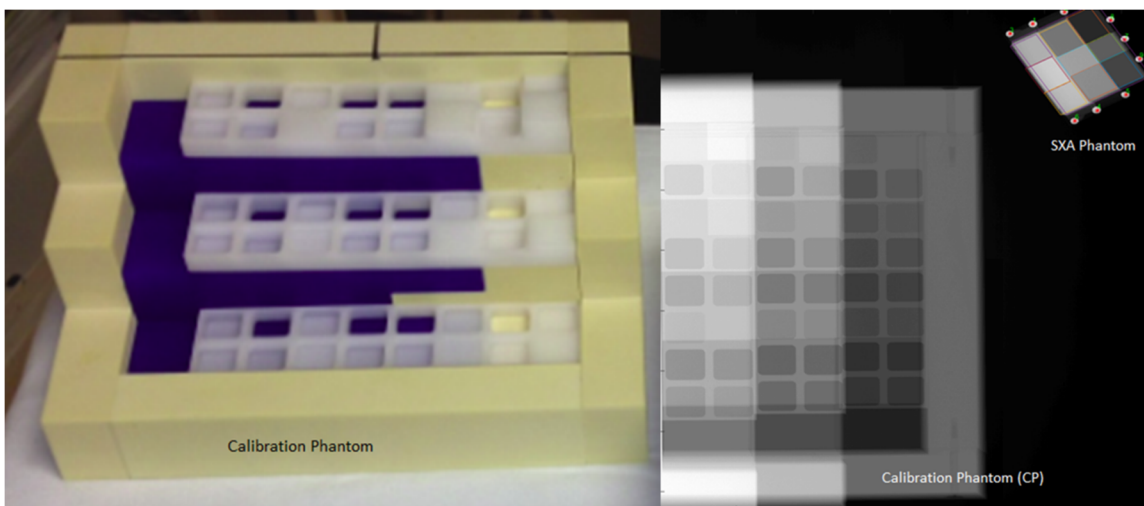


Figure 2.2 The 51-point calibration phantom is shown on the left, and an X-ray projection of it is shown on the right. An X-ray projection of the SXA phantom is also shown on the right.

Bovine and Chicken Phantoms

The bovine and chicken phantoms had 15 ROIs. Bovine lean muscle and suet were combined into volumetric fractions of 0.0/1.0, 0.25/0.75, 0.5/0.5, 0.75/0.25, and 1.0/0.0 for different ROIs. The total thickness for each “step” of the phantom was 2, 4, and 6 cm. As for the chicken phantom, LE images were acquired at varying kVp (25 – 32 kVp) to match the energy levels of breast images. Samples were sent to Anresco Laboratories (San Francisco, CA) for chemical composition analyses.

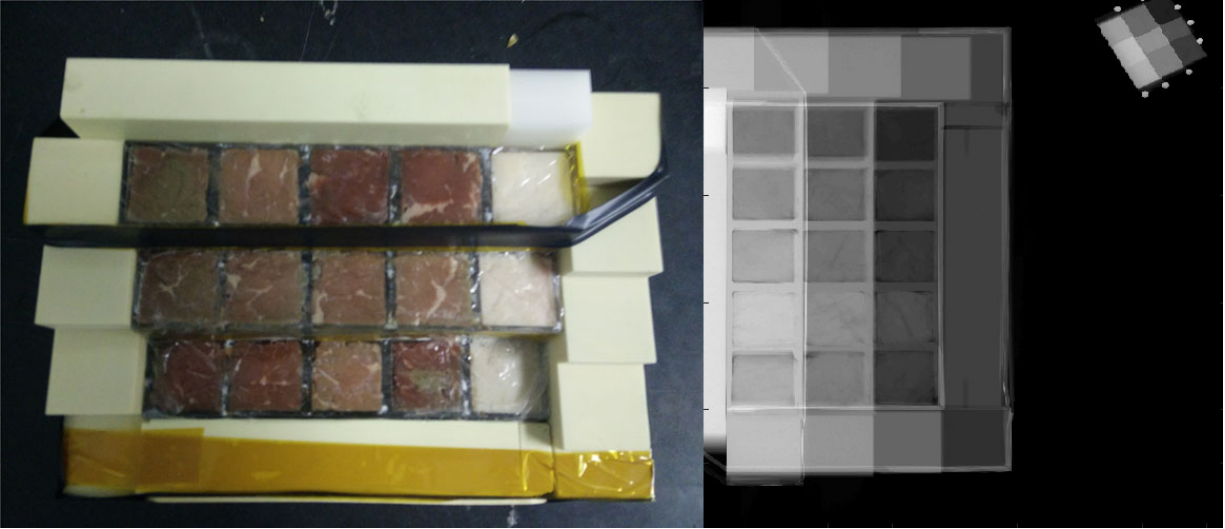


Figure 2.3 The bovine phantom is shown on the left and its corresponding X-ray projection is shown on the right. This phantom was used to create a linear map between the 51-point CP and biological materials.

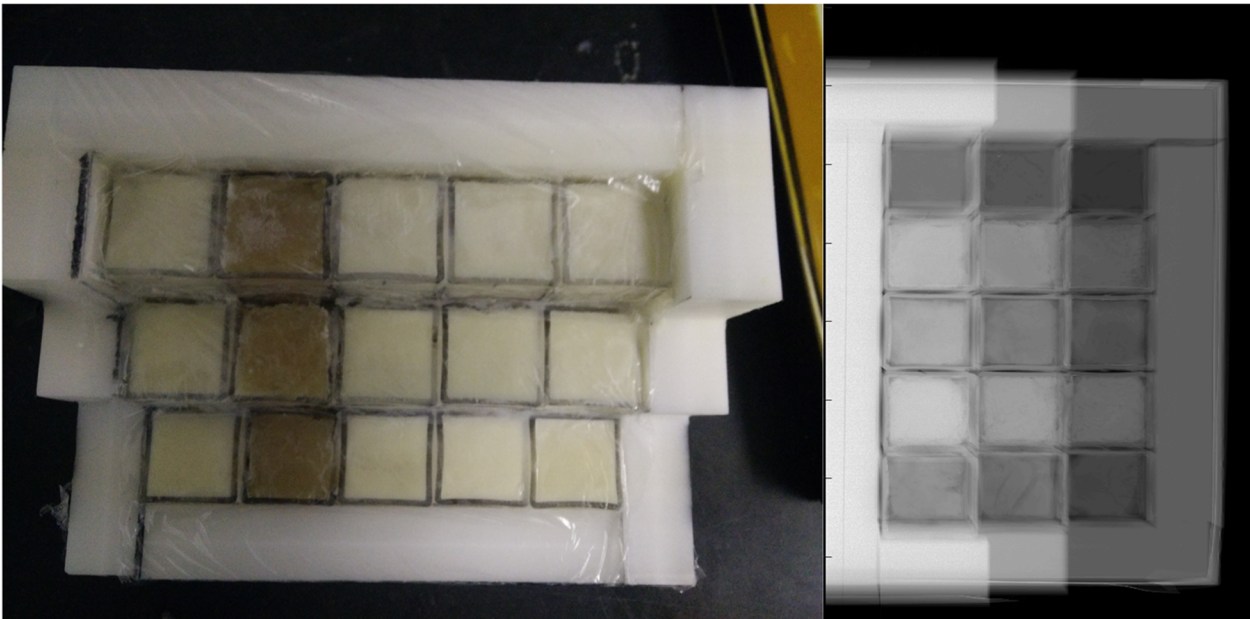


Figure 2.4 The chicken phantom is shown on the left and its corresponding X-ray projection is shown on the right.

Results

Population Description

The bovine correction was also applied to a set of participants. Demographics of these participants are shown in Table 2.1. One of the participants was removed since

no estimate could be created, so a total of 80/81 patients had compositional estimates created.

Table 2.1 Demographics of study participants.

	N	%
Number of Women Imaged at each kVp		
kVp = 25	4	4.94
kVp = 26	2	2.47
kVp = 27	5	6.17
kVp = 28	15	18.52
kVp = 29	7	8.64
kVp = 30	13	16.05
kVp = 31	8	9.88
kVp = 32	27	33.33
Total	81	100
Breast Density		
A=Almost entirely fatty	5	6.17
B=Scattered fibroglandular densities	29	35.8
C=Heterogeneously dense	39	48.15
D=Extremely dense	39	9.88
Total	81	100
Age	53.91 ± 9.92	
Height	64.65 ± 2.74	
Weight	150.46 ± 31.6	
BMI	25.3 ± 5.13	

Corrections with Biological Phantoms

The composition results of the bovine phantom samples are shown in Table 2.2 and Table 2.3. Composition results for the chicken phantom are in Table 2.4 and Table 2.5.

Table 2.2 Composition of Bovine Phantom tissue samples by % weight and volume

Component	Density used for Conversion (g/cm ³)	Bovine Composition by % Weight	Bovine Composition by % Volume	Suet Composition by % Weight	Suet Composition by % Volume
Water	1	70.03	75.04	11.90	11.11
Lipid	0.92	4.44	5.17	86.52	87.83
Protein	1.35	24.50	19.45	1.50	1.04
Mineral Ash	3.2	1.03	0.34	0.08	0.02

Table 2.3 Bovine Phantom regions of interest compositions with estimated water, lipid, protein, and mineral ash components from laboratory analysis.

Region of Interest	Total ROI Thickness (mm)	Percent Density (%)*	Water thickness (mm)	Lipid Thickness (mm)	Protein Thickness (mm)	Mineral Ash Thickness (mm)
1	60.50	0.00	6.72	53.13	0.63	0.01
2	40.20	0.00	4.47	35.31	0.42	0.01
3	20.20	0.00	2.24	17.74	0.21	0.00
4	60.50	21.49	15.03	42.39	3.02	0.06
5	40.30	36.72	13.94	23.16	3.14	0.06
6	20.20	34.65	6.72	11.95	1.50	0.03
7	60.50	51.24	26.54	27.51	6.33	0.11
8	40.20	53.23	18.15	17.62	4.36	0.08
9	20.20	48.02	8.45	9.72	2.00	0.04
10	60.50	100.00	45.40	3.13	11.76	0.21
11	40.20	100.00	30.17	2.08	7.82	0.14
12	20.20	100.00	15.16	1.04	3.93	0.07
13	60.40	60.93	30.24	22.63	7.40	0.13
14	40.20	64.68	21.09	13.82	5.20	0.09
15	20.10	66.17	10.74	6.66	2.66	0.05

*Density is defined as the meat thickness/total thickness*100

Table 2.4 Composition of Chicken Phantom tissue samples by % weight and volume

Component	Density used for Conversion (g/cm ³)	Gallus Composition by % Weight	Gallus Composition by % Volume	Tallow Composition by % Weight	Tallow Composition by % Volume
Water	1	75.04	80.88	0	0
Lipid	0.92*	0.06	0.07	100	100
Protein	1.35	23.09	18.44	0	0
Mineral Ash	3.2	1.81**	0.61	0	0

*Although Tallow density = 0.87, this does not affect Tallow conversion since it is 100% lipid

**Mineral Ash content includes 0.63 % total carbohydrates

Table 2.5 Chicken Phantom regions of interest compositions with estimated water, lipid, protein, and mineral ash components from laboratory analysis.

Region of Interest	Total ROI Thickness (mm)	Percent Density (%)*	Water thickness (mm)	Lipid Thickness (mm)	Protein Thickness (mm)	Mineral Ash Thickness (mm)
1	69.14	0.00	0.00	69.14	0.00	0.00
2	48.77	0.00	0.00	48.77	0.00	0.00
3	29.41	0.00	0.00	29.41	0.00	0.00
4	69.14	75.20	42.05	17.18	9.59	0.32
5	48.77	77.97	30.76	10.77	7.01	0.23
6	29.41	67.27	16.00	9.64	3.65	0.12
7	69.14	61.54	34.41	26.62	7.84	0.26
8	48.77	51.30	20.24	23.77	4.61	0.15
9	29.41	50.78	12.08	14.49	2.75	0.09
10	69.14	100.00	55.92	0.05	12.75	0.42
11	48.77	100.00	39.45	0.03	8.99	0.30
12	29.41	100.00	23.79	0.02	5.42	0.18
13	69.14	29.90	16.72	48.48	3.81	0.13
14	48.77	29.17	11.50	34.55	2.62	0.09
15	29.41	24.01	5.71	22.36	1.30	0.04

*Density is defined as the meat thickness/total thickness*100

Figure 2.5 shows how different element values of the affine transformation B vary as a function of kVp. By going through the matrix multiplication, we can observe how B maps the WLP vectors between the calibration material and bovine spaces. For W , the water vector, the corresponding elements that affect its transformation are b_{11} , b_{21} , and b_{31} , yielding the new vector $W' = b_{11}W + b_{21}L + b_{31}P$. Figure 2.6 shows similar plots but for the chicken phantom. For the chicken phantom, it appears that most of the energy-dependent variation of the elements occur at the lower energy levels.

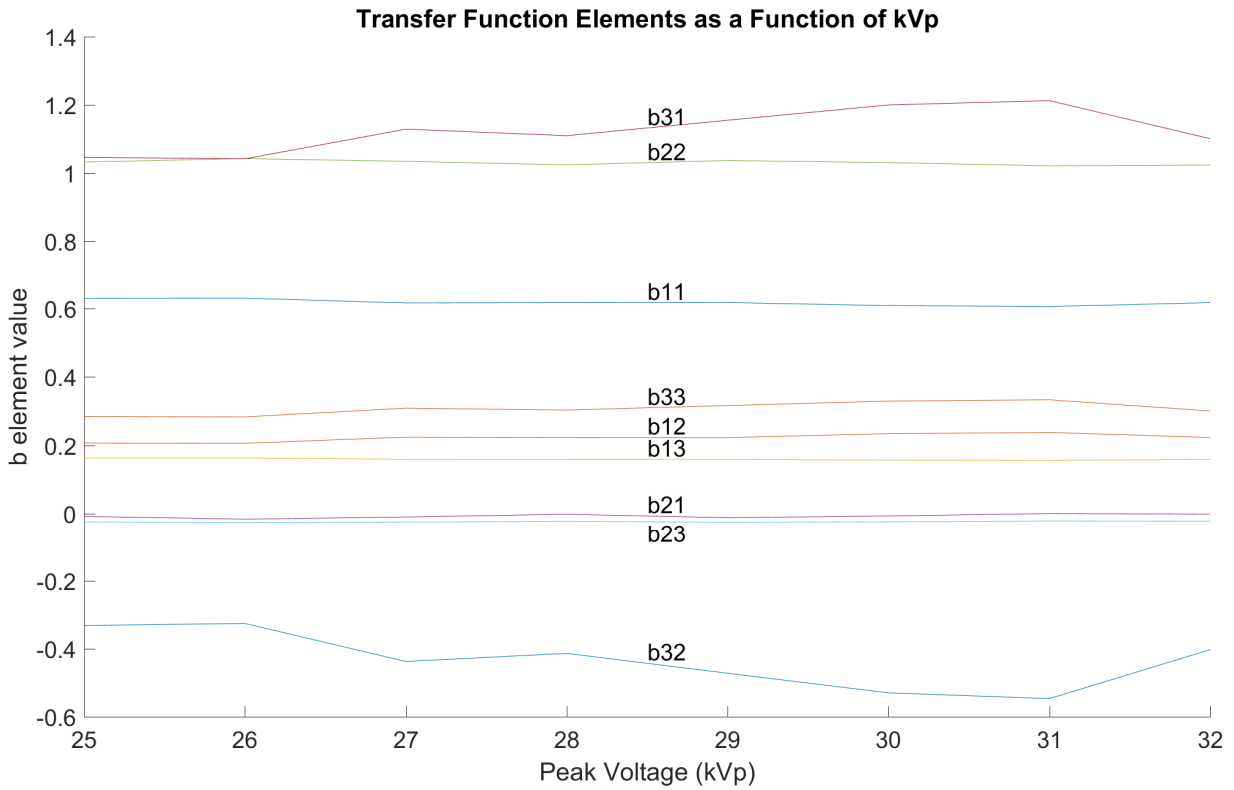


Figure 2.5 This shows the different elements of the transfer function, a 3x3 matrix B , from calibration material space to bovine space as a function of kVp. Most of the elements are constant, but elements b_{31} , b_{32} , and b_{33} —which scale the protein vector P in the matrix multiplication—vary as a function of kVp.

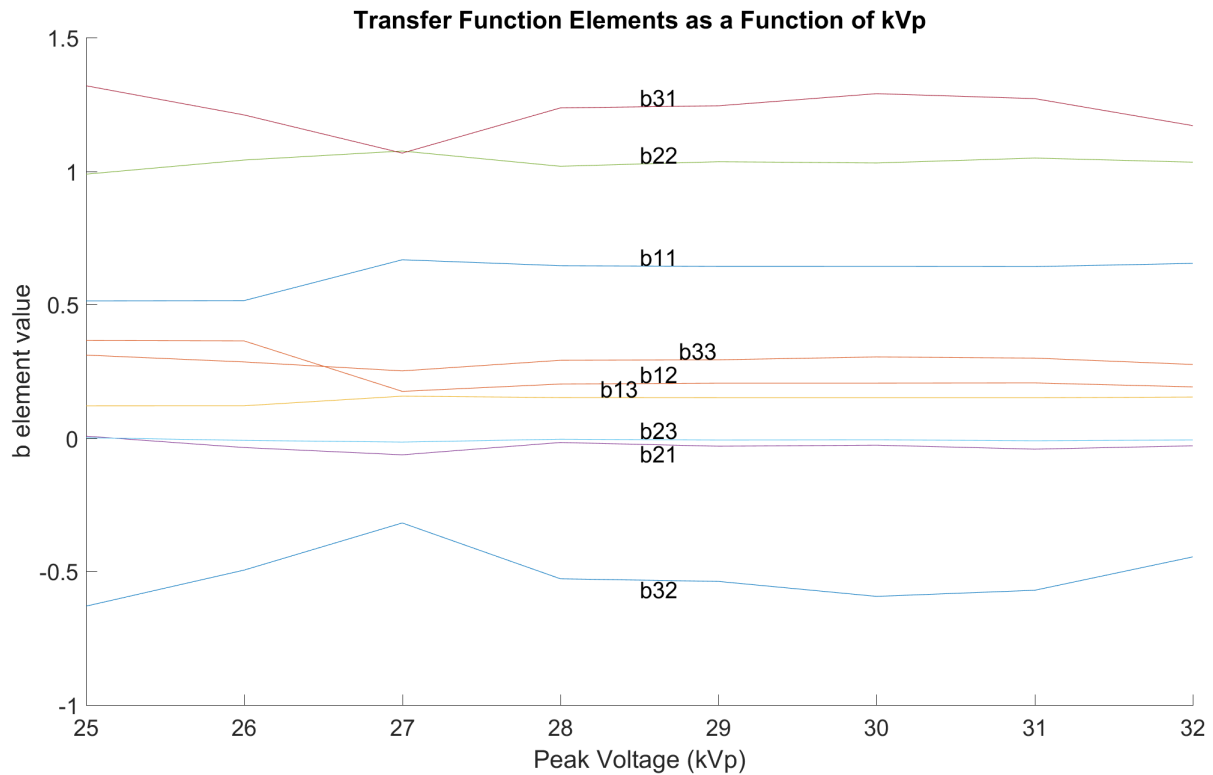


Figure 2.6 The chicken phantom transfer function components. This shows the different elements of the transfer function, a 3x3 matrix B , from calibration material space to chicken space as a function of kVp.

Table 2.6 shows the equation form of the matrix multiplication. For the bovine phantom: for W' , the water contribution W is reduced, L doesn't contribute, and protein contributes but to a lesser extent (since protein is about factor lower than W and the range for b_{31} is approximately 1.05 – 1.21). For L' , W plays a contribution and is approximately constant, L is almost the unit value, and P is multiplied by a negative number (range of b_{32} is approximately -0.55 – -0.33). For P' , W is scaled at a similar value as the water contribution for L' (~0.16), L slightly contributes, and P is also varies over the kVp range (range of b_{33} is approximately 0.28 – 0.33). In all three equations, protein seems to be the most energy dependent while the other components can be

replaced by constants. For the chicken phantom, the protein component P' seems to be a constant equation for all kVps, while W' and L' vary as a function of kVp.

Table 2.6 The matrix multiplication for each input vector is shown.

Input Vector	3x3 Matrix Multiplications	Bovine Multiplications (simplified form)	Chicken Multiplications (simplified form)
W	$W' = b_{11}(kVp)W + b_{21}(kVp)L + b_{31}(kVp)P$	$W' \approx 0.63W + 0.0L + b_{31}(kVp)P$	$W' = b_{11}(kVp)W + b_{21}(kVp)L + b_{31}(kVp)P$
L	$L' = b_{12}(kVp)W + b_{22}(kVp)L + b_{32}(kVp)P$	$L' \approx 0.24W + 1.02L + b_{32}(kVp)P$	$L' = b_{12}(kVp)W + b_{22}(kVp)L + b_{32}(kVp)P$
P	$P' = b_{13}(kVp)W + b_{23}(kVp)L + b_{33}(kVp)P$	$P' \approx 0.16W - 0.02L + b_{33}(kVp)P$	$P' \approx 0.15 + 0.0L + 0.29P$

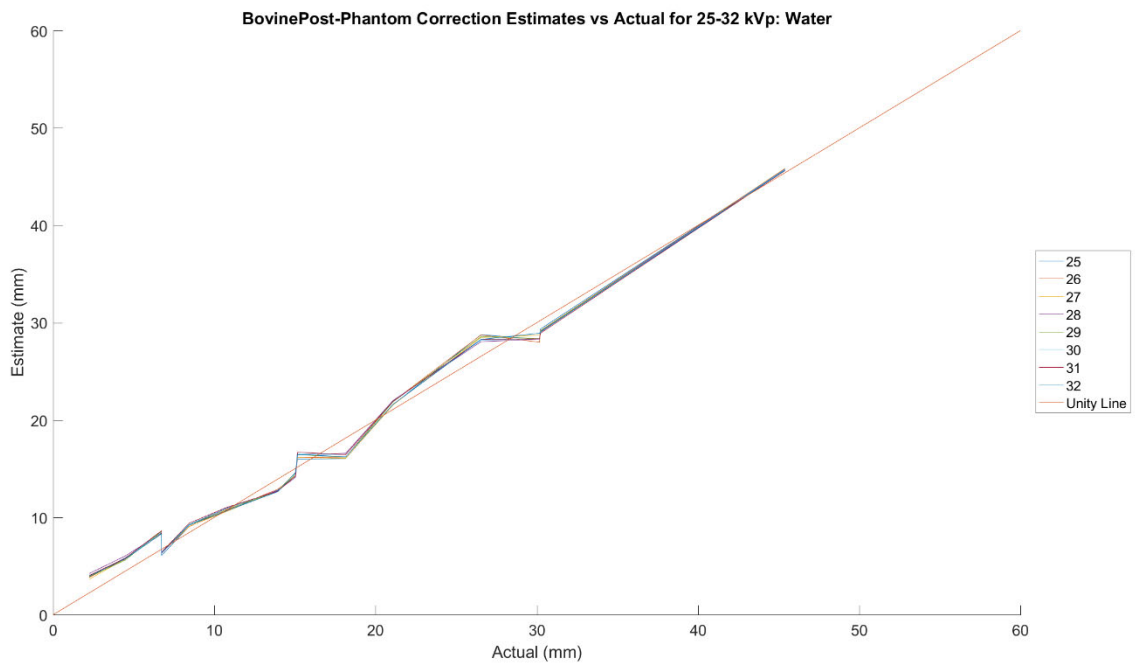
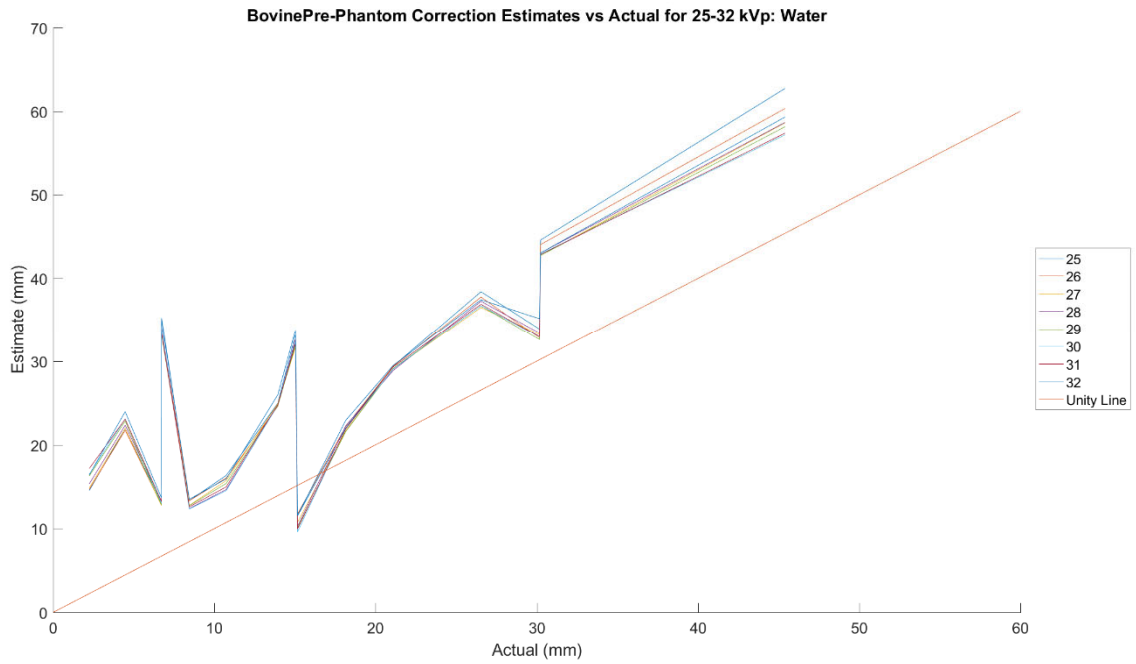


Figure 2.7 Bovine phantom ROI water thickness estimates vs. actual for each kVp. The top shows the estimates using only the calibration phantom, and the bottom plot shows estimates after a linear correction (3x3 matrix) was applied using data from the top plot.

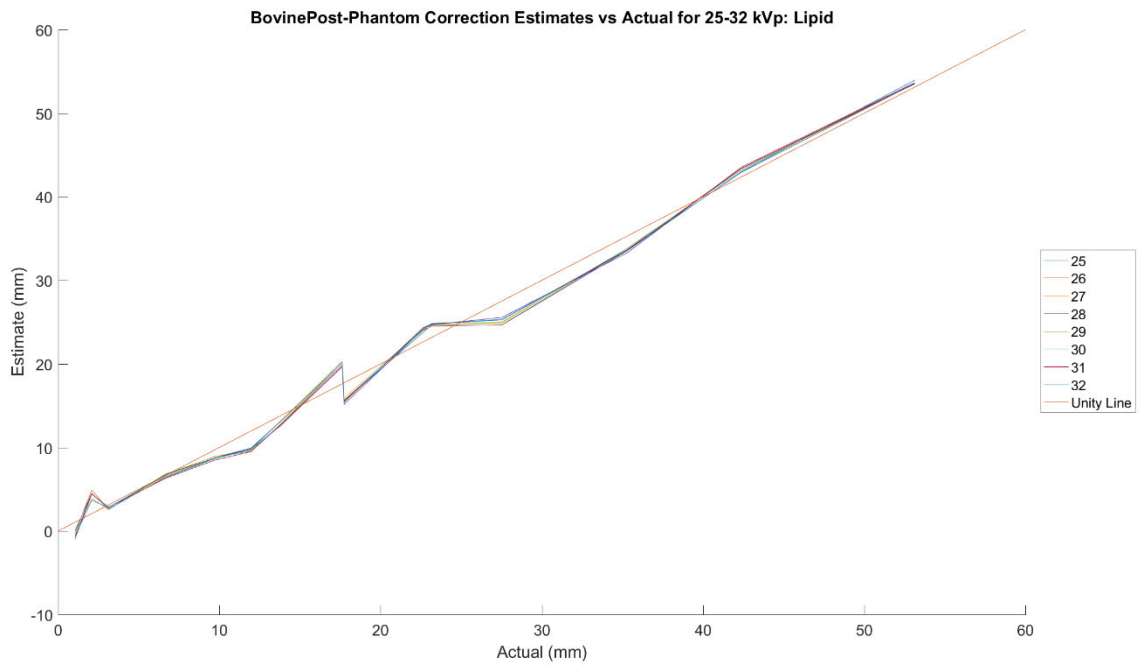
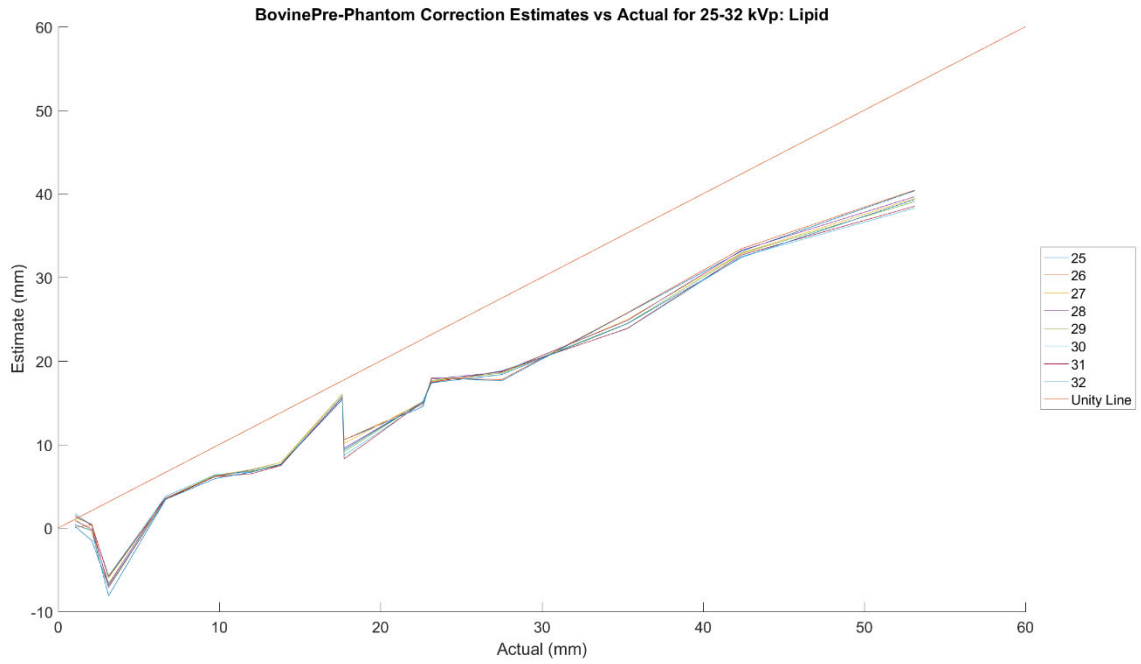


Figure 2.8 Bovine phantom ROI lipid thickness estimates vs. actual for each kVp. The top shows the estimates using only the calibration phantom, and the bottom plot shows estimates after a linear correction (3x3 matrix) was applied using data from the top plot.

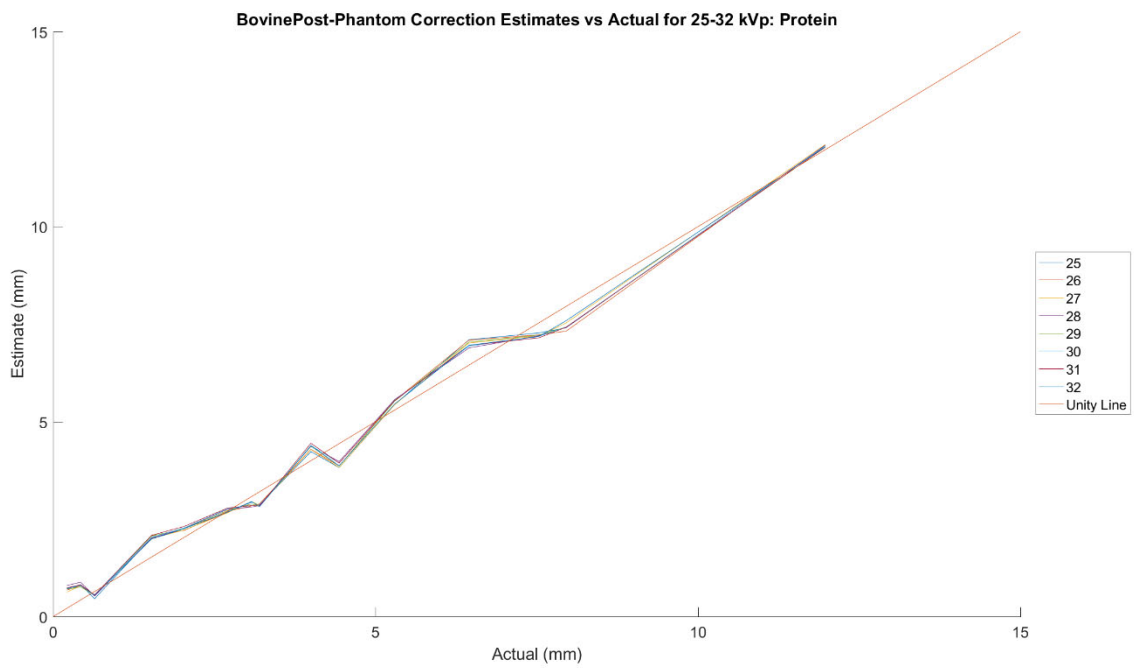
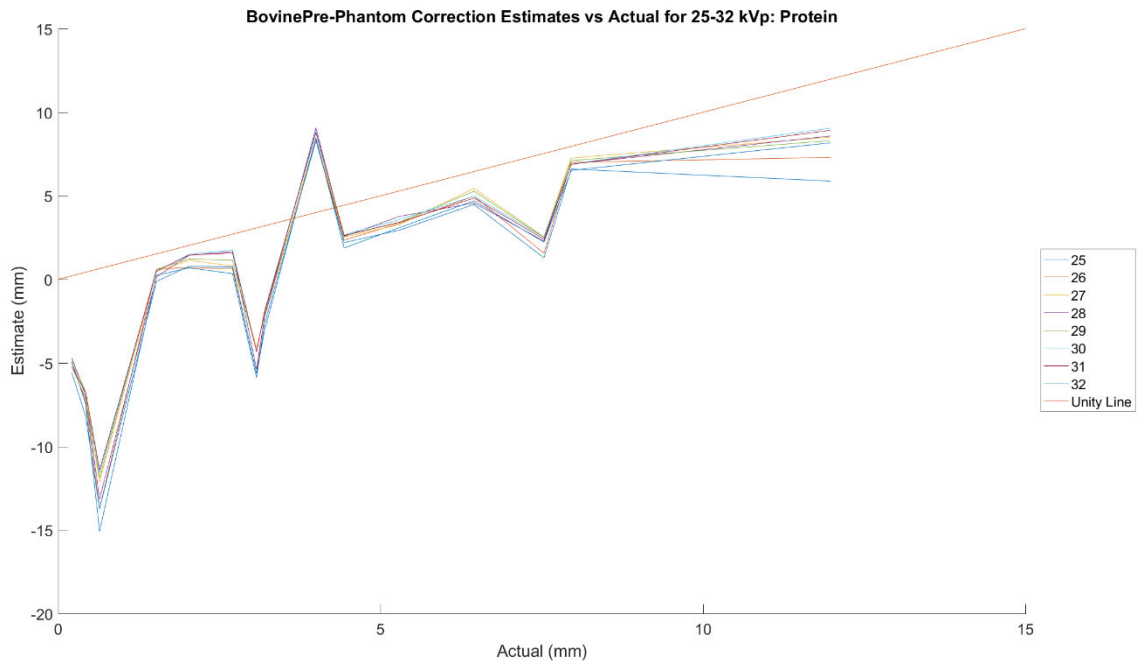


Figure 2.9 Bovine phantom ROI protein thickness estimates vs. actual for each kVp. The top shows the estimates using only the calibration phantom, and the bottom plot shows estimates after a linear correction (3x3 matrix) was applied using data from the top plot.

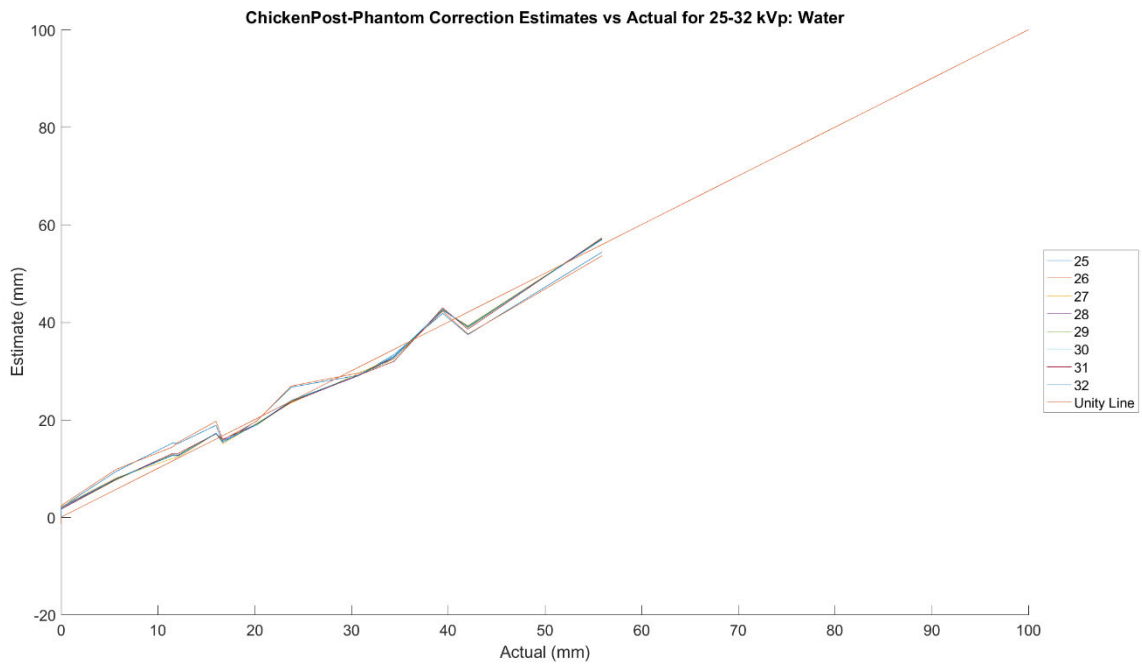
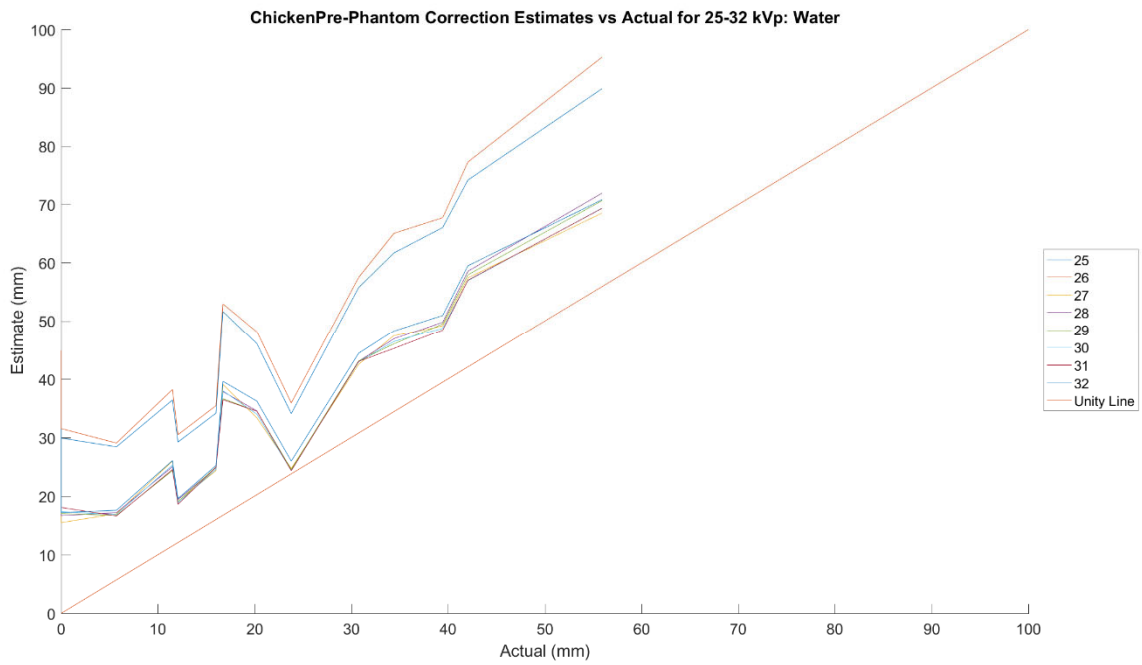


Figure 2.10 Chicken phantom ROI water thickness estimates vs. actual for each kVp. The top shows the estimates using only the calibration phantom, and the bottom plot shows estimates after a linear correction (3x3 matrix) was applied using data from the top plot.

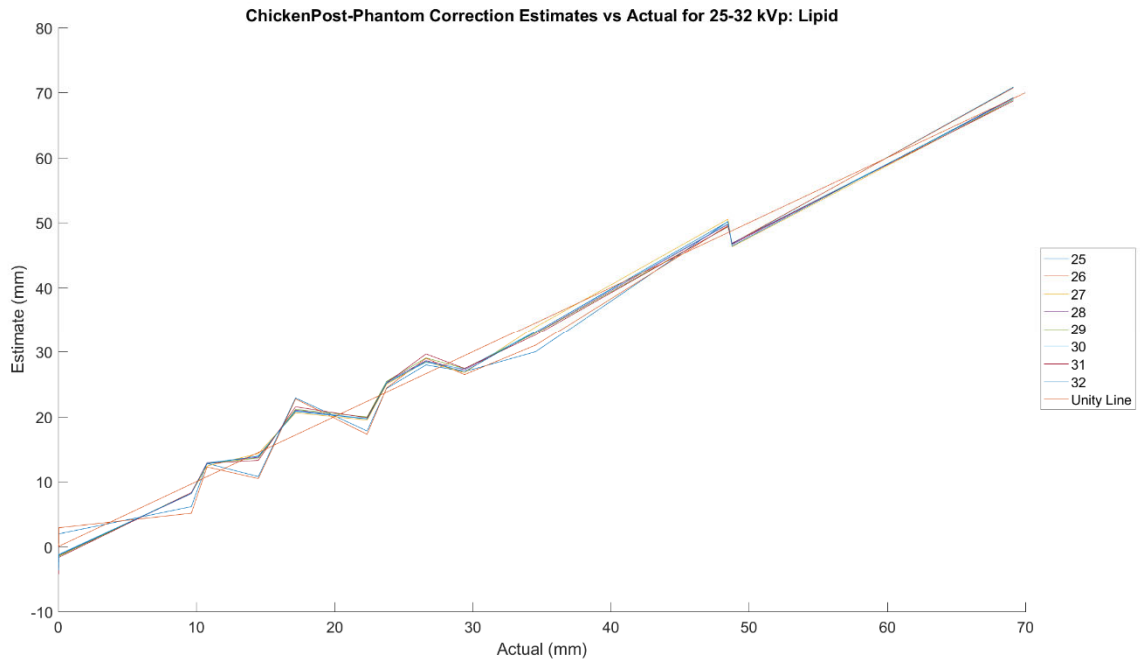
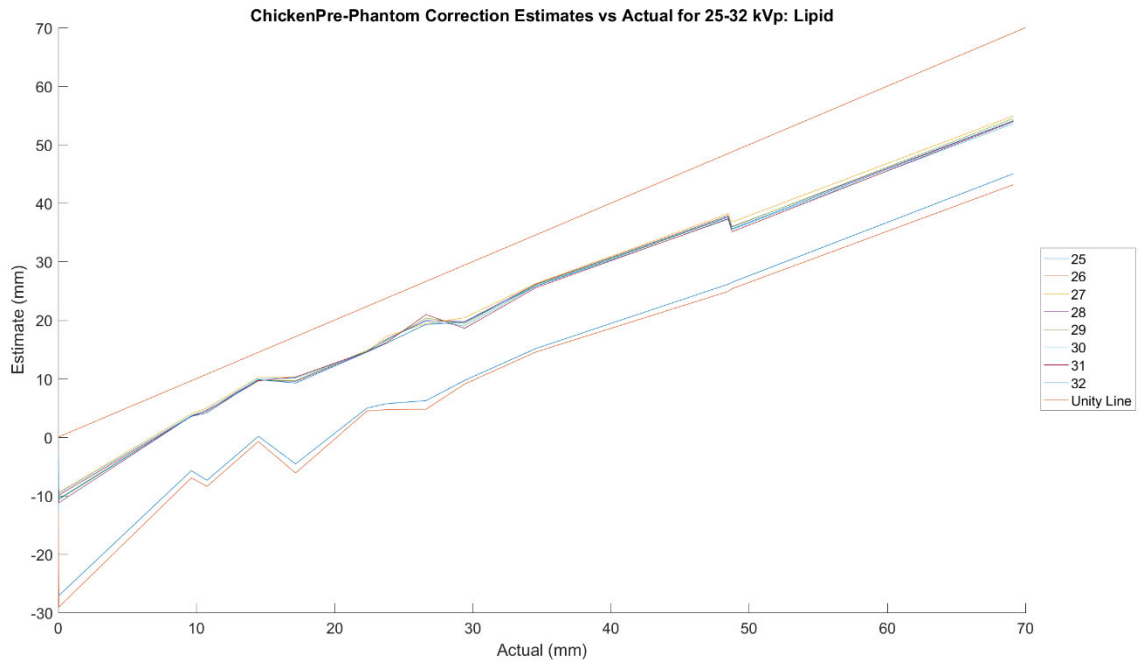


Figure 2.11 Chicken phantom ROI water thickness estimates vs. actual for each kVp. The top shows the estimates using only the calibration phantom, and the bottom plot shows estimates after a linear correction (3x3 matrix) was applied using data from the top plot.

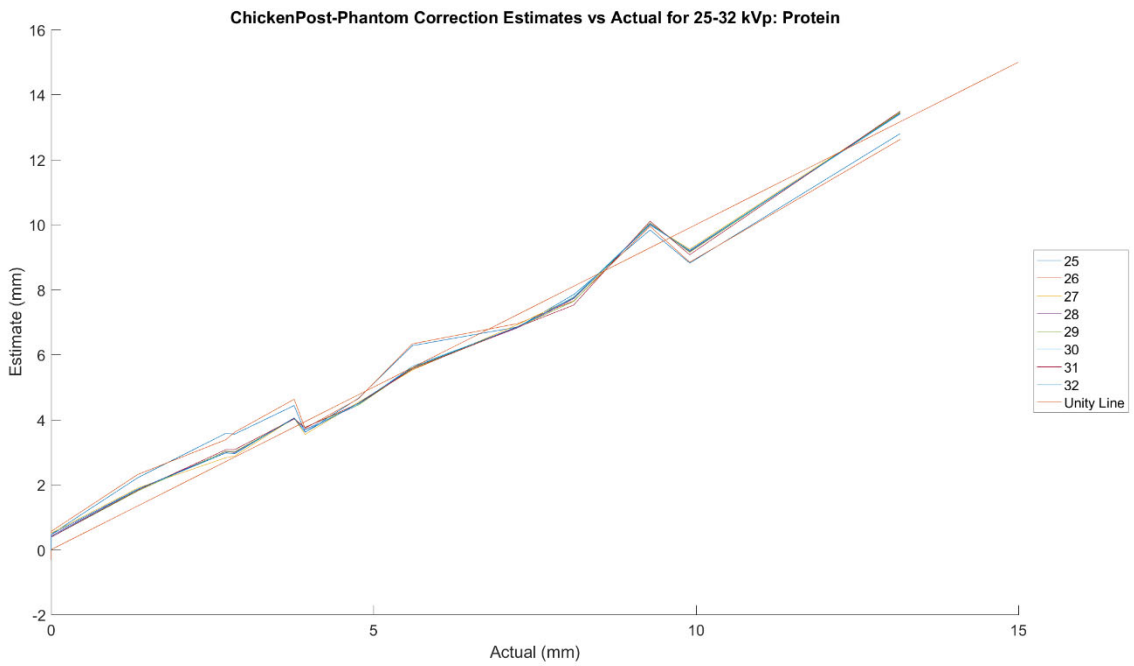
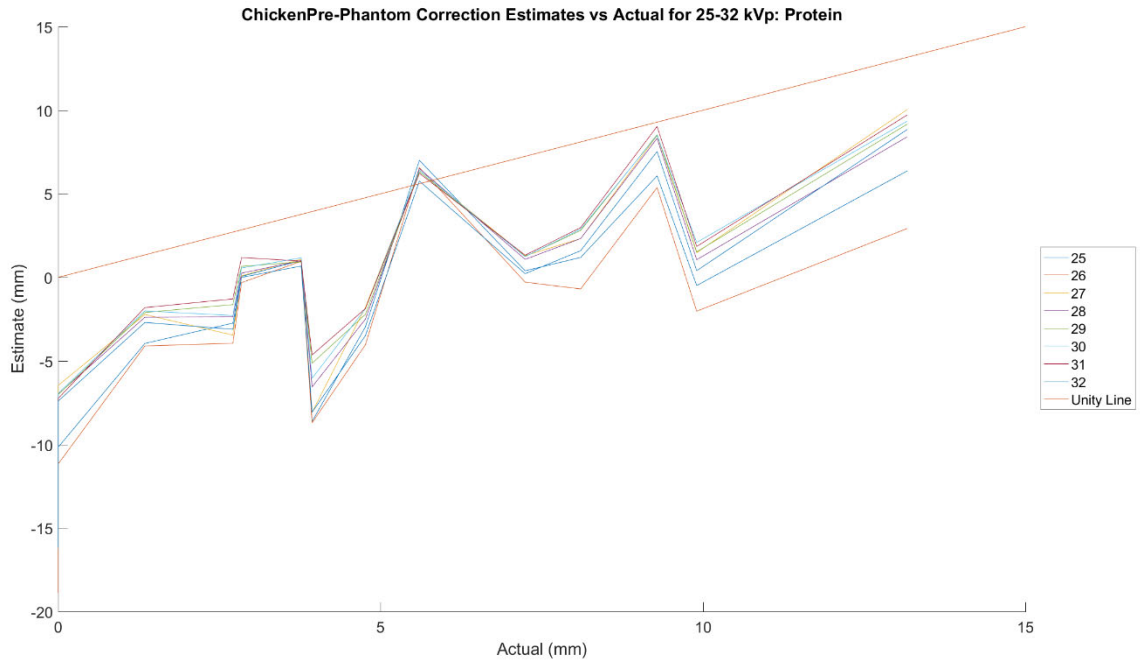


Figure 2.12 Chicken phantom ROI water thickness estimates vs. actual for each kVp. The top shows the estimates using only the calibration phantom, and the bottom plot shows estimates after a linear correction (3x3 matrix) was applied using data from the top plot.

Figure 2.13, Figure 2.14, and Figure 2.15 show the percent errors of the 15 regions of interest (ROIs) of the bovine phantom before and after applying the transfer function. The top plot shows the percent error before the bovine correction/transfer function was applied, and the bottom shows the estimates after the bovine correction was applied.

$$\% \text{ Error} = \text{Relative Percent Difference (RPD)} = 2 * \frac{(3CB \text{ Estimate} - \text{Lab Estimate})}{|3CB \text{ Estimate}| + |\text{Lab Estimate}|} * 100, \text{ where}$$

$$RPD = 0 \text{ when } 3CB \text{ Estimate} = \text{Lab Estimate} = 0$$

The RPD was used over percent difference to avoid dividing by zero. The *Lab Estimate* is the computed estimate based on laboratory results of tissue samples.

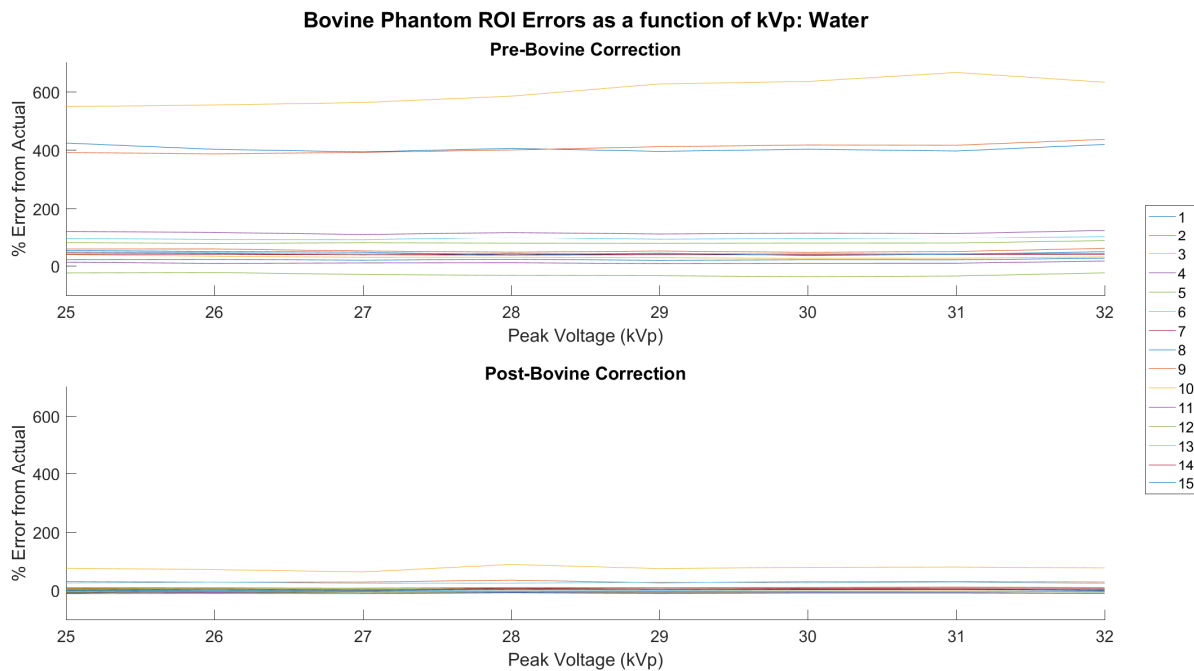


Figure 2.13 The 3CB water thickness estimate for the fifteen ROIs of the bovine phantom are shown before and after linear correction was applied.

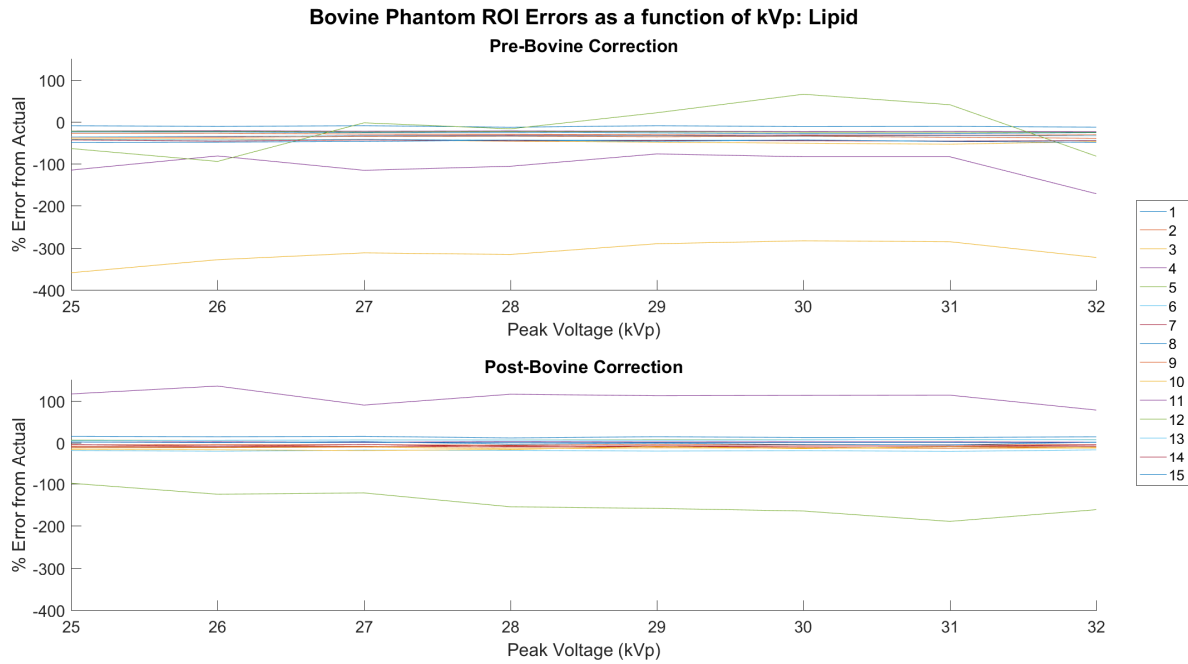


Figure 2.14 The 3CB lipid thickness estimate for the fifteen ROIs of the bovine phantom are shown before and after linear correction was applied.

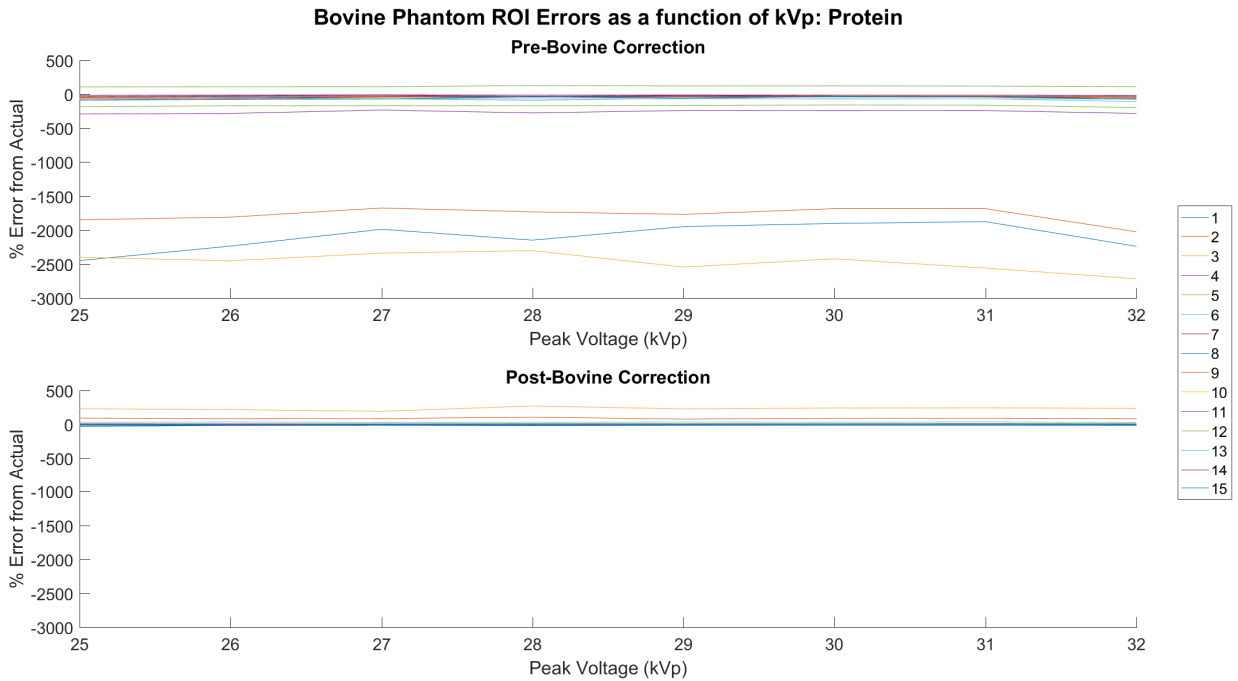


Figure 2.15 The 3CB protein thickness estimate for the fifteen ROIs of the bovine phantom are shown before and after linear correction was applied.

Oil Experiments

The results for the oil experiment are shown in Figure 2.16. The affine transformation seemed to correct the thickness estimate error between the two energy levels, though it did not correctly estimate the measured 30 mm thickness. For each boxplot, “the central mark is the median, the edges of the box are the 25th and 75th percentiles, the whiskers extend to the most extreme datapoints the algorithm considers to be not outliers, and the outliers are plotted individually” (MATLAB, 2016b). The top plot shows the estimated lipid thicknesses pre-bovine correction. Regions of interest on the oil images are compared between two different LE levels, 27 and 30 kVp. There are significant differences ($p < 0.001$ for all comparisons) in the estimated lipid thickness between the two energy levels for all ROIs. After the bovine correction is applied (bottom plot), there still seem to be significant differences between the two energy levels. Moreover, there is still an approximately 16% error between the actual and estimated lipid thickness (30 mm vs. 25 mm, respectively). A similar figure can be seen for the water experiment, but the error is larger between actual and estimated (~40 %).

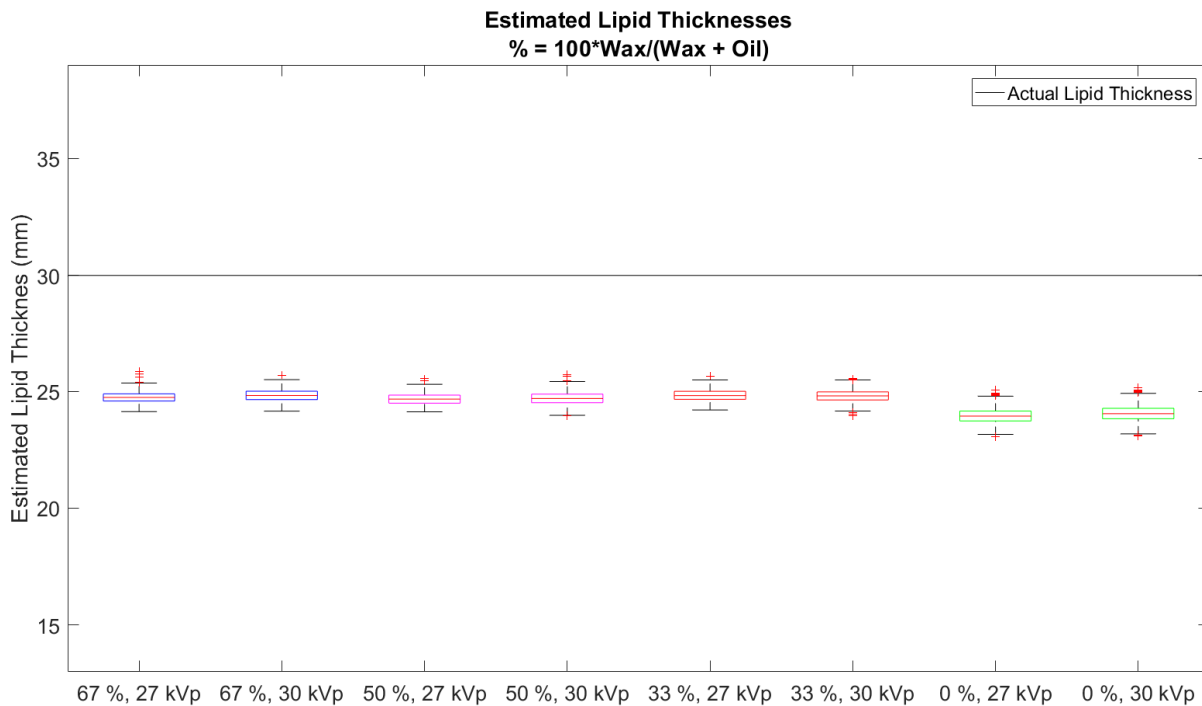
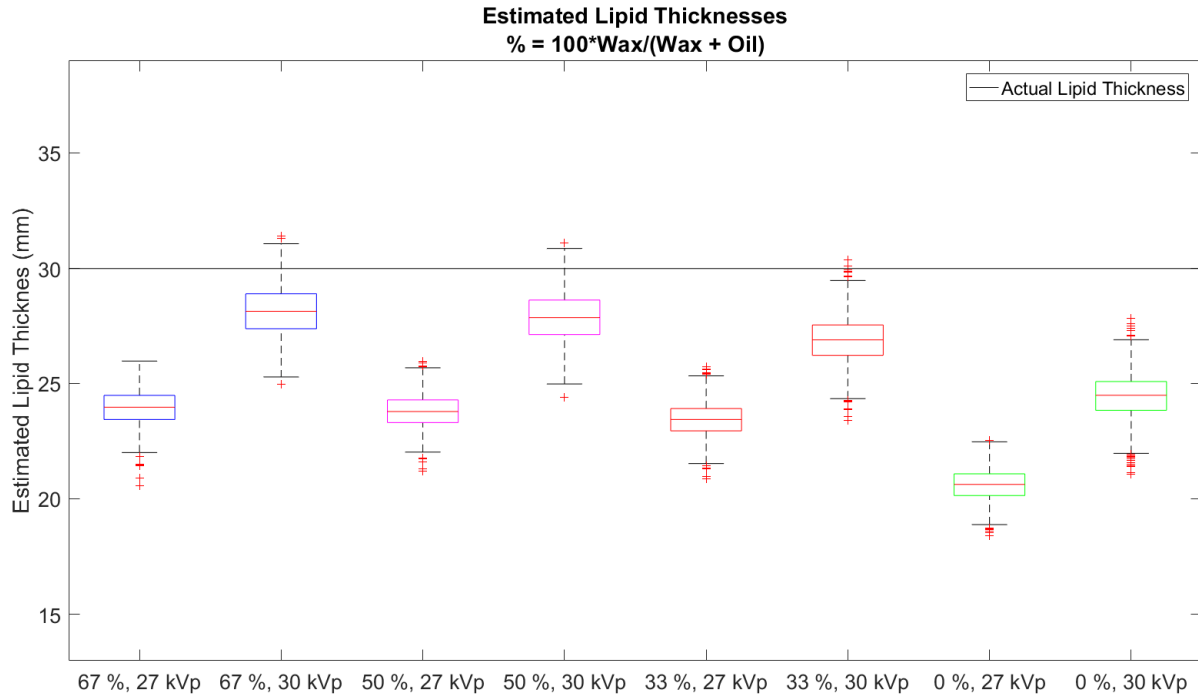
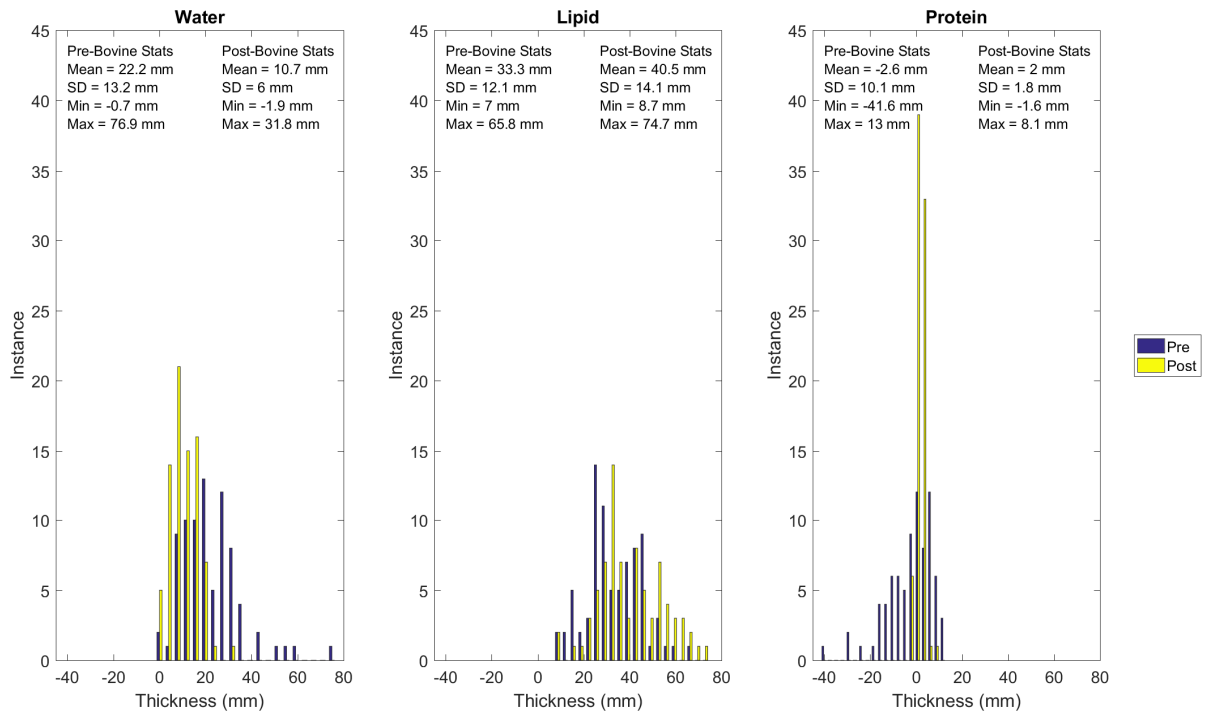


Figure 2.16 The estimated lipid thicknesses for different regions of interest (ROIs), pre- and post-bovine correction.

Population Corrections

Figure 2.17 shows patient data thickness estimates before and after models were applied. The top figure shows these distributions for pre- and post-bovine correction estimate, and the bottom for the chicken model. The mean, standard deviation, minimum thickness, and maximum thickness for pre- and post-model corrections are shown for all distributions. For both models, the lipid compartment distribution seemed to shift toward the right, indicating that the 3CB calibration phantom was underestimating lipid thicknesses. For water distributions in both models, the post-model correction narrowed and shifted the distribution to the left, which indicates that the 3CB calibration phantom was overestimating the water compartment. This overestimation seems to have caused negative protein estimates in the distributions of both models; these have narrowed in ranged and shifted toward the right after the model corrections.

Distributions of 3CB Material Thickness Estimates: Pre- and Post-Bovine Correction



Distributions of 3CB Material Thickness Estimates: Pre- and Post-Chicken Correction

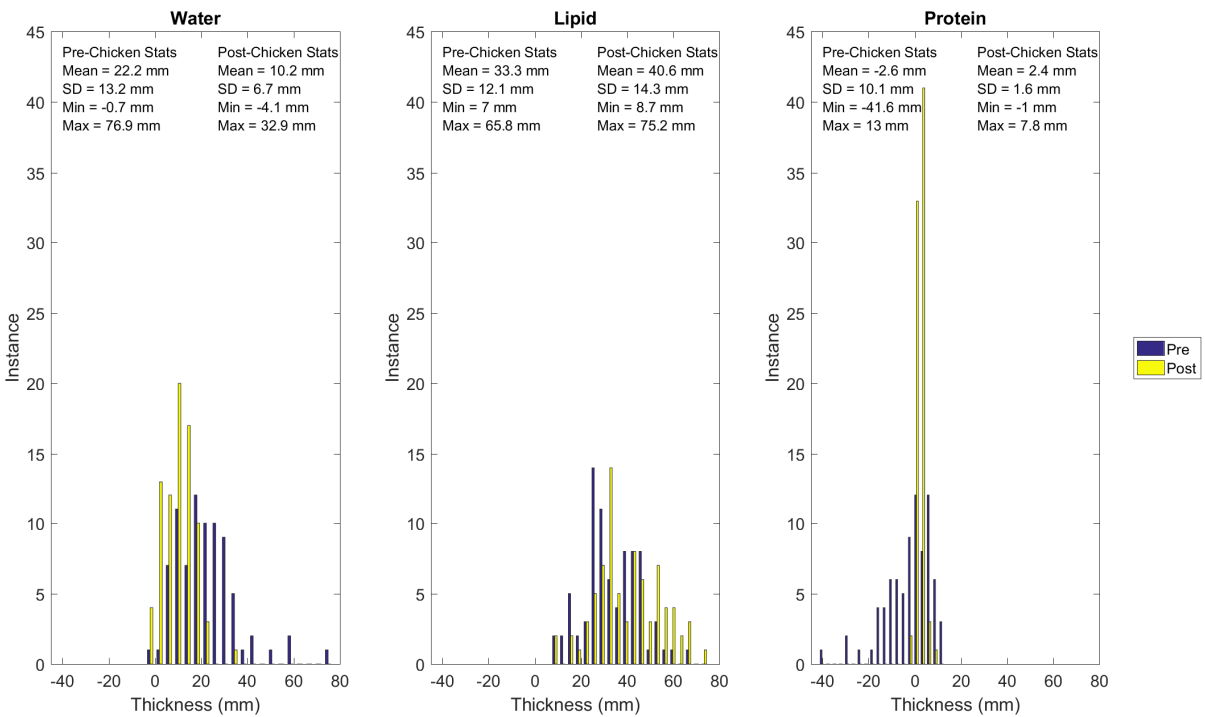


Figure 2.17 Estimated water, lipid, and protein thickness distributions of sampled population. The top figure shows distributions before and after bovine model corrections, and the bottom figure shows these for the chicken model corrections.

Discussion

The above experiments seemed to show that mass attenuation differences between biological and their calibration equivalent can become problematic for estimating compositional estimates, particularly when estimating three compositions and/or at varying kVp settings. A promising correction for such estimates seems to be deriving a linear map between the biological and calibration materials. Indeed, the oil and water experiments show that energy-dependent estimates of materials seem to be corrected using a map between the WLP calibration materials and bovine. The transfer function B was used as the linear map, and closer inspection of this function provides some intuition about how this correction works. For all three transformations of $(W \rightarrow W', L \rightarrow L', P \rightarrow P')$, the lipid vector in the transfer function does not seem to have any effect when each material is linearly mapped from the calibration material space to bovine. When the transfer function is applied to the lipid component, the scalar value for the lipid vector (b22) is 1. When the transfer function is applied to the water and lipid components, the scalar value for the lipid vector is approximately 0 (b21 and b23). Concomitantly, the water and protein vectors are scaled for every mapping. These two effects indicate that water and protein are the components that are being incorrectly estimated; thus, it is difficult to decouple these two components when we are in the calibration material space. When we applied this correction to participant estimates, this is what seems to occur. Water and protein compartments are scaled while the lipid compartment stays approximately the same (Figure 2.17). This transformation arrives at composition estimates that seem to be more realistic values, removing most of the negative protein errors.

In a related study by Ding *et al.*, they analyzed the chemical composition of lean and adipose bovine and chicken samples and compared it to estimates based on the three-compartment breast technique but for computed tomography.[40] The WLP content was approximately 0.80/0.02/0.17 for their lean bovine sample and 0.11/0.85/0.02 for the bovine adipose sample, respectively. As mentioned previously, the volumetric fractions of W/L/P for our samples were 0.81/0.012/0.178 for the lean muscle and 0.13/0.855/0.015 for the suet. These findings are consistent with each other. In previous work, compared the pre- and post-bovine WLP estimates of cadaver breast to estimates from a chemical composition analysis.[51] The combined RMSE for WLP estimates was 29.8% for pre-bovine estimates and 15.9% for post-bovine estimates. For Ding *et al.*, their combined RMSE was 2.7%. It is important to note that Ding *et al.* seem to achieve more accurate results because (1) they used two more biologically equivalent materials for their calibration phantom (water and vegetable oil) and (2) the difference in energy between their LE and HE images is much higher for CT than FFDM. They acquired their images at 100 kVp, 20 keV was the cutoff for their lowest energy, and 40 keV was selected as the splitting energy between their LE and HE bins. This would yield less correlation between LE and HE images since there would be greater separation between Compton and photoelectric events.

The results of this study should be considered when using dual energy X-ray techniques that involve calibration materials at varying kVp energy levels. This would involve applying the 3CB technique for other imaging modalities, such as breast tomosynthesis. Although the bovine correction seemed to have corrected for unrealistic

estimates, a combined RMSE of 15.9% is still not optimal. Higher energy separation between the LE and HE images should help ameliorate this error.

One limitation of this study is that the bovine correction may not cover the entire range of WLP variations found in breasts, and is perhaps the reason why we still see negative protein estimates for some lesion samples. As an example, although the bovine correction removed the estimate differences between the two energy levels, it still did not accurately estimate it for either both water and oil (and intended target of 30 mm). We believe that this is because the bovine phantom did not contain a 100% lipid compartment or 100 % water compartment. It is, therefore, imperative not to over fit when creating a map between the two material spaces. Another limitation is that the bovine and chicken maps were derived using a specific X-ray machine, and differences between X-ray sources among machines may create large enough errors in estimates that a bovine calibration may be needed for each X-ray machine that is used for clinical studies. It is also particularly important to test whether the bovine map is stable over time, especially for longitudinal studies. Lastly, there may be limitations in the bovine and chicken maps because of inherent differences between animal and human tissues. Experiments comparing the chemical composition of cadaver breasts and thickness estimates using the bovine map show similar estimates, however.[51]

In conclusion, energy-dependent differences between biological materials and their calibration equivalents may be corrected using a linear map between the two material spaces. This map, although itself still energy-dependent, could be used to correct erroneous compositional estimates for dual-energy mammography techniques.

Chapter 3 Studies on Other Error Sources

After acquiring the LE image, HE image, and total breast thickness estimate at every pixel (i.e., the breast thickness map) for 3CB, the next part is estimating the water, lipid, and protein compartment images. A calibration phantom is used to derive this 3CB composition based on a linear mapping of LE, HE, and total breast thickness measurements. There exists, however, sources of error that can influence LE and HE measurements and, thus, 3CB composition estimates. Two of these error sources are discussed in this chapter, and a third was covered more in-depth in Chapter 2.

Flat-Fielding

Full field digital mammography (FFDM) scanners typically acquire polychromatic X-ray projection images using cone-beam source geometry. The intensity that is measured at a detector's pixel location—even when no object is present—varies because of numerous factors, and nonuniformity due to cone-beam geometry becomes important when performing compositional measurements. Linear and non-linear corrections have been developed by Seibert *et al.* and Kwan *et al.* [54, 55] Here we develop an empirical polynomial model, similar to Kwan *et al.*'s, to apply flat-fielding (gain) corrections to X-ray projections.

Methods

Hologic Selenia full-field digital mammography system (Hologic, Inc.) was used to acquire all images. CIRS (Computer Imaging Reference Systems, Inc.) phantom slabs with 50% fibroglandular and 50% adipose breast tissue equivalent materials were

used for all images. Three phantoms of thickness 4, 2, and 1 cm were stacked in different combinations to obtain scans of 1 – 8 cm thicknesses at 1 cm intervals. The imaging parameters for the images are shown in Table 3.1.

Table 3.1 Scanner settings for BR50/50 CIRS phantoms for flat-fielding model

kVp	Anode-filter(s) Combination	mAs
25-31	Mo/Mo	100
32	Mo/Rh	100
39	Mo/Rh-Al	100

MATLAB (Natick, Massachusetts, USA) software was used to create empirical flat-fielding models. First, the 2D slab images were turned into 3D surface images, where the x and y axes corresponded to pixel locations and the z-direction to image intensity. Next, a 10x10 moving window median filter was applied to the surface image to remove stochastic noise. The surface image S_{in} was then normalized in two steps. First, the scanner’s DC component (I_{DC} , taken from the DICOM image header) was removed and a pre-normalization was applied with the initial intensity derived from the I_0 model (see Empirical I_0 Model found later in this chapter) using the following equation

$$S_{N0} = (S_{in} - I_{DC}) / (I_0 - I_{DC}) \quad \text{Equation 3-1}$$

Secondly, this was normalized by the intensity value of S_{N0} located at (x_0, y_0) , which is a small region of interest surrounding the point where the incident X-ray beam is perpendicular to the detector plane. This made it so that the flat-fielding model would be independent of exposure (mAs) settings, so

$$S_N = S_{N0} / S_{N0}(x_0, y_0) \quad \text{Equation 3-2}$$

After normalization, S_N was downscaled by a factor $c \approx 0.15$ such that the smallest positional dimension (either x or y dimension) of the image (in this case, the x-axis) was size 250, so

$$S_S = S_N(c * x_{size}, c * y_{size}) \quad \text{Equation 3-3}$$

Following this, a third-degree polynomial in x and y was made using the MATLAB function *fit*. Polynomial fits were made for all thicknesses (T) and kVps, so the flat-fielding model function is the function $S_{FFM}(x, y, kVp, T)$. After the flat-fielding correction is applied to S_S , we get $S_{FF} = \frac{S_S}{S_{FFM}}$. To validate fitting, the normalized RMSE $RMSE_N = 100 * \frac{RMSE}{\sigma_{mean}}$ (%) between the surface fit and S_S was compared to the normalized standard deviation σ_{SDN} of the median-filtered image noise, where

$$\sigma_{SDN} = \frac{100 * \sigma_{SD}}{\sigma_{mean}} (\%) \quad \text{Equation 3-4}$$

σ_{SD} : standard deviation of $S_S(x_0, y_0)$

σ_{mean} : mean of $S_S(x_0, y_0)$

Note that σ_{SDN} is smaller than the actual image noise since it is the residue noise left over after a median filter was applied to the original image.

Results

Figure 3.1, Figure 3.2, Figure 3.3 depict how well a polynomial surface fit the input for the three different filter conditions of the slab images. In each figure, the 1 cm (top) and 8 cm (bottom) cases are shown. For each thickness case, the top-left surface plot is the median-filtered, normalized, and downscaled input image S_S , which varied up to approximately 15% in normalized intensity. The top-right surface plot is the third-

degree polynomial fit in x and y of S_S . The bottom plot is S_{FF} , the resulting surface plot after the flat-fielding correction is applied to S_S . In almost all surface fit cases, the polynomial surface fit performed better than the normalized median-filtered image noise of the input image (i.e., $RMSE_N < \sigma_{SDN}$ for almost all cases). Figure 3.4 shows plots of $RMSE_N$ and σ_{SDN} as a function of kVp. These were used to verify a good fit for the polynomial model. Plots similar to this were made for all thicknesses. Only the surface plots for $(T = 6 \text{ cm}, kVp = 31)$ and $(T = 4 \text{ cm}, kVp = 26)$ had $RMSE_N > \sigma_{SDN}$, but these were within rounding error.

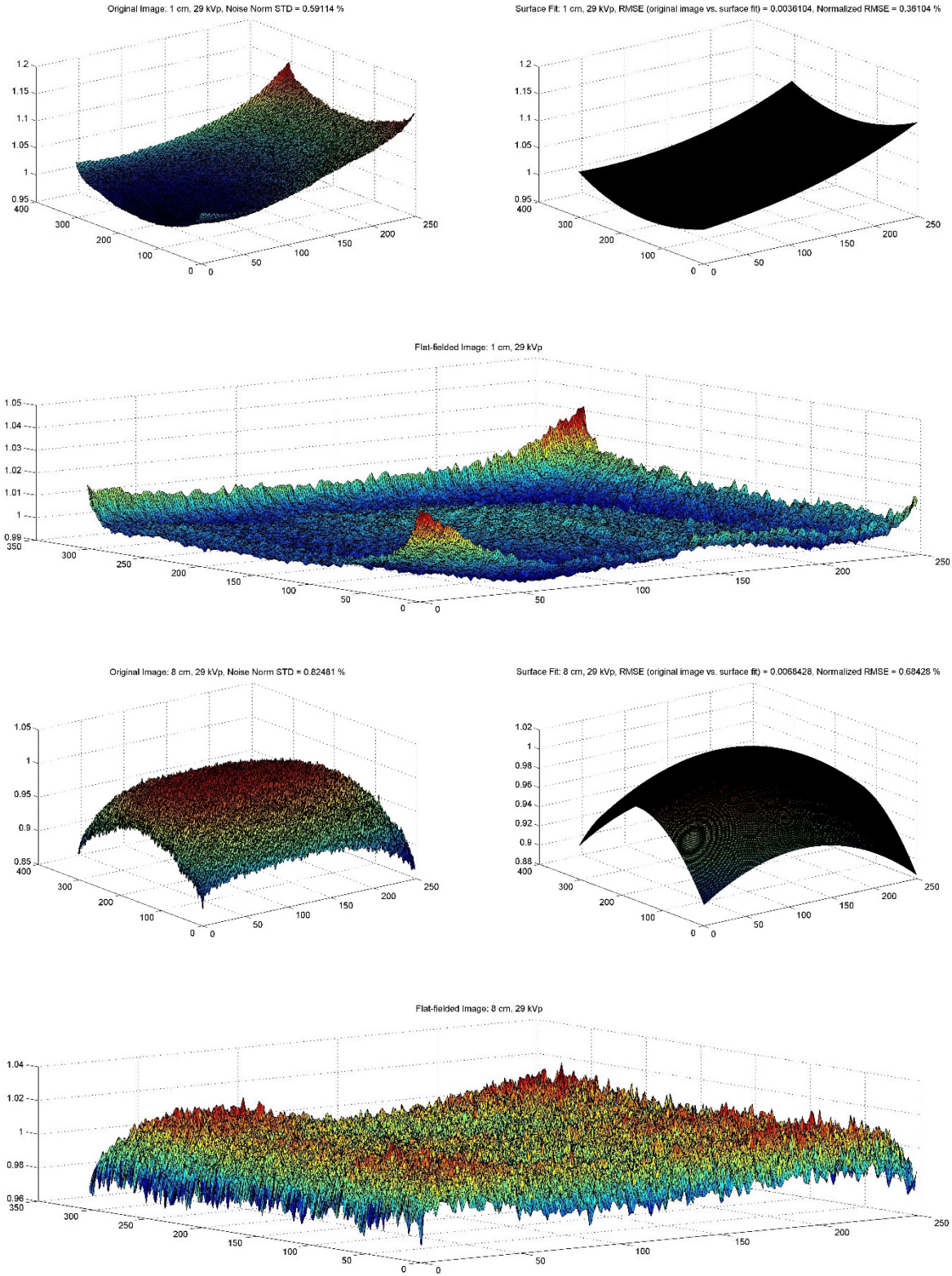


Figure 3.1 Flat-fielding surface fits for kVp = 29 (Mo/Mo anode/filter combinations), 1 cm (top plots) and 8 cm (bottom plots). For 1 cm plots, $\sigma_{SDN} = 0.59\%$, $RMSE_N = 0.36\%$. For 8 cm plots, $\sigma_{SDN} = 0.83\%$, $RMSE_N = 0.68\%$.

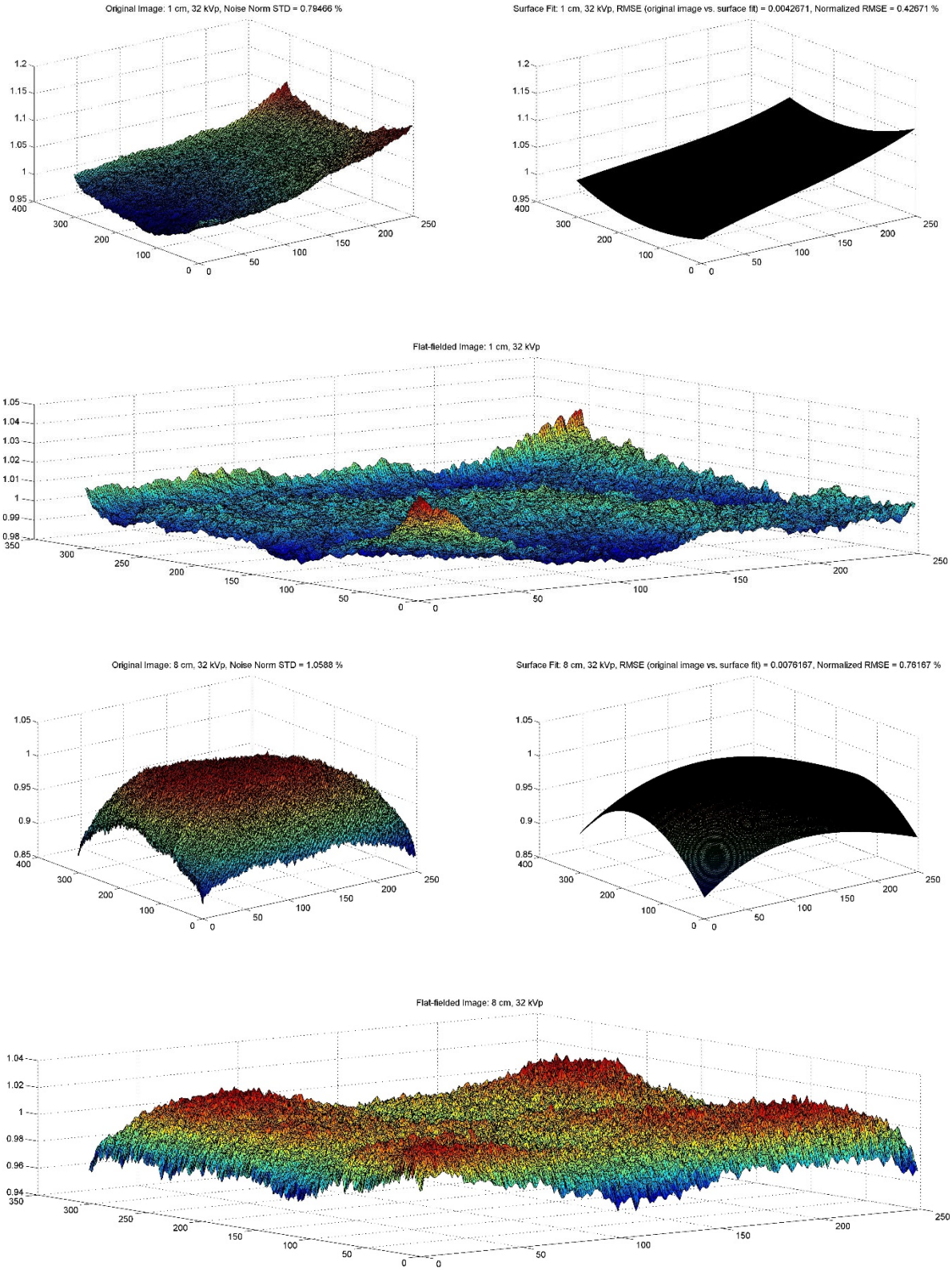


Figure 3.2 Flat-fielding surface fits for kVp = 32 (Mo/Rh anode/filter combinations), 1 cm (top plots) and 8 cm (bottom plots). For 1 cm plots, $\sigma_{SDN} = 0.79\%$, $RMSE_N = 0.43\%$. For 8 cm plots, $\sigma_{SDN} = 1.06\%$, $RMSE_N = 0.76\%$.

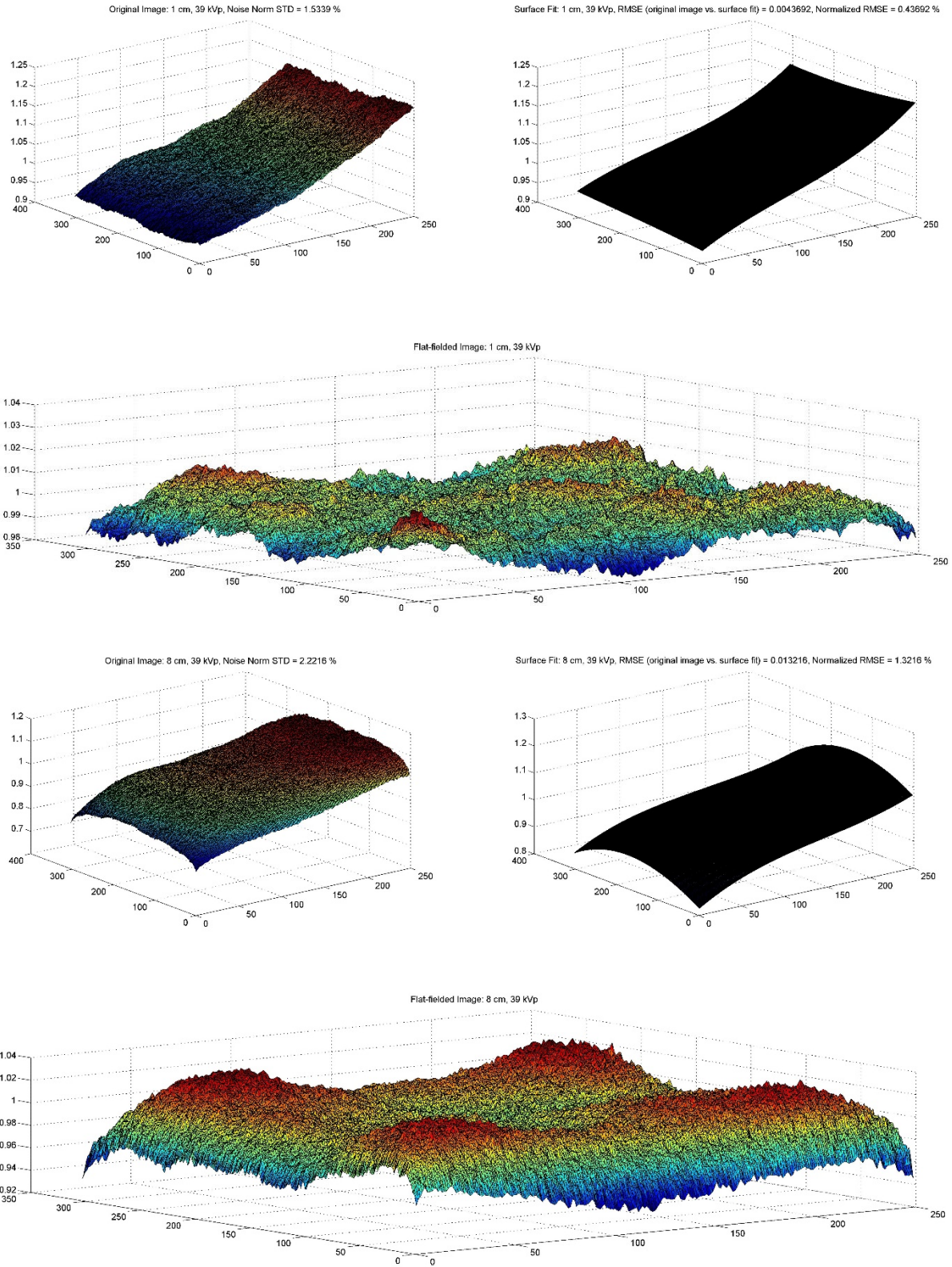


Figure 3.3 Flat-folding surface fits for kVp = 39 (Mo/Rh-Al anode/filters combinations), 1 cm (top plots) and 8 cm (bottom plots). For 1 cm plots, $\sigma_{SDN} = 1.53\%$, $RMSE_N = 0.44\%$. For 8 cm plots, $\sigma_{SDN} = 2.22\%$, $RMSE_N = 1.32\%$.

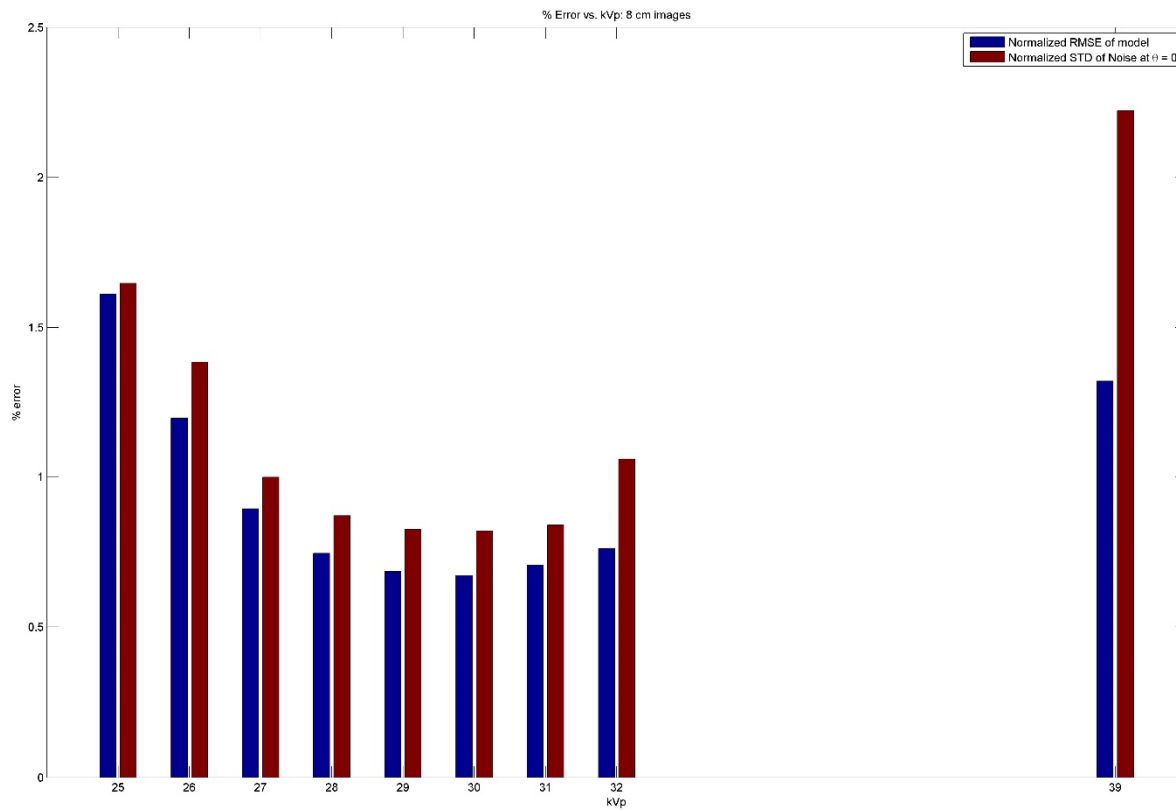
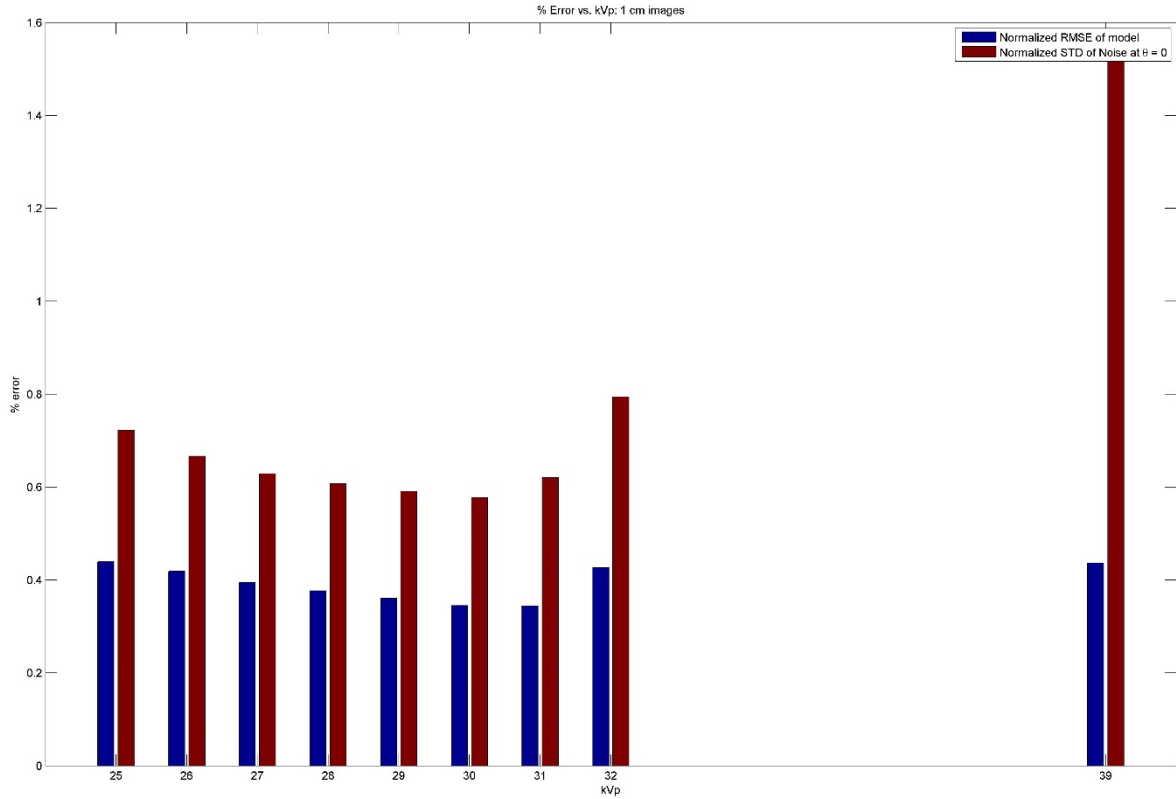


Figure 3.4 Flat-fielding plots of σ_{SDN} and $RMSE_N$ for 1 cm (top) and 8 cm (bottom) surface fits as a function of kVp.

Figure 3.5 shows the coefficients of a typical fit model created for $kVp = 29$. The x axis for each plot is the thickness T in cm , and the y axis is the intensity value of a coefficient $p_{i,j}$, where $i = 0, \dots, 3$ and $j = 0, \dots, 3$. Using the values for measured thicknesses 1, 2, ..., 8 cm , linear interpolation was used to estimate coefficient values for all thicknesses in the range $[1, 8]$ cm . This makes it so that the flat-fielding model function $S_{FFM}(x, y, kVp, T)$ is continuous in the range $T = [1, 8]$ cm .

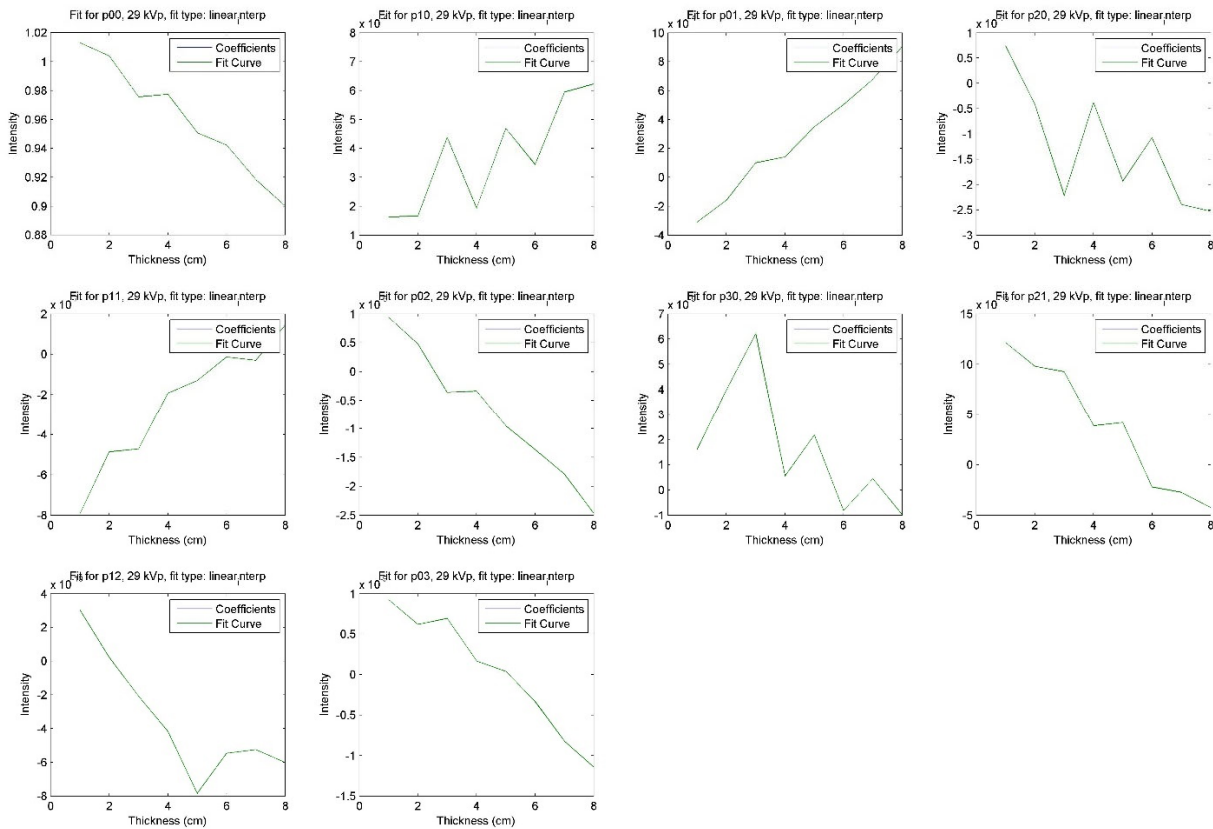


Figure 3.5 Flat-fielding model coefficients for 29 kVp. Linear interpolation was used to create flat-fielding values for all thicknesses between 1 and 8 cm , so the “Fit Curve” directly overlays over the plot of the surface fit coefficient values.

Discussion

The goal of the above was to create a method to correct for flat-fielding errors found when acquiring X-ray projection images. This correction is important for

estimating 3CB water, lipid, and protein compositions, since the method uses a calibration phantom to perform a linear mapping of LE and HE measurements. From the experiments, it was shown that there can be nonuniformity of up to a 15% due to the geometry of cone-beam X-ray projections used in mammography. To minimize this error and get an accurate linear mapping between the calibration phantom and breast measurements, LE and HE values should be position-independent. A third-degree polynomial flat-fielding model $S_{FFM}(x, y, kVp, T)$ seemed to correct geometric-based errors. The resulting flat-fielded image S_{FF} had non-uniformity errors reduced to approximately 2%. This method can be applied to LE and HE phantom and breast images before the 3CB composition is estimated. A thickness map would be needed to apply this flat-fielding correction to projection images. In addition, flat-fielding models would have to be made for each scanner that is used to acquire 3CB images by scanning uniform thickness breast composition phantoms, since these empirical models can vary between scanners.

Initial Intensity (I_0) Correction

In 3CB imaging, WLP thicknesses are estimated by using LE and HE log-signal functions A_i :

$$A_i = \ln\left(\frac{I}{I_0}\right), \quad \text{Equation 3-5}$$

where I is the measured attenuation photon intensity, I_0 is the nonattenuated photon intensity, and i is either *LE* or *HE*. It is, therefore, important to accurately estimate I_0 for both calibration phantom and breast images. Here we discuss the two methods that were used for estimating I_0 in 3CB images. This first method is based on an empirical model made from measuring nonattenuated images at varying exposures. The second one estimates I_0 from the single X-ray absorptiometry (SXA) step phantom that is used when acquiring 3CB images.

Methods

Empirical I_0 Model

An empirical I_0 model was created from nonattenuated X-ray images scanned with a Hologic Selenia FFDM system. Scans were taken at 20, 50, and 100 mAs and 25-32 and 39 kVp. A small ROI (75x150 pixels) was sampled from each image at the same location—where the X-ray source was perpendicular to the detector plane. A linear model, which uses mAs and kVp as dependent variables, was created using the 20 and 50 mAs samples, since the detector saturated at 100 mAs for higher kVps. To validate the empirical I_0 model, a two-compartment model was tested first. The 51-point

calibration point was sampled at ROIs that contained only water and protein, which shall be known as the two-compartment calibration phantom (2CCP). A two-compartment intermediate phantom (2CIP) was made by adding 1 cm of water to the 2CCP. The 2CCP was used for calibrating linear mapping equations, while the 2CIP was used to test accuracy. The percent $RMSE$, $RMSE_p = 100 * \frac{RMSE}{\max(Actual)}$, was used for this accuracy test.

I₀ from SXA Phantom

The SXA phantom, which is a step phantom that is normally used to estimate breast thickness at every pixel, was used to derive the negative log-signal values ($-A_i$) of a uniform material as a function of thickness.[53] This phantom was already included in 3CB FFDM images, since it is part of the routine procedure. A flat-fielding correction (see Flat-Fielding section from earlier in this chapter) was applied to the SXA phantom based on its known region-of-interest thicknesses. The ROIs of the SXA phantom were then located in the image by isolating the SXA phantom lead beads and then mapping ROI coordinates from these lead bead locations. Next MATLAB software function *polyfit* was used to create a first-degree polynomial fit. A first-degree polynomial was chosen since $-A_i$ is a linear function of material thickness T . Lastly, I_0 was estimated using this fitting function for $T = 0 \text{ mm}$.

Results

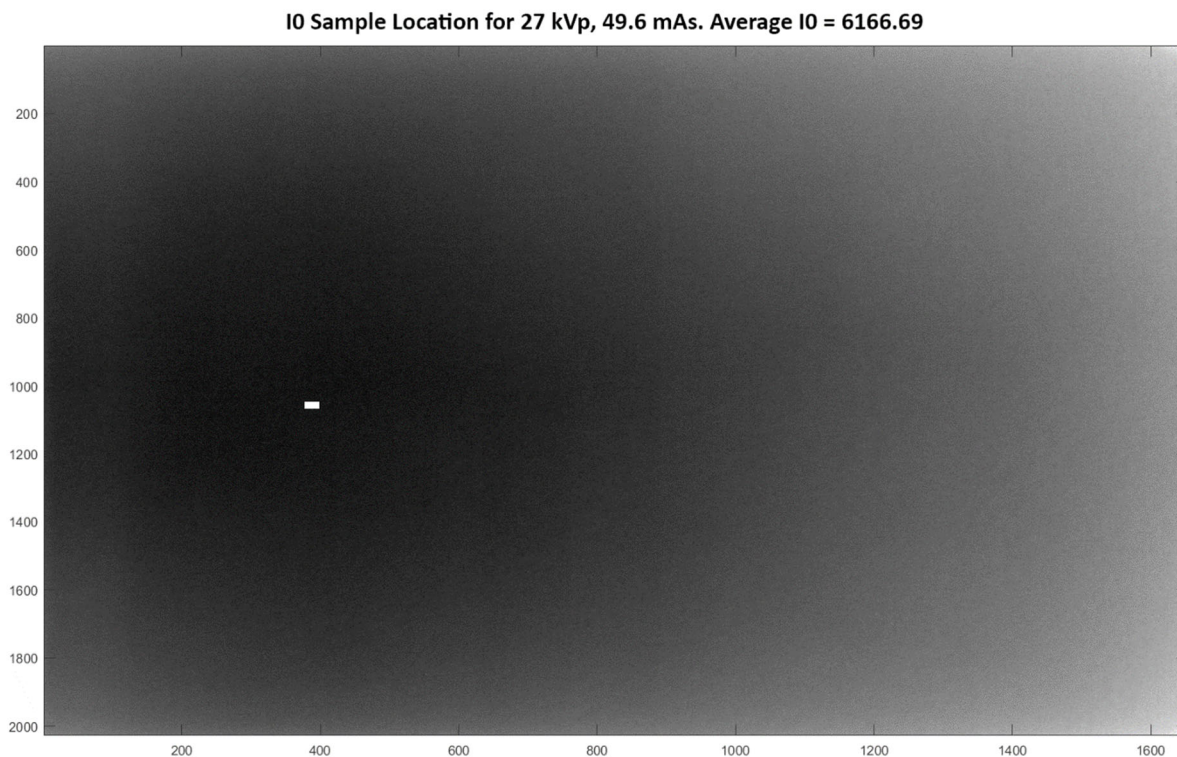


Figure 3.6 The ROI sample location for the empirical I_0 model

Table 3.2 lists the compositions of the two-compartment phantoms. Figure 3.7 shows R (LE/HE) vs. HE attenuation values for the 2CCP and 2CIP phantoms before the empirical I_0 model was applied. Curves were fit to the varying compositions of the 2CCP. Some of these compositional curves converge, which implies that the 2CCP linear mapping will poorly predict compositional estimates.

Table 3.2 Compositions of the two-compartment phantoms for testing the empirical I_0 model

ROI No.	2CCP Water Thickness (cm)	2CCP Protein Thickness (cm)	2CIP Water Thickness (cm)	2CIP Protein Thickness (cm)
1	6	0.89	7	0.89
2	6	1.34	7	1.34
3	4	0.59	5	0.59
4	4	0.89	5	0.89
5	2	0.3	3	0.3
6	2	0.44	3	0.44

7	6	0	7	0
8	6	0.44	7	0.44
9	4	0	5	0
10	4	0.3	5	0.3
11	2	0	3	0
12	2	0.15	3	0.15

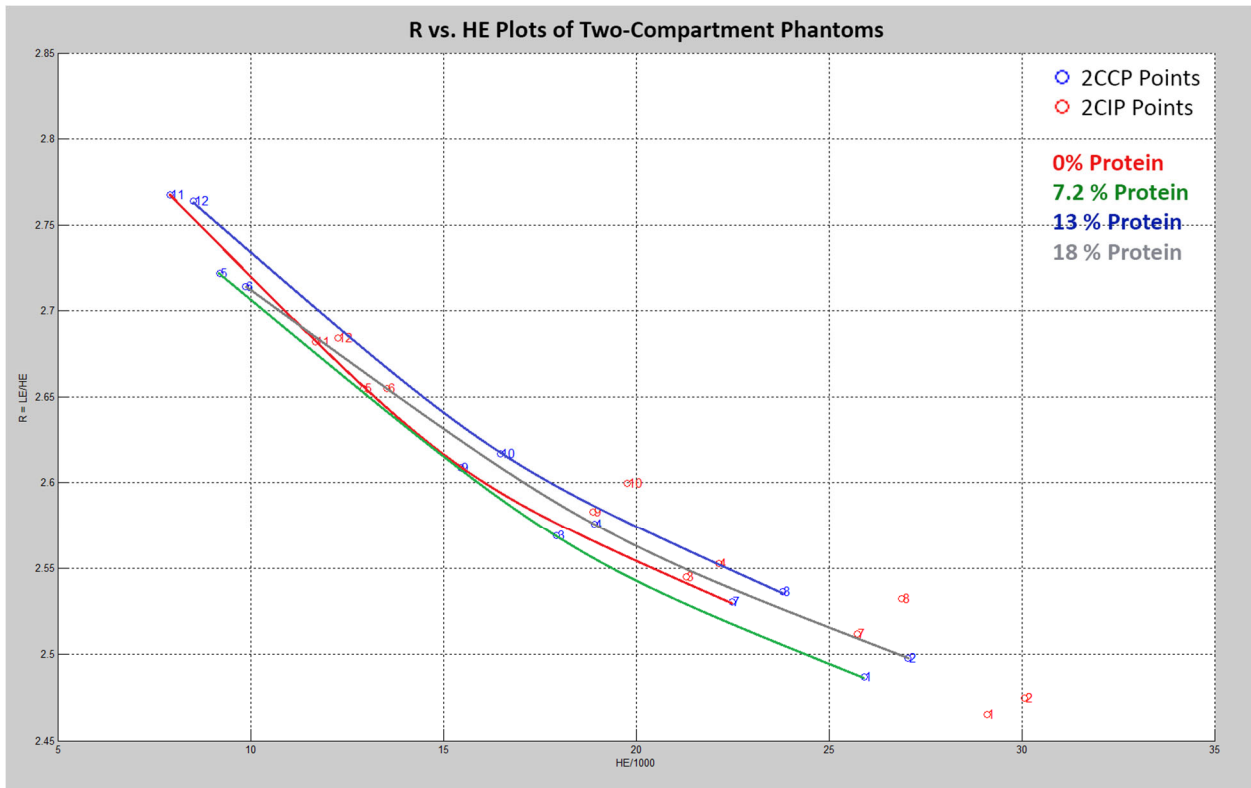


Figure 3.7 R vs. HE Plots of two-compartment phantoms before the empirical I_0 model was applied.

Figure 3.8 shows the R vs. LE plots of the two-compartment phantoms after the empirical I_0 model was applied. In this plot, only two of the 2CCP curves converge. After investigation, however, the composition of 2CCP point 12 had the incorrect composition (8.96 %); it is also the ROI most susceptible to error, since it is the region with the thinnest amount of protein content. The $RMSE_p$ for the 2CCP using the linear mapping

created from the 2CCP itself was 1.39% for water and 6.39% for protein. For validation, the $RMSE_p$ for the 2CIP was 5.37% for water and 25.55% for protein.

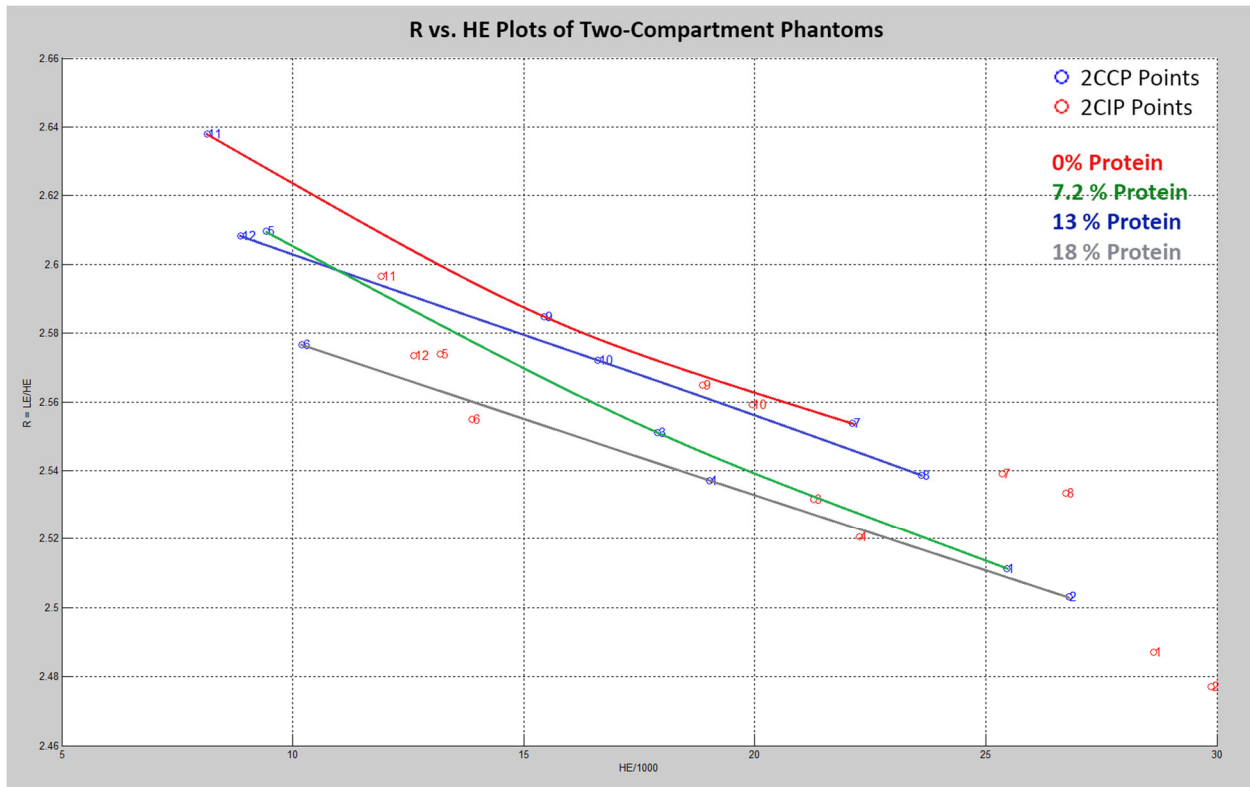


Figure 3.8 R vs. HE Plots of two-compartment phantoms before the empirical I_0 model was applied.

Figure 3.9 shows the nine ROIs of the SXA phantom that were used to estimate the SXA phantom-derived I_0 . The lead beads can be seen, and their estimated locations are shown by a red crosshair. A sample fit for I_0 derived from the SXA phantom for a breast scanned at 28 kVp is shown in Figure 3.10 and Figure 3.11. The I_0 for the LE CP and breast images was 6892.68 and 3701.56, respectively; the I_0 for the HE CP and breast images was 2597.44 and 1641.72, respectively.

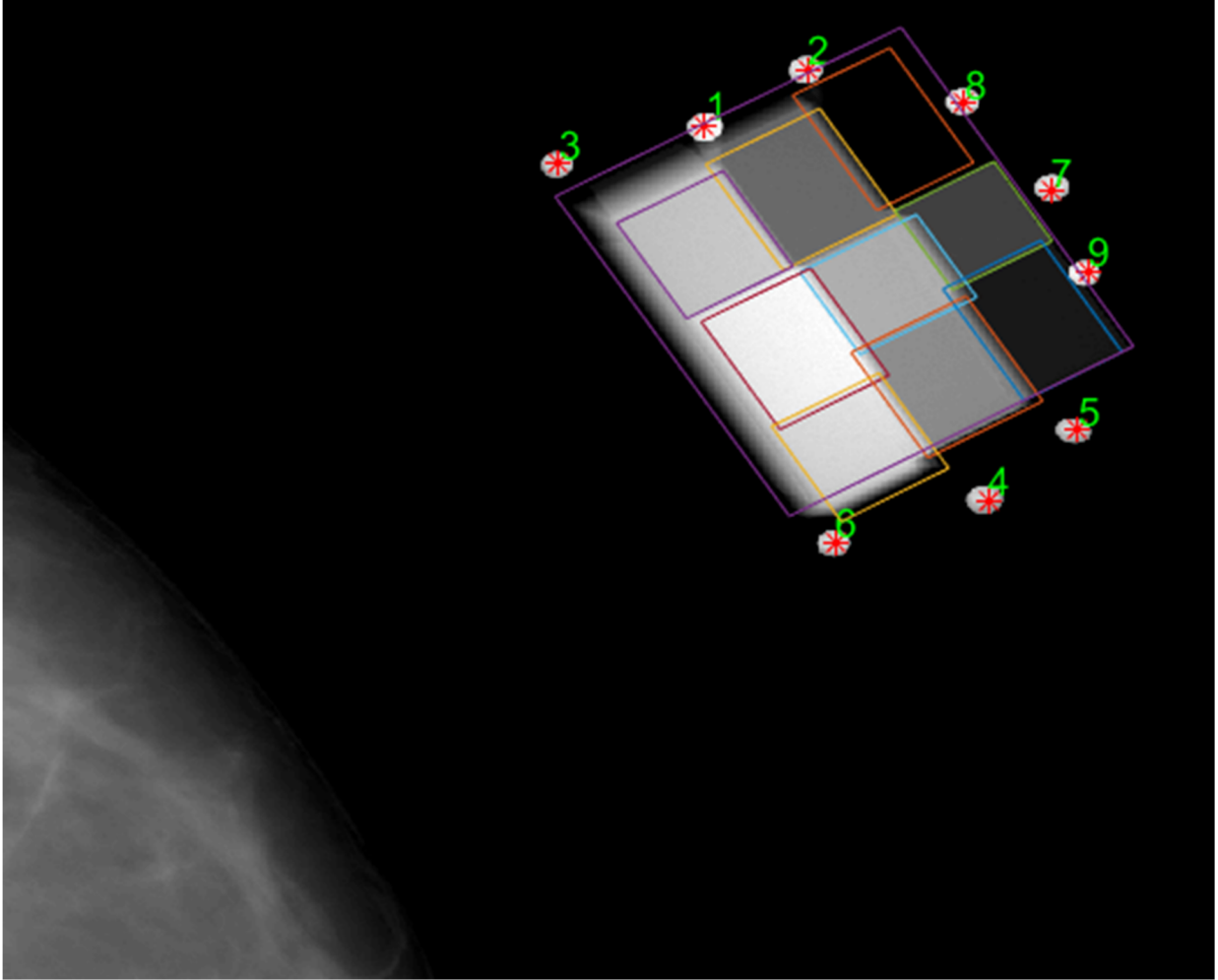


Figure 3.9 Located SXA ROIs phantom for estimating I_0 from the SXA phantom log-signal values.

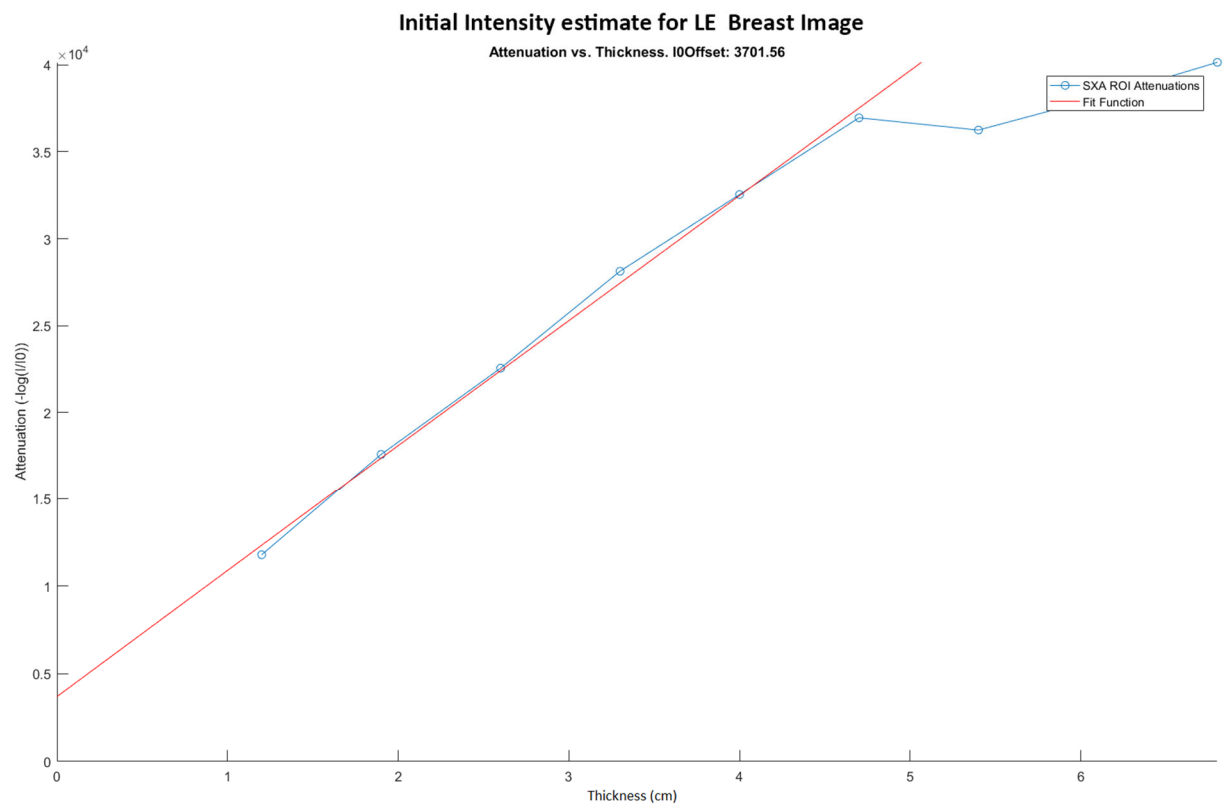
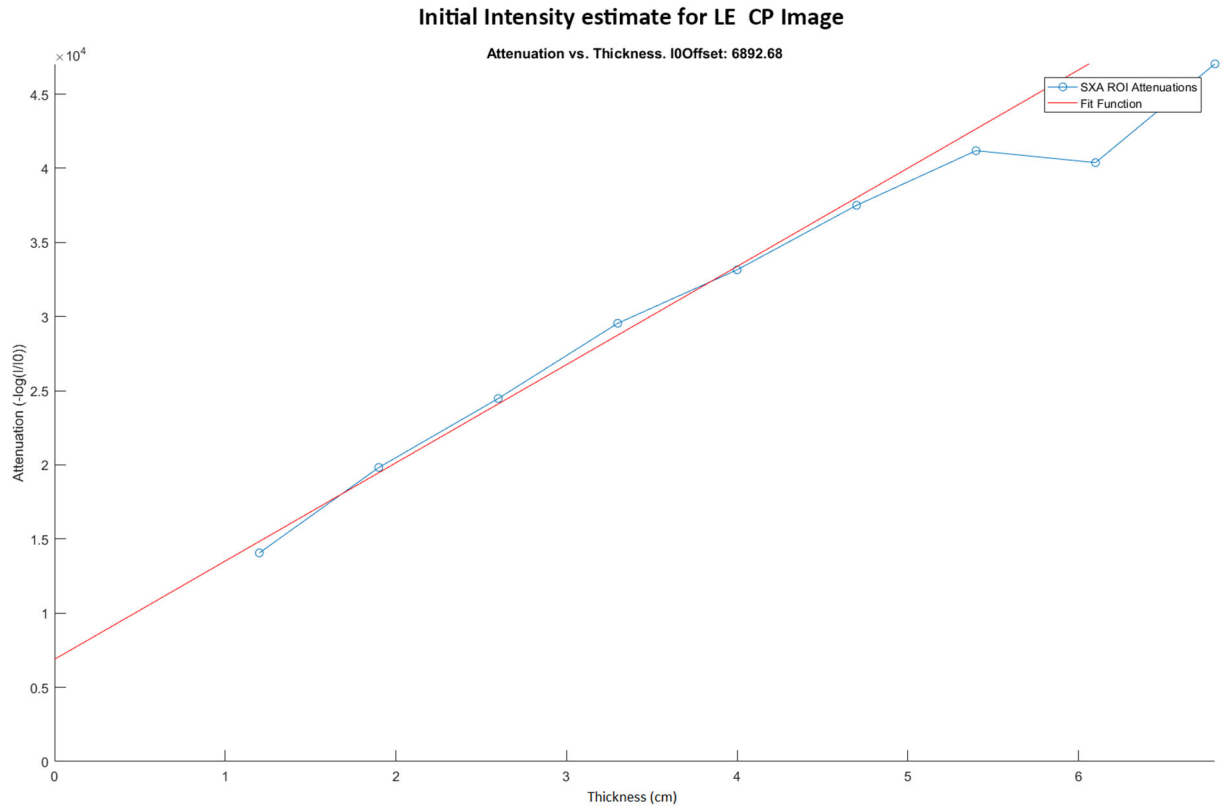


Figure 3.10 LE calibration phantom and breast I_0 derived from SXA phantom

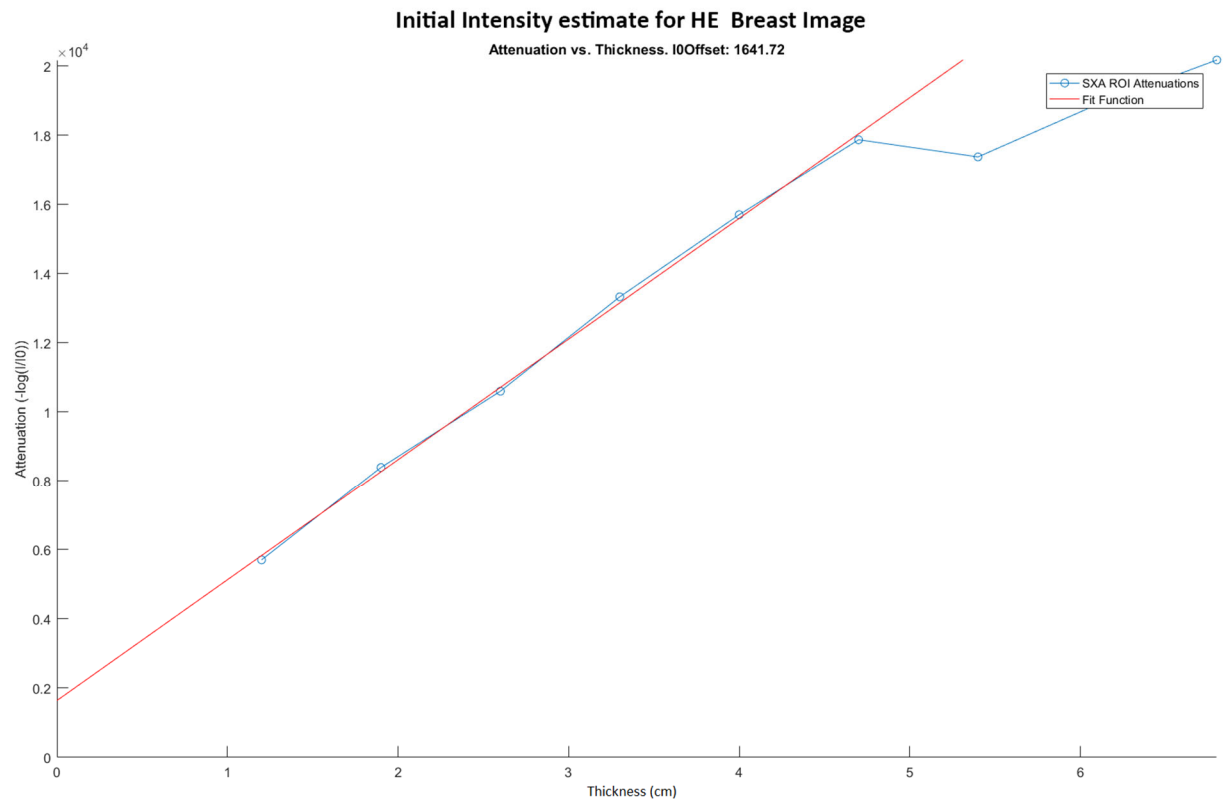
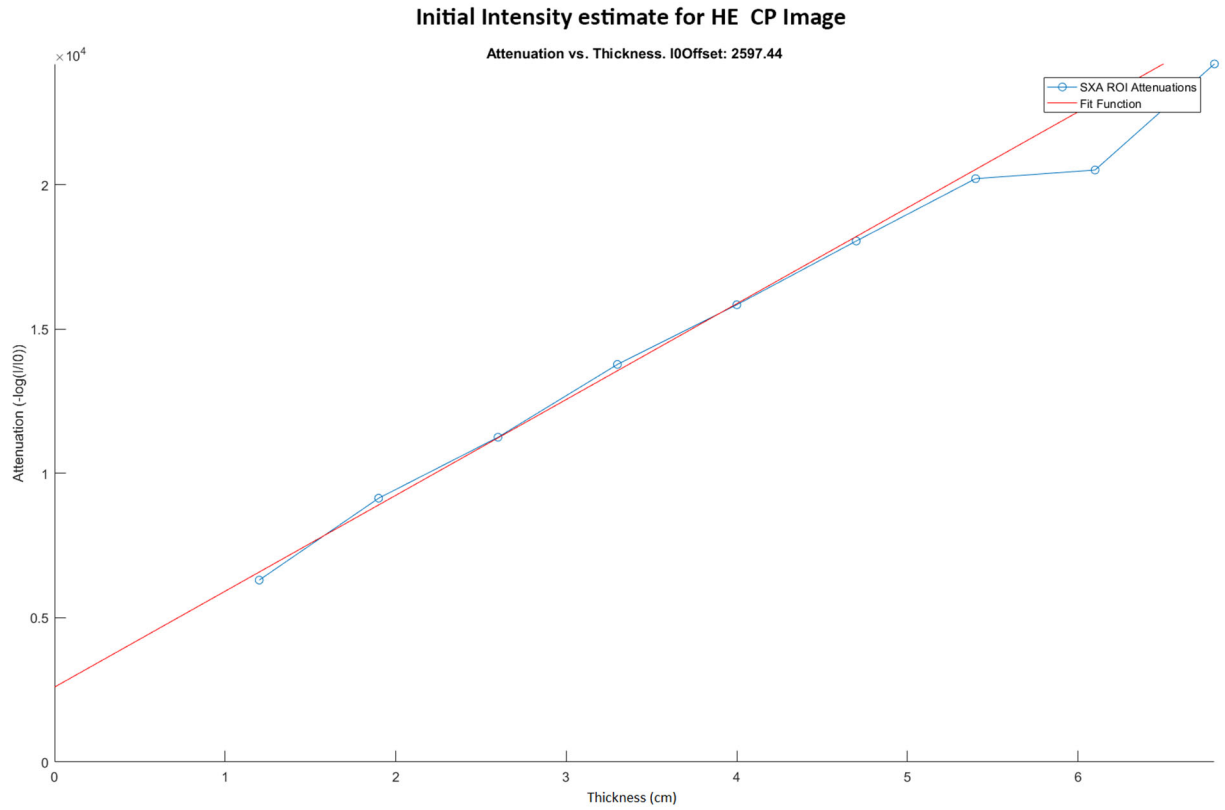


Figure 3.11 HE calibration phantom and breast I_0 derived from SXAI phantom

Discussion

The goal of the above was to create and test methods for estimating nonattenuated photon intensity, I_0 . The experiments for the empirical I_0 model seemed to produce better R v. LE curves for linear mapping estimates. Still, validation with the 2CIP had over 20% $RMSE_p$ for the protein estimates. This could probably be attributed to the linear mapping performing poorly for estimates outside of its calibrated thicknesses, since the total thickness for some of the predictions were 7 cm. When deriving I_0 from the SXA phantom, some of the attenuations at higher thicknesses were not aligned with the rest of the data. This is most likely because the ROIs for these were sampled outside the thickness region. It is, therefore, important to ensure that mapped ROIs are accurate for future fittings, though these did not seem to affect the actual fit since most of the lower thicknesses followed a linear trend. It is recommended to use the I_0 derived from the SXA phantom to estimate I_0 , since it is a measured prediction from the same image as being predicted. If the SXA phantom is not available, however, a robust empirical I_0 model using more sample points at varying mAs and taken at different days should be made for every scanner. Even then, a mechanism to calibrate and validate the empirical model would most likely be necessary due to quantum fluctuations in X-ray scanners.

Chapter 4 3CB Tomosynthesis

Introduction

Tomosynthesis is an X-ray imaging modality that is similar to computed tomography (CT). Fundamental work for tomosynthesis was done in the 1930s, but tomosynthesis did not become clinically relevant until the late 1990s, “when flat-panel radiographic detectors were introduced.”[56] One of the main differences between CT and tomosynthesis is the sweep angle; CT sweeps at 180° to fully reconstruct a 3D volume from 2D projections, whereas tomosynthesis sweeps anywhere in the 15° – 50° range to reconstruct a pseudo-3D volume. This pseudo-3D volume creates focal plane “slices” of the imaged object. Since only a limited angle range is scanned, tomosynthesis has anisotropic spatial resolution. The in-plane (x-y direction) spatial resolution can outperform CT, but the z-direction spatial resolution can vary between 1 mm (full-width half maximum of the point spread function) for a 30° sweep angle tomosynthesis scanner and 4 mm for 10° sweep angle scanners.[57] Over the past two decades, research efforts have focused on making tomosynthesis clinically applicable, and there have been numerous studies on evaluating its applicability to breast cancer detection and diagnosis.

One of the largest retrospective reading studies of 7060 patients that compared digital breast tomosynthesis (DBT) to FFDM found that the sensitivity of DBT was 89% and 87% for FFDM, which showed “borderline significant improvement ($p = 0.07$).”[58, 59] As noted by Gilbert *et al.* in their review, several other studies show similar or improved sensitivity over FFDM. As for specificity, most studies included in Gilbert *et*

al.'s review showed a significant increase: 74% for DBT and 51% for FFDM in one study.[60]

As DBT becomes more clinically prevalent, the 3CB technique should also be able to function with DBT. This chapter covers early investigations into making 3CB applicable for DBT. First, DBT imaging parameters—including filter type and thickness—for 3CB HE images are investigated. The second part of this chapter investigates potential methods for determining breast thickness, which is an essential part of the 3CB technique, from DBT projections.

Part I: Optimizing filter and imaging parameters for high-energy projections

The goal of this experiment was to find the optimal filter and imaging parameters to use for acquiring HE DBT projections. For commercial tomosynthesis scanners, such as GE SenoClaire, the peak energy available for scanning is higher than FFDM (49 kVp vs. 39 kVp). This allows for more energy separation between the LE and HE images, creating greater orthogonality/uncorrelation between measurements and, thus, solutions. Using higher peak energies, however, can also increase patient dose. One 3CB constraint is that the dose of the HE image should be approximately 10% of a regular diagnostic exam dose (i.e., 3CB LE image dose) while optimizing image contrast-to-noise ratio (CNR). Here we investigate this and recommend a filter for acquiring HE DBT projections.

Methods

All images for the measurements below were acquired using GE Healthcare (Chicago, IL) SenoClaire DBT. This scanner acquires nine projections over a 25° sweep angle. At first, both aluminum and copper filters were considered. After cursory simulations, however, it was determined that an aluminum filter would have to be approximately 12 cm thick, which is clinically impractical. Copper filters were considered as the choice material since they attenuate X-ray intensity at a higher rate than aluminum, are readily available, and are cost effective.

Average Glandular Dose

The average glandular dose (AGD) is defined as $D_g = D_{gN} * k$ where k (mGy) is the incident air kerma at the entrance surface of the breast and D_{gN} (mGy/mGy) is the normalized glandular dose coefficient.[61] Tables of D_{gN} values were computed by GE Healthcare for Rhodium-Rhodium anode-filter combinations, 49 kVp, 2-9 cm breast thicknesses, and 0, 50, and 10 % breast glandularity. Extrapolations were computed from these tables to obtain values for all relevant copper thicknesses. Along with AGD, corresponding half value layer (HVL) values for Cu filter thicknesses were also measured. In our experiments, $HVL = \frac{\ln 2}{\mu}$ was computed by measuring the air kerma of aluminum, plotting this value as a function of aluminum thickness, and obtaining the attenuation coefficient μ by fitting an exponential function to corresponding plots. All air kerma values were measured using Radical Corporation (Monrovia, CA, USA) model 1515 ion chamber. Two measurements were performed for estimating the AGD of 3CB HE images. The goal for the first measurements was to determine optimal mAs for a 4 cm breast with 50% glandularity. The goal for the second measurements was to

compute the dose for additional breast thicknesses using the optimal mAs obtained from the first measurement.

CNR

A GEN3 phantom—which is a step phantom made of Plastic Water® and machinable wax to mimic the water and lipid compartments—was used to acquire CNR measurements. Ideally, these represent the two bounds for contrast found in 3CB images, so the aim was to maximize this contrast. A BR3D phantom, which mimics adipose and fibroglandular tissues, was used to obtain imaging settings (kVp, mAs, and target-filter combinations) for the GEN3 phantom images. Tomographic images of the BR3D phantom were first acquired, and then single 2D projections of the GEN3 phantom were taken using these imaging parameters. The mAs parameter was reduced 9-fold for the 2D projections since each DBT sweep acquires nine projections. CNR was estimated by sampling the 2, 4, and 6 cm regions of the GEN3 phantom that contained either pure Plastic Water® or machinable wax (see Figure 4.1). The background of the GEN3 images were sampled for noise estimates (i.e., denominator) using the equation

$$CNR = \frac{(R_L - R_W)}{\sigma_{BKG}}$$

where R_L is the lipid compartment (machinable wax) intensity ratio of the LE and HE GEN3 phantom images, R_W is the water compartment (Plastic Water®) intensity ratio of the LE and HE GEN3 phantom images, and σ_{BKG} is the standard deviation of the noise in the image. The intensity ratio between LE and HE images was used since 3CB images are computed using both LE and HE images. Normalized CNR was also computed using the equation

$$CNRN = \frac{CNR}{\sqrt{AGD}}$$

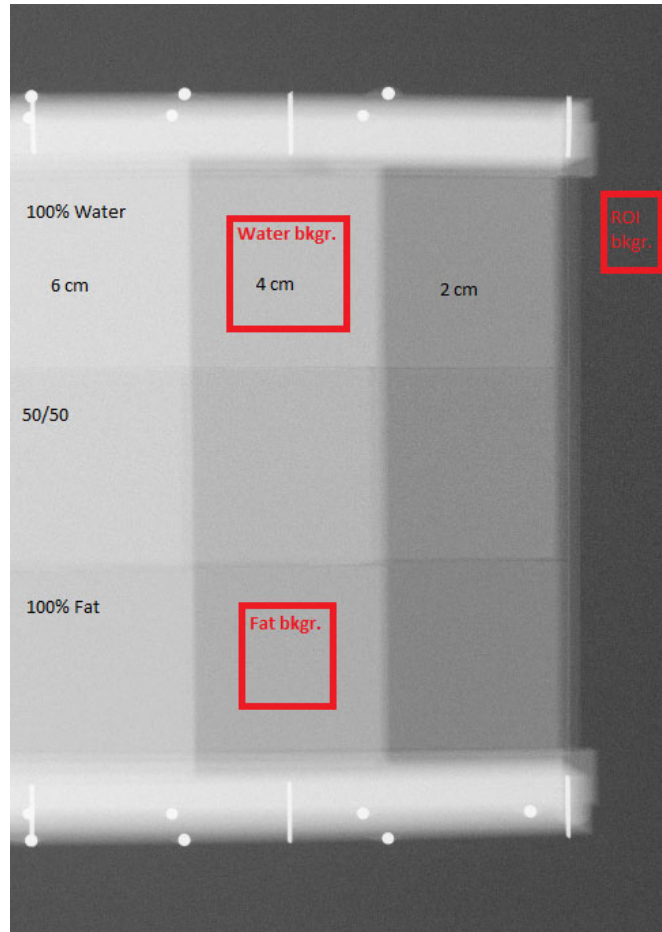


Figure 4.1 A projection of the GEN3 phantom showing sampled regions of interest.

Results

Figure 4.2 and Figure 4.3 show the AGD estimates and HVL plots for the first set of AGD measurements. For the AGD estimates, the lowest available mAs for tomo (36 mAs total) was used. An additional mAs (71 mAs) was also measured for Cu thickness = 0.4064 mm. For the HVL estimates, all exponential fits had $R^2 > 0.99$, indicating little error in air karna measurements. Unfortunately, time constraints (a limited window was

given to perform air kerma measurements during patient hours) did not allow HVL estimates for all copper filter thicknesses. The 71 mAs setting was chosen as optimal since it optimizes for CNR and falls within the 10% of LE AGD constraint.

LE and HE Dose (Dg) Estimation 4 cm Breast, ~50 % Glandularity

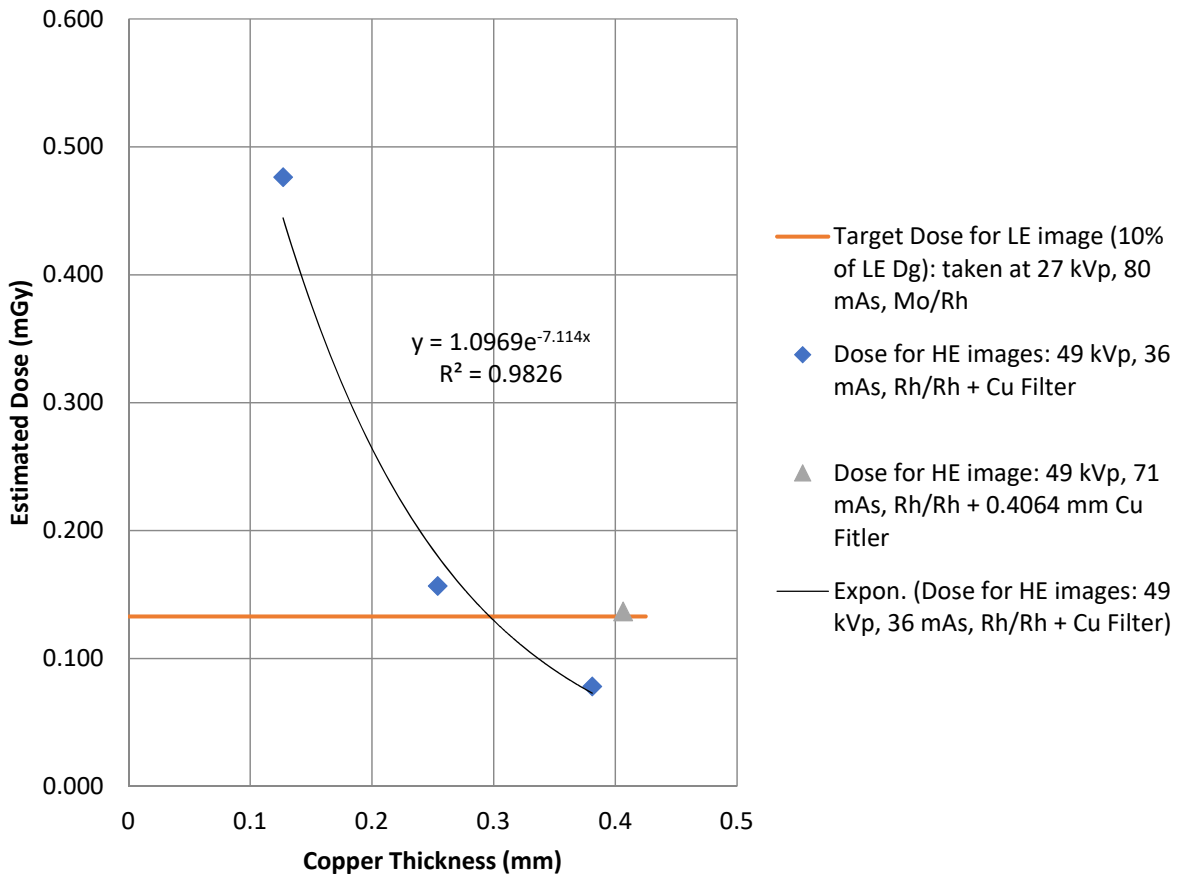


Figure 4.2 LE and HE AGD estimates for a 4 cm thick, 50 % glandularity breast for the first set of AGD measurements.

HVL Estimation Rh/Rh, 49 kVp, 36 mAs

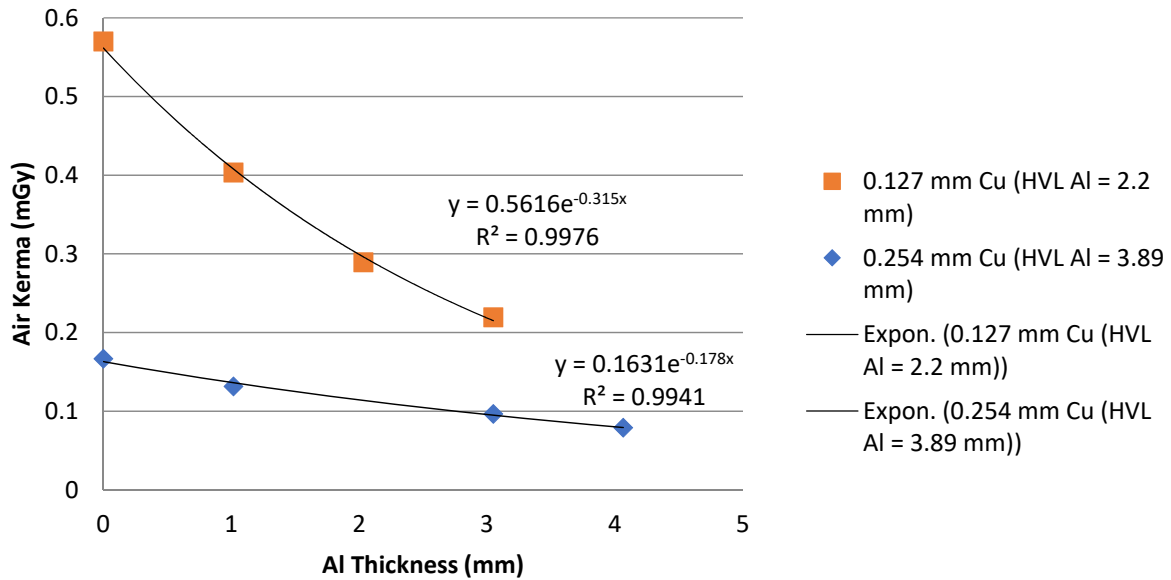
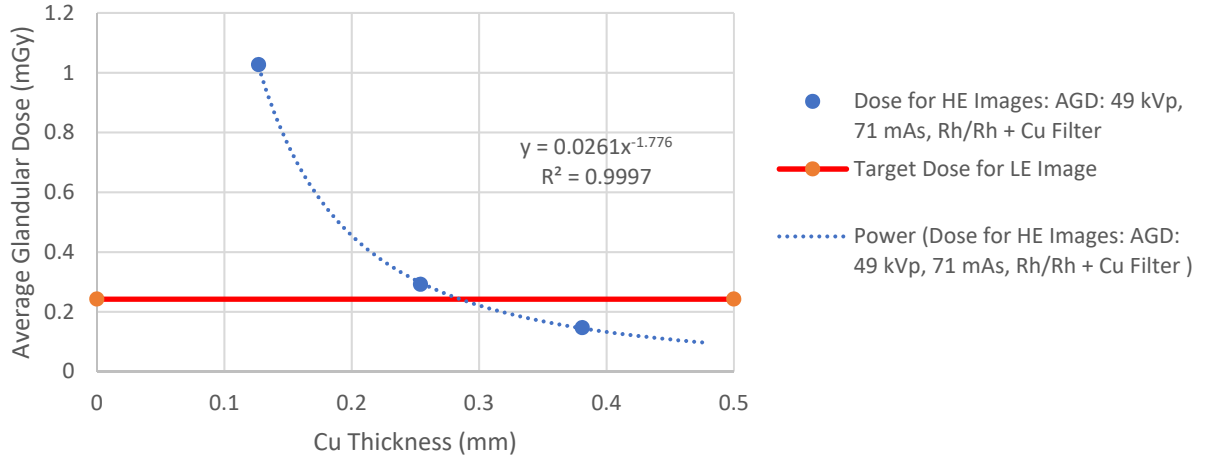


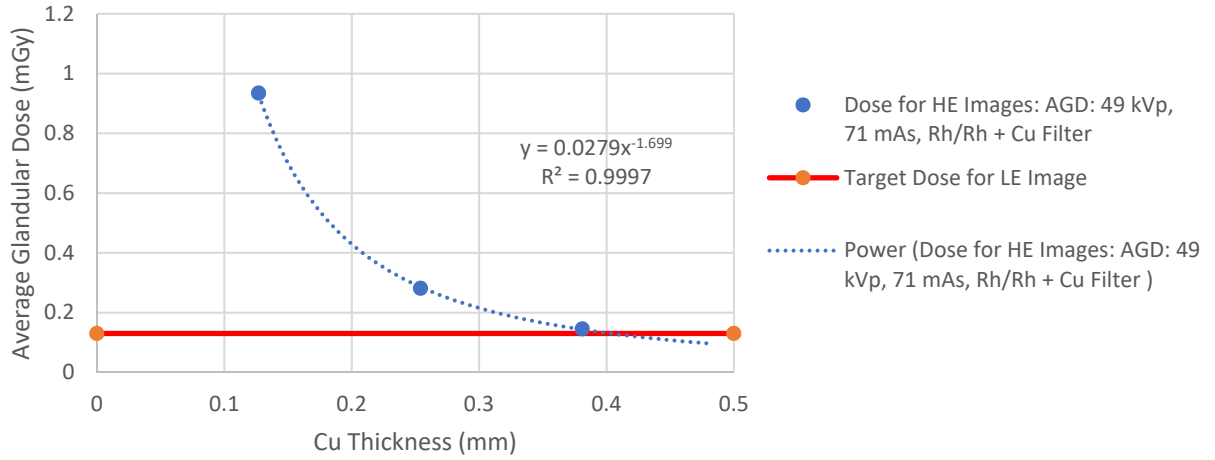
Figure 4.3 HVL estimation plots (air kerma vs. aluminum thickness) for first set of AGD measurements.

Figure 4.4 and Figure 4.5 show the results for the second set of AGD measurements. For the AGD estimates, all power fit curves had $R^2 > 0.99$. Copper filter thickness selection seems to be constrained by the 6 cm dose value since optimizing for one based on the 10% of LE AGD target dose from this measurement would satisfy the LE AGD target for smaller breast thicknesses. For the HVL estimates, all exponential fit curves had $R^2 > 0.98$.

AGD for 2 cm Breast, 50 % Glandularity



AGD for 4 cm Breast, 50 % Glandularity



AGD for 6 cm Breast, 50 % Glandularity

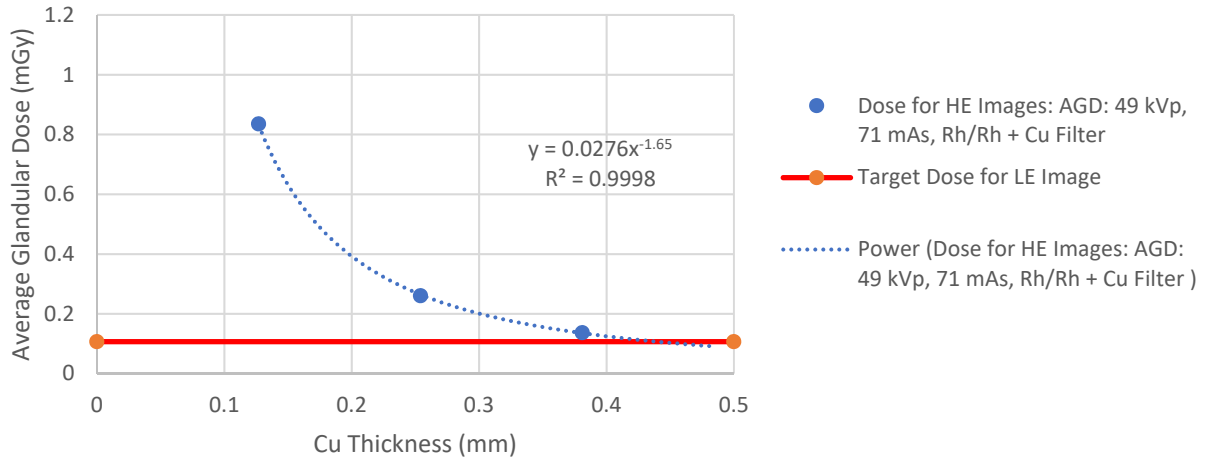


Figure 4.4 LE and HE AGD estimates for 2, 4, and 6 cm thick, 50 % glandularity breasts for the second set of AGD measurements.

HVL Estimation Rh/Rh, 49 kVp, 71 mAs

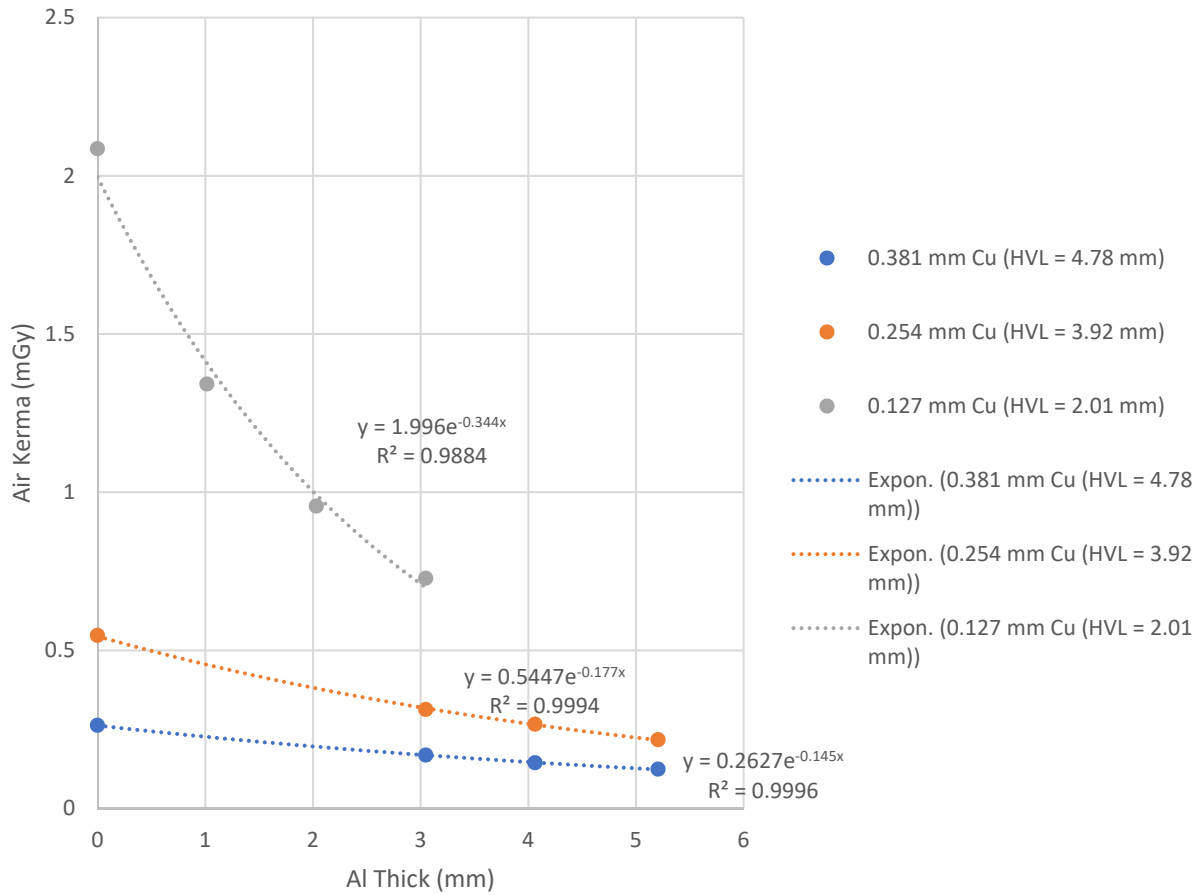


Figure 4.5 HVL estimation plots (air kerma vs. aluminum thickness) for second set of AGD measurements

Table 4.1 shows the imaging parameters for the acquired CNR images.

Table 4.1 Imaging Parameters for CNR Images

Breast Thickness	kVp	Cu Thickness (mm)	mAs	Anode	Filter
2	26	0	5.1	Mo	Mo
4	29	0	5.9	Rh	Rh
6	31	0	9.5	Rh	Rh
2/4/6*	49	0	8	Rh	Rh
	49	0.127	8	Rh	Rh
	49	0.254	8	Rh	Rh

49

0.381

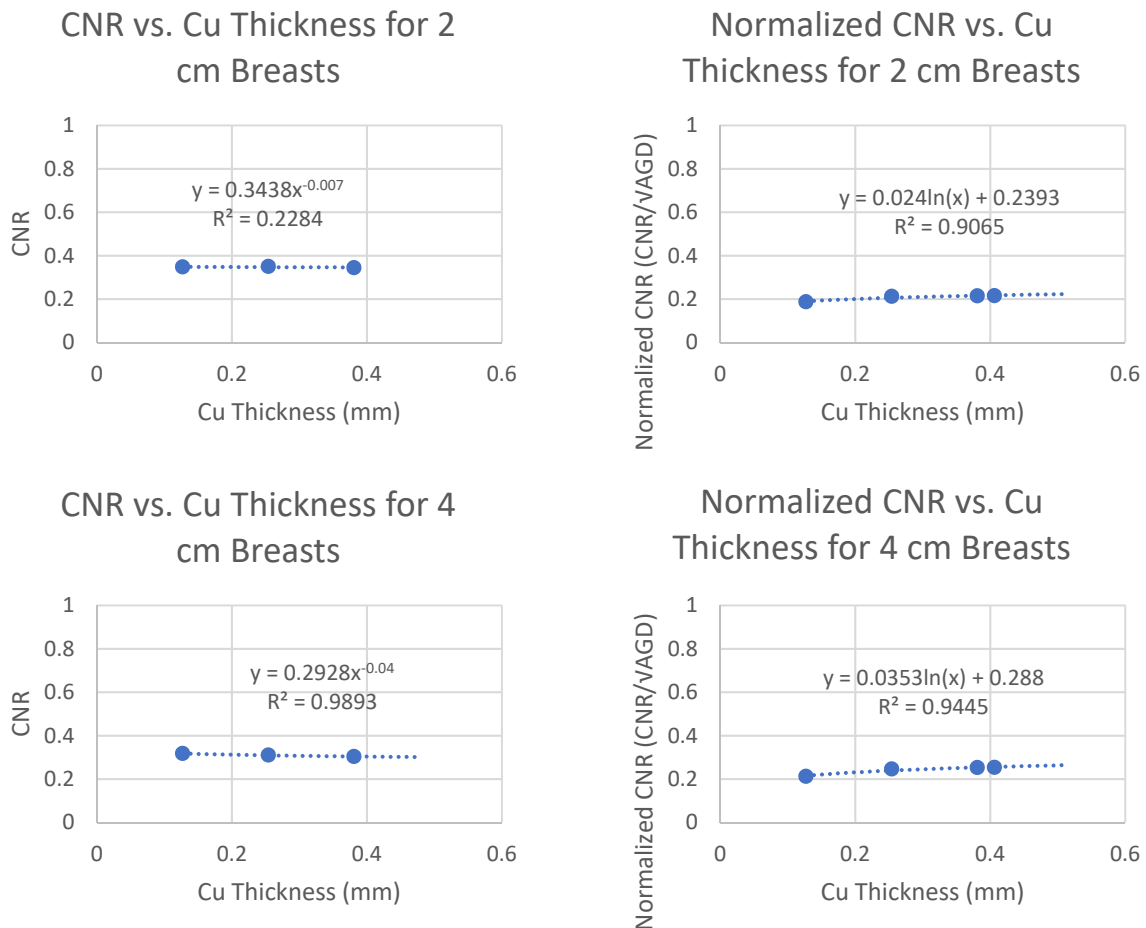
8

Rh

Rh

*kVp is set to 49 for the HE images, so breast thickness does not affect HE kVp

Figure 4.6 shows plots of the CNR and CNRN estimates for 2, 4, and 6 cm breast thicknesses. In all thicknesses, CNR and CNRN estimates are within 15% of each other for all measured values (0.127, 0.254, and 0.381 mm). The fourth point shown (Cu thickness = 0.4064 mm) in the CNRN plots is an extrapolated value from the fit equation derived from the plotted measurements.



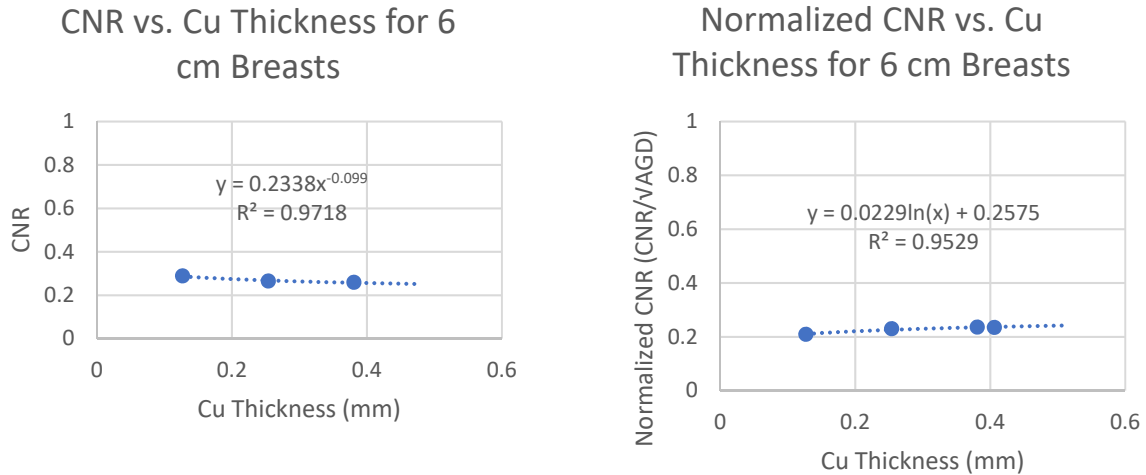


Figure 4.6 The CNR and Normalized CNR for varying breast thicknesses.

Discussion

In the above experiments, the main goal was to optimize imaging parameters and a filter for HE 3CB images. A Cu filter of 0.4064 mm (16 mils) seems to be optimal in terms of meeting dose requirements, availability, and CNR. Imaging at 71 mAs optimizes CNR while satisfying dose requirements. One limitation of this study is that breast thicknesses higher than 6 cm, which can be found in clinical practice, were not considered. It would be valuable to see if dose requirements are met using a 0.4064 mm filter at 71 mAs exposure time for thicker breasts. Lastly, it is extremely important to note that when acquiring HE 3CB images, technicians must ensure that the Cu filter is installed. If the Cu is not installed, the given dose to patients would be approximately 10 times the LE image dose.

Part II: Methodology for determining 3D breast thickness from raw tomosynthesis projections

One important aspect of the 3CB technique is breast thickness estimation. For FFDM 3CB, an SXA phantom is used to estimate breast thickness using known geometric positioning of the phantom and then determining the paddle tilt angle and .[Check Supplement submission to see what I wrote in there about this]. Since DBT acquires multiple projections during its sweep, however, it may be possible to estimate breast thickness from these raw projections. The main goal of the following experiments was to identify possible variables for accurately estimating breast thickness from DBT raw projections.

Methods

The ASTRA *Toolbox* (Vision Lab, University of Antwerp, Belgium and Centrum Wiskunde & Informatica (CWI) in Amsterdam, The Netherlands) was used to create simulations in MATLAB (Natick, Massachusetts, USA) software. It is “a software platform to address the need for a flexible, efficient, and easy to use development platform for tomographic algorithms.”[62, 63] The geometry for the simulations was meant to replicate a typical DBT imaging modality and is shown in Figure 4.7. Sinograms were created from the simulated tomosynthesis projections of a breast-like object. Examples of sinograms for CT and DBT scans are shown in Figure 4.8.

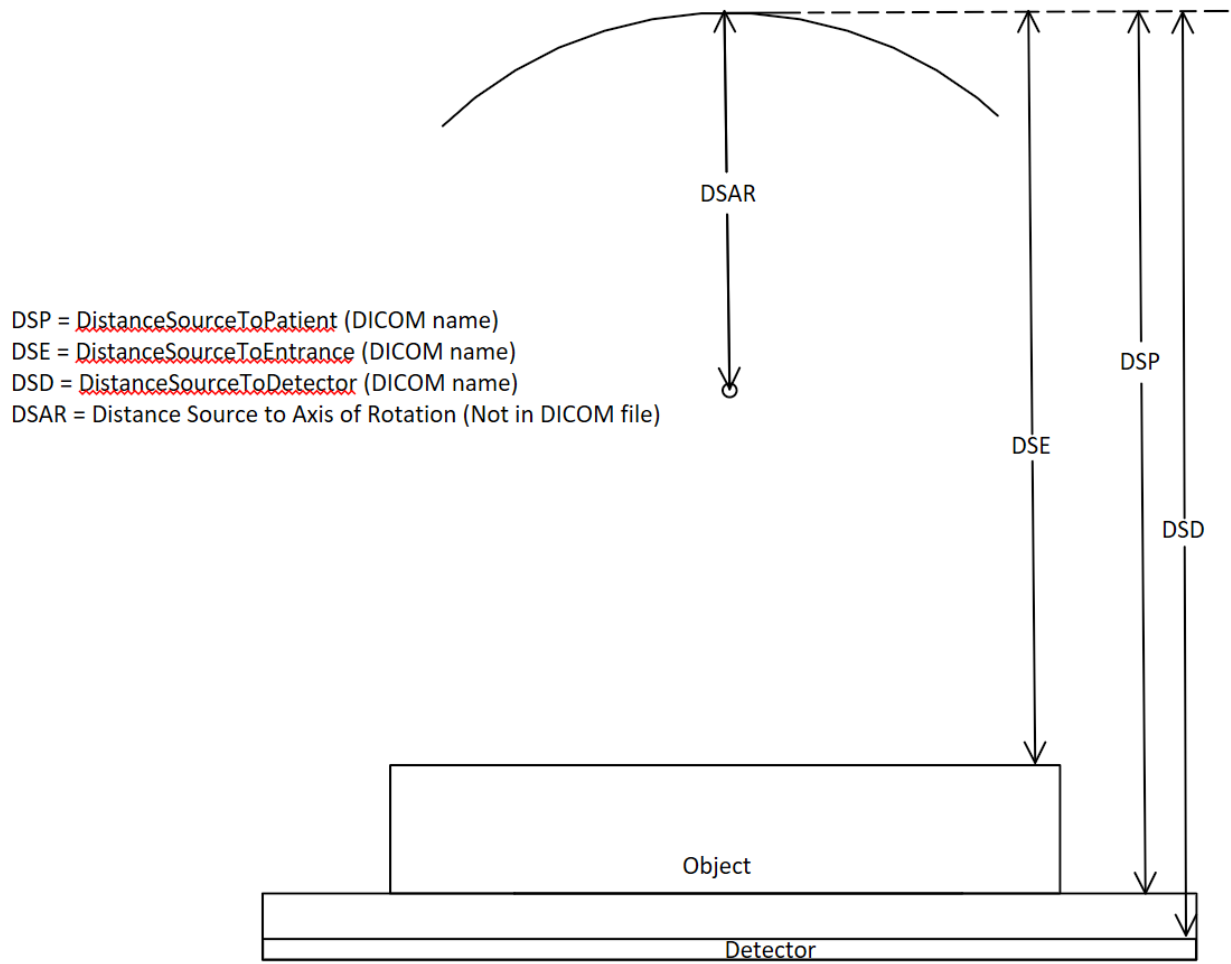


Figure 4.7 ASTRA toolbox experiment imaging geometry and parameters.

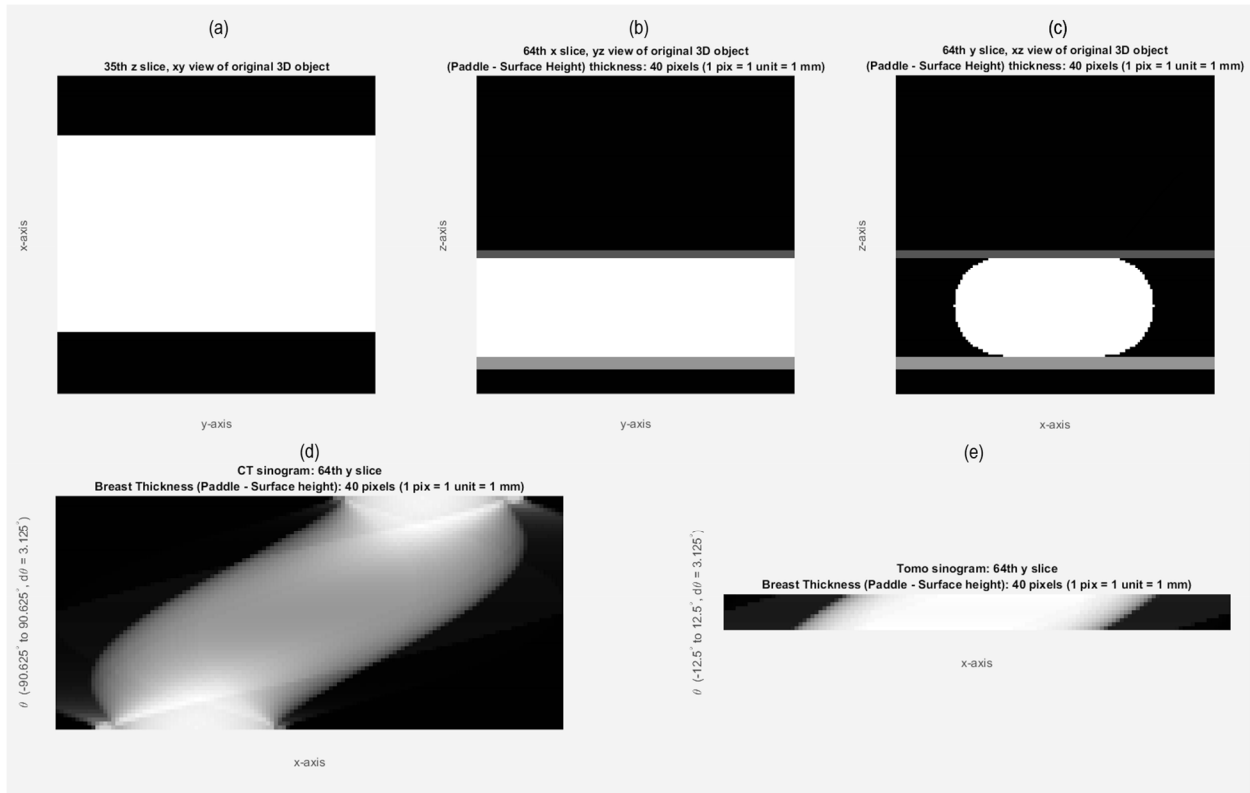


Figure 4.8 Example sinograms of a simple breast phantom for CT and DBT simulations. (a), (b), and (c) show the top, side, and front views of the geometry of the object. (d) shows a sinogram made from a simulated CT scan with 59 projections over a sweep angle $\theta = 180^\circ$ ($d\theta = 3.125^\circ$). (e) shows a sinogram made from a simulated DBT scan with 9 projections over a sweep angle $\theta = 25^\circ$ ($d\theta = 3.125^\circ$).

Sinograms were selected for investigation because they contain z-direction (the axis perpendicular to the detector plane) geometric information about an imaged object. It was hypothesized that by varying breast thickness, intensity (i.e., breast density), and diameter of simulated DBT projections, sinograms would contain information that correlated with breast thickness. Initial investigations sought to see if these parameters could be minimized with an error function. Next, ten random breast sinograms were generated by varying breast thickness, intensity, and diameter from simulations to see if it was possible to solve for these parameters. An iterative method solved for these by minimizing RMSE between a randomly generated sinogram and a library of generated

sinograms. To aid in finding the global minimum instead of an erroneous local minimum, only sinograms with breast parameters that were within 2 mm, 5mm, and 10 of the breast thickness, diameter, and intensity were searched. In real-world applications, these initial parameters would be the breast thickness information from the DICOM image header (e.g., the variable `BodyPartThickness`), the breast diameter derived by measuring breast thickness from the perpendicular tomo projection ($\theta = 0^\circ$), and breast intensity from the average intensity of the breast.

Results

Figure 4.9 shows the cross-sectional view and sinogram of simple a breast object of varying thickness that was generated using the *ASTRA Toolbox*. The parameters for the top figures are 20 mm, 100 mm, and 200 for breast thickness, diameter, and intensity, respectively. The bottom figure varied only in breast thickness (60 mm). Note the difference in the edges between the two sinograms. The 60 mm breast thickness sinogram seems to have a smaller difference between the starting (left) edge value of the first projection (x-axis value = 68) and the ninth (x-axis value = 59). This difference approximately doubles for the 20 mm breast (x-axis value = 68 for the first projection and x-axis value = 49 for the ninth).

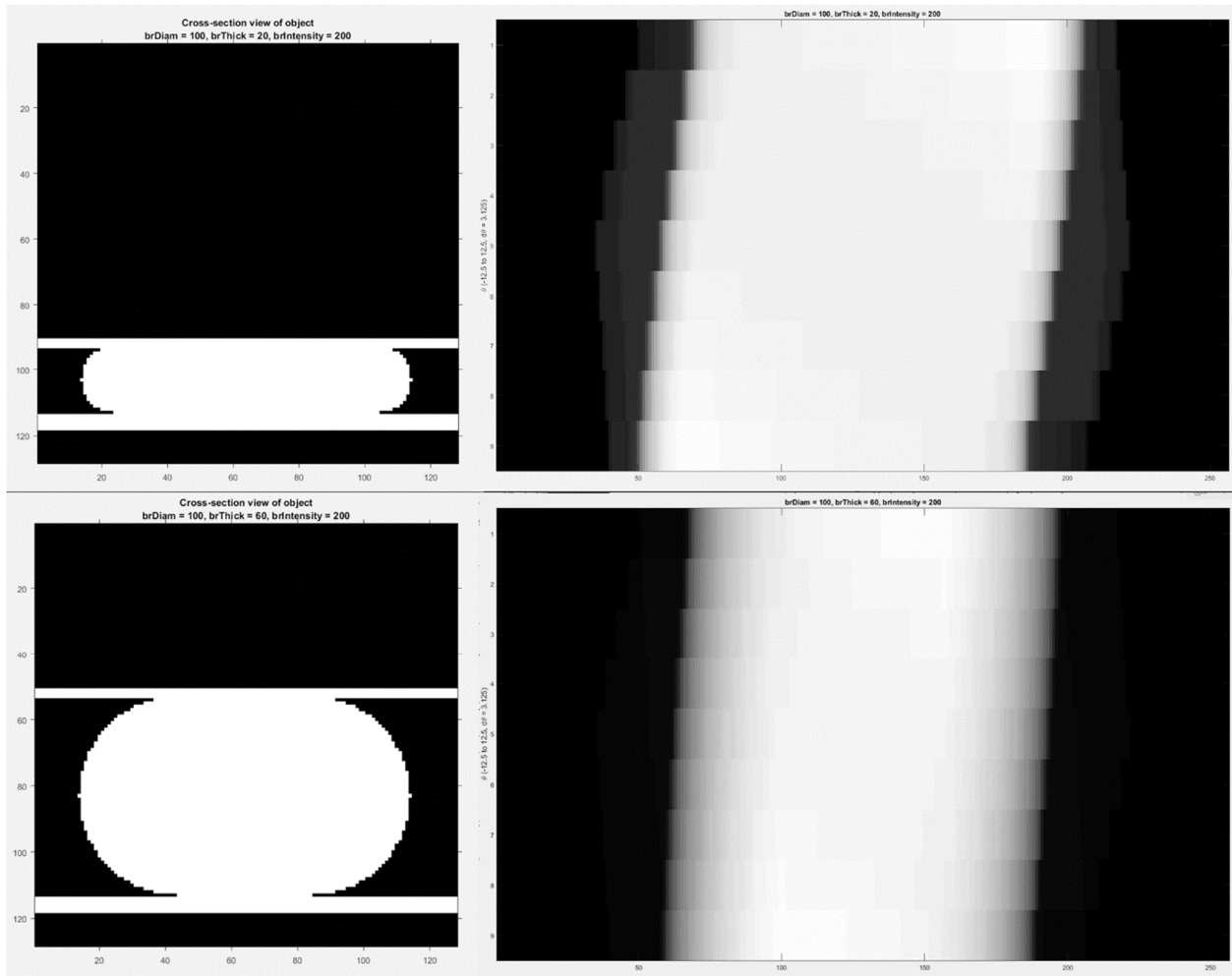


Figure 4.9 Cross-sectional view and sinogram of simple a breast object of varying thickness (top thickness = 20 mm, bottom thickness = 60 mm).

Figure 4.10 summarizes the feasibility of a using an error function to minimize the simulated breast parameters. For each plot, one parameter varied while the other two were held constant. Minima are found for the three parameters for a simulated breast sinogram. After these initial findings, the RMSE was computed between a sinogram of randomly generated breast parameters and a library of sinograms. The iterative method varied all three parameters in each iteration and is shown in Figure 4.11. The estimated minima are found for each iteration (top, middle, and bottom plots). The target values for breast thickness, diameter, and intensity were 53 mm, 77 mm, and 200, respectively.

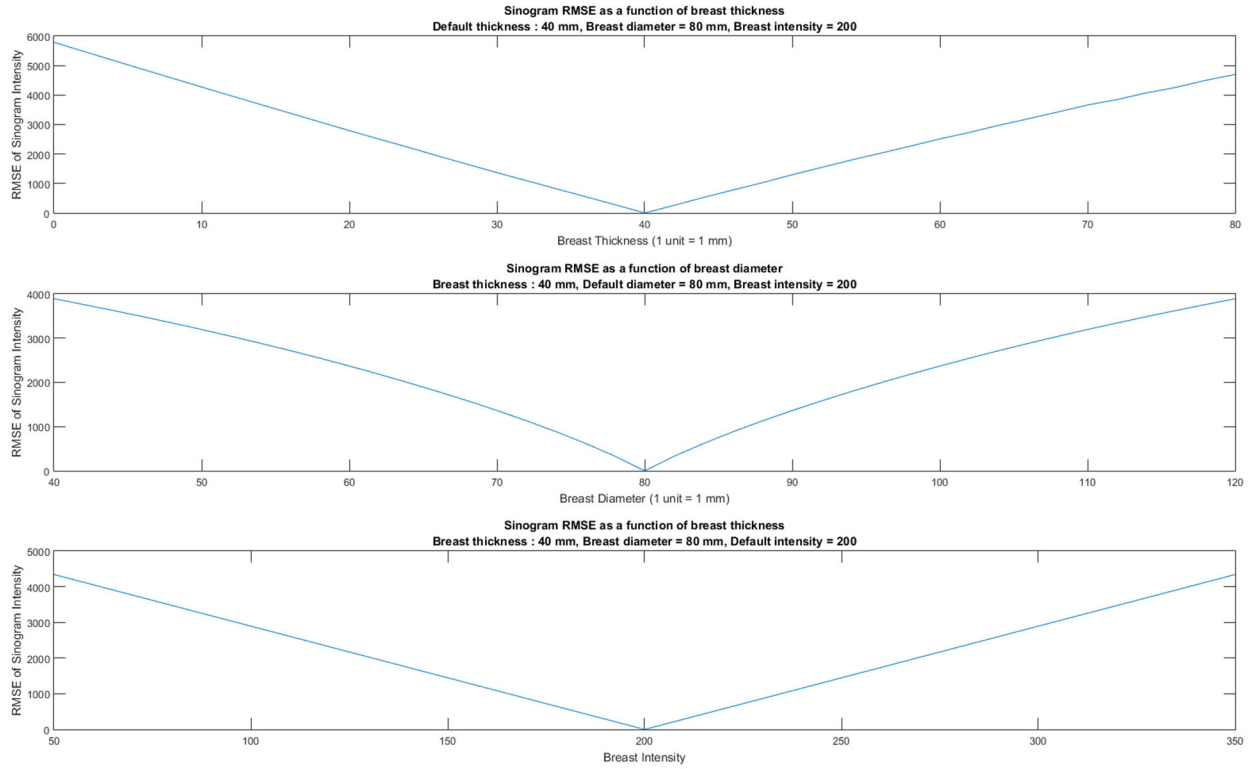


Figure 4.10 RMSE of a pre-selected breast sinogram and generated sinograms of varying breast parameters.

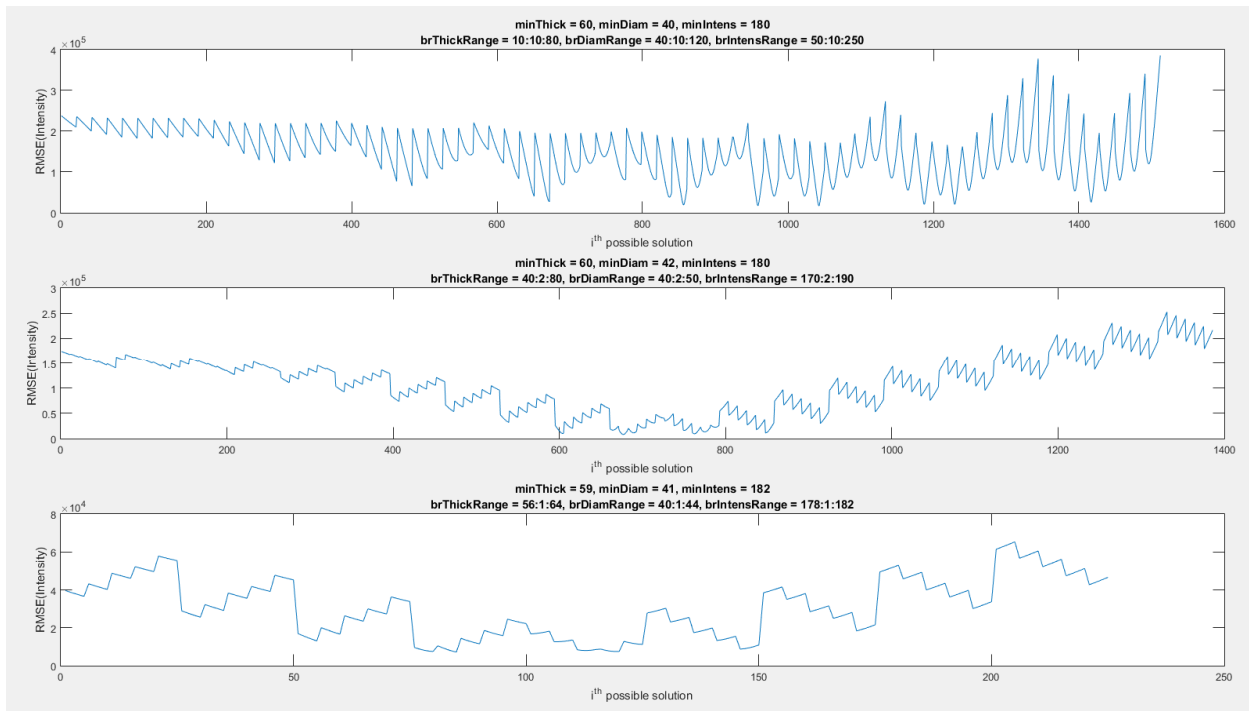


Figure 4.11 The RMSE between a sinogram of random breast parameters and a library of sinograms for an iterative method.

Figure 4.12 top plot shows the parameters for the ten breast sinograms that were generated, and the bottom plot shows the error between actual and iteratively-found estimates. In all cases, the iterative method had the most error in the intensity parameter. Estimated breast thicknesses and diameters were within their search range, ± 2 mm and ± 5 mm, respectively.

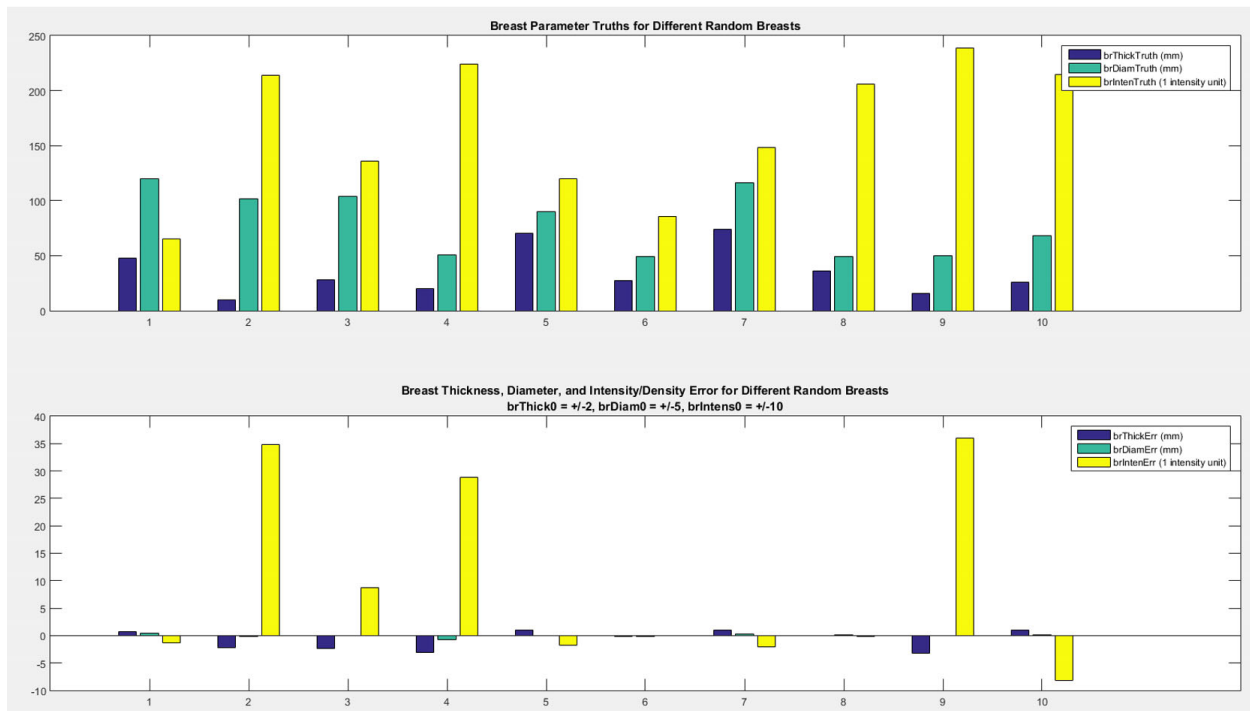


Figure 4.12 (Top) Breast sinograms of randomly generated thickness, diameter, and intensity parameters and (Bottom) the error between actual and iteratively-found estimates.

Discussion

The above investigations sought to derive potential variables of interest as predictors of breast thickness from raw DBT projections using the *ASTRA Toolbox*. Thickness estimates derived through an iterative search method seem promising, though the search method found it difficult to accurately estimate the breast intensity parameter. Since intensity had a larger search range (± 10), it is probably more likely to find a local minimum instead of the global one. From Figure 4.9, however, sinogram edges could potentially be used as a predictors of breast thickness estimates from raw DBT projections.

Chapter 5 Accurate body composition estimates from whole-body silhouettes

Dual-energy X-ray Absorptiometry (DXA) has been widely used to study body composition, and obesity has been linked as a major risk factor for cancer.[64] More specifically, large epidemiological studies have "...found that overweight or obese women are at increased risk of developing postmenopausal breast cancer." [65] In addition, current trends show that endocrine-based mechanisms may act as mediators in the link between obesity and breast cancer for postmenopausal women.[66-68] Moreover, monitoring and maintaining a lean body may offer "...a way in which [postmenopausal-]women can modestly to significantly reduce their relative breast cancer risk." [66] Although unrelated to three-compartment breast imaging, here a method is described that could potentially help monitor lean mass from 2D optical images, which was developed by Avila *et al* during his graduate studies.[69]

Introduction

With the globalization of high-caloric foods, the rate of obesity in children of developing regions such as Southeast Asia and China has increased from 2 to 10% over the last 20 years.[70] In many developing countries, there is a dual burden of malnutrition, where under- and over-nutrition occur simultaneously.[71] Body mass index (BMI) is often used as a measure of under- and over-nutrition since it describes the body weight relative to height and it can be measured with little or no cost. Studies have shown that increased BMI is associated with increased risk for diabetes[72] and metabolic syndrome;[73] however, because BMI is only a measure of overall insufficient

or excess weight, it does not discern the relative amounts of fat and lean mass .[74-76] For example, there can be a two-fold variation in fat mass for a given BMI in children.[77, 78] Furthermore, the distribution of fat changes in children and adolescents throughout their development, and BMI cannot directly monitor these changes.[78] The relationship of BMI to percent body fat changes as a function of age and sex.[79] Must and Anderson have suggested using BMI Z-scores (BMIZ) instead of BMI to represent what is normal for BMI as a function of age and sex trends[80], and BMIZ is commonly reported instead of BMI in pediatric studies.

Unlike BMI and BMIZ, the fat mass index (FMI, kg/m^2) and fat-free mass index (FFMI, kg/m^2) describe body mass in terms of fat and lean masses independently. FMI is a significant determinant of diabetes type and overcomes the limitation of BMI and BMIZ not directly measuring fat and lean masses.[81] FFMI is associated with strength and muscle mass and is used in sarcopenia prediction models.[82]

To measure FMI and FFMI, total body mass must be subdivided into fat and fat-free masses. Previous approaches to measuring FMI and FFMI include bioelectrical impedance analysis (BIA),[83, 84] underwater weighing,[85] air-displacement plethysmography,[86] deuterium dilution,[87, 88] and dual-energy X-ray absorptiometry (DXA).[89-91] Of these, DXA is considered a reference method because few assumptions are made in its determination of fat and lean mass. DXA is not widely used to characterize body composition in large populations or in a clinical setting because the technique is typically more costly than other body composition methods and it uses ionizing radiation.[85] However, all of the techniques listed require measurement

devices that range from thousands to tens of thousands of dollars, making FMI and FFMI impractical in low-resource environments.

An alternative approach is to quantify fat and lean masses using anthropomorphic body shape measures of either skinfold thicknesses or body circumferences. Body shape measures including waist, hip, and thigh circumferences, as well as sagittal abdominal diameter, are already used in epidemiological studies for their high association with diabetes[92] and metabolic syndrome.[93-96] In adult models of metabolic syndrome, BMI loses its predictive power when waist circumference is added to the model.[97] Skinfold thicknesses provide an estimate of subcutaneous fat thickness by measuring the thickness of pinched (doubled over) skin, but models of whole body percent body fat derived from skin fold thickness are not accurate compared to more direct methods like DXA.[98]

In this study, we propose that the silhouette of a person is a reasonable representation of overall body shape, and that shape can be used to estimate fat and lean body masses. Silhouettes, or shadow images that represent the outline of objects, have the advantage of being easily created with minimal processing using low-resolution cameras, which are now ubiquitous. For a proof-of-concept, we created silhouettes from an existing DXA whole-body dataset of a large cohort of children. This approach allows for testing the silhouette imaging concept and its accuracy to DXA before recruiting a large population of children to have new DXA and optical scans. Here we present a method to derive fat and fat-free indices from silhouettes and show their agreement with the true indices acquired using whole-body DXA scans.

Methods

This study is an *in-vivo*, cross-sectional, comparative study using a convenience sample; the sample population of children varies in age, BMIZ, and sex.

Participants

The participants were recruited as part of the Bone Mineral Density in Children Study (BMDCS). BMDCS was a prospective cohort study of 1554 children of mixed ethnicity ranging in age from 5 to 16 years. Begun in 2002 and sponsored by the National Institute for Children's Health and Diseases (NICHD), BMDCS was designed to study the bone health of healthy children as they aged over a 6-year period. The scans used in the present study were the baseline scans from 5 different locations in the United States from July 2002 to November 2003.[89] The selection criteria for the children were defined by the BMDCS through telephone questionnaires and physical examination. A complete description of recruitment and the study has been published.[89] Two hundred children (100 male) were selected to represent a wide range of body shapes and demographic descriptors. Weights were measured on digital scales, and heights were measured using stadiometers. All measures including DXA were acquired while the participants were dressed in examination gowns without shoes. BMIZ for each participant was calculated using growth charts from the Centers for Disease Control and Prevention.[99] Our selection criteria was to choose the extremes (low and high values) for age, height and weight from both sexes, then use a random selection criteria for the remaining individuals.

DXA acquisition

Our selected children were scanned on one of four Hologic Discovery/A systems (Hologic, Inc., Bedford, MA). A fifth BMDCS study site was not used in our pilot because the children were scanned on a Hologic Discovery/W. The DXA scans created using the

Discovery/W have a slightly different projection of the body due to differences in the fan-beam geometry compared to the Discovery/A. All scans were centrally analyzed at the University of California, San Francisco using Hologic Apex 3.0 software. FMI and FFMI were derived from the total body fat and lean masses as follows: $FMI = \text{fat mass}/\text{height}^2$ and $FFMI = (\text{lean soft tissue mass} + BMC)/\text{height}^2$. Note that $BMI = FMI + FFMI$ using this definition. Participants were centered on the scanner table with their arms out to the side and feet pointed downwards, which followed the manufacturer's standard scan and positioning protocols.[100] Further details of the acquisition and analysis procedures are described elsewhere.[89]

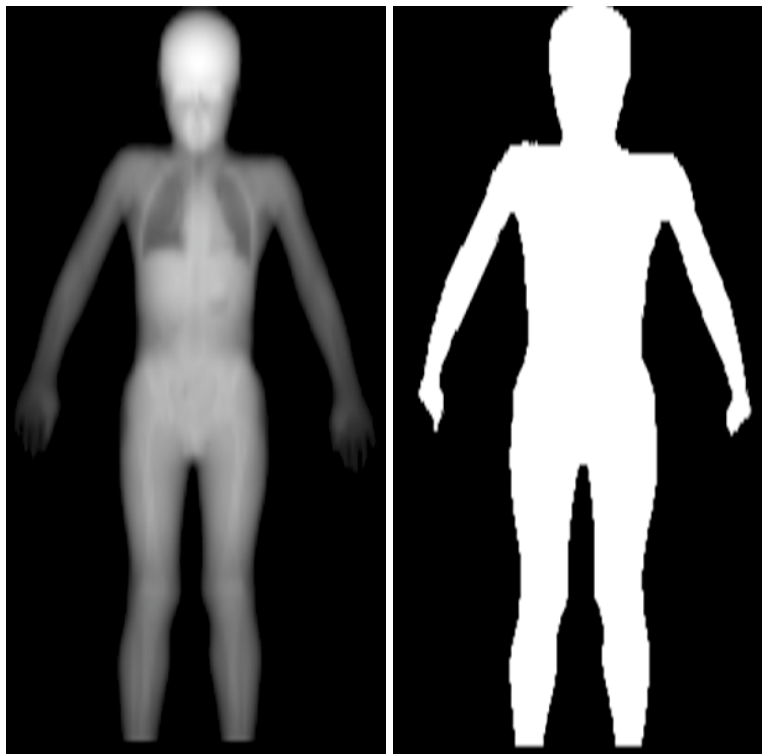


Figure 5.1. (left) Image of the high-energy attenuation portion of the DXA scan. Bone and the density of soft tissue can clearly be distinguished as shades of grey. (right) Silhouette representation of the same DXA image.

Silhouette images

In-house algorithms written in MATLAB (MathWorks Inc.) were used to extract high-energy X-ray attenuation images from raw DXA image files.[101] All pixels above a threshold value defined the silhouette and set to “1”. All pixels with values below the threshold were set to “0” (see Figure 5.1). Linear spatial transformations (translation and rotation) were then used to align all images to each other. Images were then cropped

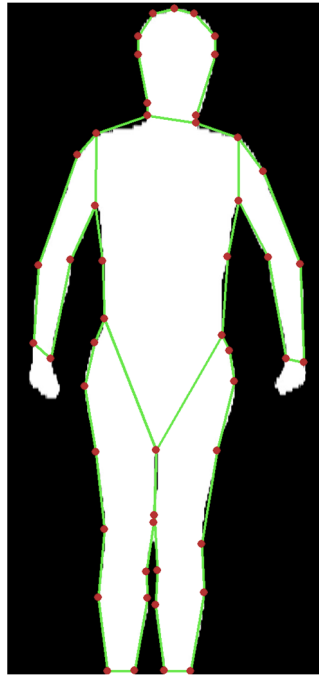


Figure 5.2. Delineation of 50 points of interest on silhouettes for active shape modeling.

above the head to remove unused pixels and at the ankles to remove the variance of the position of the feet. Due to the standardized geometry of DXA device, pixel dimensions were identical across all patients. Quality control was performed on the silhouettes by manually reviewing each and checking for abnormalities in the body positioning that was markedly different from the standard DXA positioning.

Active Shape Modeling

We built a 50-point Active Shape Model (ASM) to describe body shape.[102] See Figure 5.2. The selection criteria for the 50 points were as follows: a) points were placed on vertices along the body outline (inseam, underarms, elbows, etc), b) additional 3-point sets were used to capture major body contours (thighs, shoulders, neck etc.) defining the start, apex, and end of the contour, and c) point locations were picked that were easily visualized such that their placement was accurate and precise across the sample. The 50 points chosen were considered to be the minimum number of points that satisfied these criteria, but an alternative number of points was not tested at this time. The ASM of the silhouettes was built using the active shape modeling toolkit (Visual Automation Limited, Manchester, U.K.), a software program that generates image parameters based on principal component analysis of fiducial markers on images, the details of which can be found in Gregory *et al.*[103] and Cootes *et al.*[102] In brief, the 50 points were manually placed on the first few images. Then, the software used these initial placements to build a limited ASM. With this limited ASM, the software predicted the placement of the points in subsequent images. All points were manually reviewed and adjusted as necessary. This process was repeated, i.e. initial placement by the limited ASM, manual inspection, then the rebuilding of the ASM, for every 10 images analyzed until all of the images were added to the model.

From the dataset formed from the point positions of all 50 points on all images, modes of variation were generated using principal component analysis. The result was a model that described the unique modes of variation in the form of a set of eigenvectors (i.e. modes of variation) where each successive eigenvector explains less of the variation than the previous. By combining the average point placements with the

linear combinations of the eigenvector basis, the location of the fiducial markers for any particular image can be generated. The coefficients that are used in the linear combination (i.e., how much each eigenvector is scaled) are the output parameters of each image. These output parameters were used for statistical analysis. It is convenient to visualize principal components in this context by generating series of shape images in which a single principal component is varied while all others are held fixed at their average value. Such images are shown in Figure 5.3. In each row, the middle image is the overall “average shape” generated from the test data set. Extreme images are generated by varying the principal component of interest to its +3 and -3 standard deviation values and combining with the average image. These extreme images are shown on the left and right of the average image. For example, it is readily apparent that PCA Mode 1 (pc1) captures shape information related to body width and height.

PC#	-3SD	Mean	+3SD	PC#	-3SD	Mean	+3SD
0				5			
1				6			
2				7			
3				8			
4				9			

Figure 5.3. Silhouette representations of the first 10 (i.e. 0 to 9) modes used to model FFMI in both boys and girls. The average silhouette is shown in the middle and the silhouettes representing -3SD (left) and +3SD (right) are also shown.

Statistics

All statistics were performed in SAS version 9.3 (SAS Institute, Cary, NC). The BMDCS study population was separated into two groups by sex. FFMI was defined as $\frac{\text{Lean soft tissue mass} + \text{BMC}}{\text{height}^2} \text{ kg/m}^2$ where BMC = bone mineral content, FMI was defined as $\frac{\text{Fat mass}}{\text{height}^2} \text{ kg/m}^2$, and percent fat was defined as $\frac{\text{Fat mass}}{\text{total mass}} * 100$. Note that BMI = FMI + FFMI using these definitions. The ASM parameters of each silhouette (i.e., the coefficients of the eigenvector basis) were placed in a matrix, with each column corresponding to the principal component number and each row the silhouette number corresponding to each of the children.

Limiting our analysis to the components needed to describe 95% of the image variation, step-wise linear regression with n -fold (leave-one-out) cross-validation (GLMSELECT procedure in SAS) was used to generate a predictive model for FFMI, FMI, and percent body fat. Separate model equations were made from both PCA components and demographic variables. A cross-validation stop criterion was defined on the Schwarz Bayesian criterion (SBC). Statistical significance was defined as the $p < 0.05$ threshold. The final models for FFMI, FMI, and percent body fat were generated using three different approaches. As a reference point, we first derive prediction equations using demographic variables only (age, sex, height, weight, BMIZ). We compared these to equations derived using principal components only. Finally, we combined principal components and demographic variables.

Results

In a total of 200 participants, 11 were excluded during quality control for reasons including movement and poor positioning. Of the remaining 189 participants, 93 were male. The children were mainly white (112) but also include Asian (8), Hispanic (24), and Black (45). Summary statistics about the selected test population are provided in Table 5.1. Twenty-six principal components were required to explain 95% of the variance in silhouette shapes. All subsequent analysis was limited to these 26 components.

Table 5.1. Summary statistics of the test population separated by sex.

Demographic Variable	Girls (n = 96)				Boys (n = 93)			
	Mean	Std. Dev.	Min	Max	Mean (SD)	Std. Dev.	Min	Max
Age (years)	10.3	3	6	16	10.5	3.2	6	16
Height (cm)	141.2	15.5	108	173	144.6	19.3	111	185
Weight (kg)	38.9	14.9	17.2	81.8	40.9	17.7	18.1	87.4
BMI (kg/m ²)	18.8	3.8	13.3	30.1	18.6	3.5	13.7	28.8
BMIZ	0.4	0.9	-1.8	1.9	0.3	1	-2	1.9
FMI (kg/m ²)	5	2.1	2.1	10.4	3.9	1.7	1.7	10
FFMI (kg/m ²)	13.3	2.1	10.4	20.3	14.2	2.6	10.5	21.6
Percent Body Fat	25.5	6.1	14.3	39.3	20.4	6	9.7	38.1

Table 5.2 shows the correlations between the principal components, demographic, and adiposity measures. Several of the components (e.g., pc0, pc1 and pc5) showed significant correlation with multiple demographic and adiposity variables. Additionally, a few components (e.g. pc9) were not found to be significantly correlated with any demographic or adiposity variables. It can be seen in Figure 5.3 that pc9 appears to capture a variance in positioning of the left shoulder, a “tilt” along the longitudinal-axis, irrelevant to our analyses. Other patient positioning artifacts such as arm and leg abduction/adduction can be observed in several of the other principal components.

The body composition prediction equations for boys and girls are shown in Table 5.3 and Table 5.4, respectively. In general, the demographic information only had a modest ability to predict percent body fat in boys and girls ($R^2 = 0.457$ and 0.61 respectively.) Using only principal components to predict % Fat was also modestly correlated (0.73 and 0.59 respectively.) For % Fat, a combination of demographics and principal components created the best models (0.75 and 0.69 respectively). For the boys, the equation (omitted) for %fat (PCA+demo) included two additional PC terms (PC3 and 13) but no demographic variables. These coefficients remained due to the progression of the stepwise selection algorithm and were interpreted as artifacts.

For all measures of FFMI, FMI, and percent body fat, the combination of principal components with demographics performed equally or better than either principal components alone or demographics alone. No conclusion can be drawn whether the principal components alone fare better or worse than the demographics alone. They performed about equally well for % Fat and FMI in girls (Table 5.4) but the principal component alone model performed better for % Fat and FMI in boys (Table 5.3), while the demographics-only model had a slight advantage in FFMI prediction.

Table 5.2. Correlation of the most significant principal components with demographic and adiposity variables (R²).

Principal Comp. #	Age		Height		Weight		BMI z-score		%Fat		FFMI		FMI	
	Boys	Girls	Boys	Girls	Boys	Girls	Boys	Girls	Boys	Girls	Boys	Girls	Boys	Girls
pc0	0.659 [‡]	0.479 [‡]	0.688 [‡]	0.469 [‡]	0.784 [‡]	0.700 [‡]	0.615 [‡]	0.698 [‡]	0.364 [‡]	0.647 [‡]	0.716 [‡]	0.695 [‡]	0.622 [‡]	0.780 [‡]
pc1	0.534 [‡]	0.454 [‡]	0.544 [‡]	0.510 [‡]	0.339 [‡]	0.243 [*]	-0.284 [‡]	-0.374 [‡]	-0.173	-0.286 [‡]	0.137	0.105	-0.100	-0.180
pc2	0.183	0.094	0.210 [*]	0.147	0.170	0.090	0.105	0.000	-0.083	0.051	0.175	0.035	0.023	0.055
pc3	0.069	-0.098	0.081	-0.082	0.116	0.034	0.117	0.316 [†]	0.033	0.266 [†]	0.124	0.065	0.070	0.224 [*]
pc4	-0.261 [*]	-0.189	-0.244 [*]	-0.196	-0.179	-0.055	0.218 [†]	0.249	0.456 [†]	0.166	-0.234 [*]	0.020	0.337 [†]	0.154
pc5	-0.028	0.352 [‡]	0.014	0.307 [†]	0.079	0.388 [‡]	0.228 [†]	0.204 [*]	0.217 [*]	0.193	0.083	0.350 [†]	0.265 [†]	0.300 [†]
pc6	-0.165	0.0003	-0.224 [*]	-0.064	-0.103	0.108	0.195	0.186	0.278 [†]	0.112	-0.059	0.173	0.258 [*]	0.169
pc7	-0.118	-0.176	-0.097	-0.149	-0.183	-0.108	-0.099	0.029	-0.004	0.031	-0.219 [*]	-0.101	-0.085	-0.024
pc8	-0.019	-0.170	-0.039	-0.230 [*]	0.009	-0.174	0.020	0.008	-0.022	-0.011	0.035	-0.132	-0.016	-0.061
pc9	-0.091	0.080	-0.119	-0.042	-0.086	-0.013	-0.009	-0.037	0.106	0.051	-0.073	-0.023	0.078	0.024
pc10	0.152	0.178	0.165	0.219 [*]	0.268 [†]	0.133	0.376 [†]	-0.016	0.319 [†]	0.127	0.260 [*]	0.000	0.413 [†]	0.110
pc11	0.131	0.074	0.107	0.096	0.084	0.062	-0.048	0.054	-0.028	0.046	0.043	0.030	-0.021	0.016
pc12	0.121	-0.165	0.141	-0.258 [*]	0.154	-0.170	0.082	-0.078	-0.134	-0.169	0.184	-0.057	-0.059	-0.148
pc13	-0.120	-0.111	-0.056	-0.114	-0.060	-0.151	-0.001	-0.124	0.273 [†]	-0.107	-0.161	-0.140	0.206 [*]	-0.148
pc14	0.058	0.137	0.051	0.111	-0.006	0.130	-0.216 [*]	0.021	-0.080	0.051	-0.071	0.109	-0.104	0.096
pc15	0.046	0.294 [†]	-0.015	0.204 [*]	0.009	0.195	0.070	-0.039	-0.060	-0.117	0.071	0.224 [*]	-0.041	-0.011
pc16	0.319 [†]	0.164	0.335 [†]	0.157	0.335 [†]	0.111	0.0488	-0.039	-0.288 [†]	-0.158	0.375 [†]	0.141	-0.130	-0.069
pc17	-0.130	0.035	-0.142	0.119	-0.217 [*]	0.133	-0.278 [†]	0.095	-0.043	-0.047	-0.250 [*]	0.171	-0.096	0.046
pc18	-0.044	-0.015	-0.050	0.072	-0.077	0.004	-0.058	0.039	0.005	0.022	-0.078	-0.034	-0.044	-0.015
pc19	0.215 [*]	-0.154	0.142	-0.169	0.155	-0.116	0.090	-0.074	-0.205 [*]	-0.111	0.265 [*]	-0.053	-0.065	-0.075
pc20	-0.059	0.086	-0.078	0.093	-0.053	0.142	-0.180	0.017	-0.018	0.098	-0.097	0.112	-0.017	0.160
pc21	-0.029	0.007	-0.055	0.086	-0.067	0.056	-0.077	0.082	0.090	-0.027	-0.110	0.055	0.040	-0.015
pc22	0.104	0.036	0.032	0.057	0.025	0.023	-0.024	0.012	0.094	0.043	-0.020	-0.007	0.113	0.008
pc23	-0.123	0.232 [*]	-0.153	0.163	-0.111	0.183	0.095	0.130	-0.067	0.019	-0.011	0.256 [*]	-0.067	0.086
pc24	-0.129	-0.076	-0.135	-0.079	-0.188	-0.043	-0.176	0.096	-0.230 [*]	0.110	-0.139	-0.045	-0.275 [†]	0.070
pc25	-0.073	-0.120	-0.067	-0.092	-0.078	-0.177	0.015	-0.146	0.056	-0.170	-0.080	-0.176	0.025	-0.191
pc26	-0.069	0.136	-0.059	0.169	-0.009	0.062	0.099	-0.147	0.052	-0.093	0.024	-0.031	0.069	-0.075

* indicates p<0.05, † indicates p<0.01, ‡ indicates p<0.001

Regression plots of the best models versus the actual measures are shown in Figure 5.4.

Table 5.3 Prediction equations, R² adj. (see definition below table), and root-mean-square error (RMSE), for demographic variables, FFMI, FMI and Percent Fat from PCA modes and demographic information using the boys' data.

Variable (method)	Boys Prediction equation	R ² adj	RMSE
% Fat (demo)	$-94.943 + 1.761*\text{height} - 0.007*\text{height}^2 + 0.44*\text{weight} + 1.421*\text{BMIZ}$	0.457	4.411
% Fat (PCA)	$21.818 + 13.218*\text{pc0} - 6.225*\text{pc1} + 21.929*\text{pc4} + 17.214*\text{pc5} + 14.52*\text{pc6} + 30.348*\text{pc10} - 28.108*\text{pc12} - 49.375*\text{pc16} - 42.53*\text{pc19} + 32.767*\text{pc21}$	0.728	3.119
% Fat (PCA + demo)	(no demographic variables added significantly to the model)		
FMI (demo)	$3.523 + 1.266*\text{BMIZ}$	0.519	1.186
FMI (PCA)	$4.291 + 6.025*\text{pc0} - 1.461*\text{pc1} + 2.45*\text{pc3} + 4.989*\text{pc4} + 6.007*\text{pc5} + 4.508*\text{pc6} - 2.237*\text{pc8} + 8.5*\text{pc10} - 5.873*\text{pc12} - 8.393*\text{pc16} - 6.109*\text{pc19} + 7.043*\text{pc21}$	0.861	0.637
FMI (PCA+demo)	(no demographic variables added significantly to the model)		
FFMI (demo)	$14.979 - 0.061*\text{height} + 0.197*\text{weight}$	0.884	0.875
FFMI (PCA)	$14.043 + 8.538*\text{pc0} + 1.792*\text{pc2} + 3.204*\text{pc3} - 3.863*\text{pc4} + 5.034*\text{pc5} - 5.954*\text{pc7} + 6.664*\text{pc12} - 12.616*\text{pc13} + 17.425*\text{pc16} - 10.531*\text{pc17} + 13.946*\text{pc19} - 9.234*\text{pc21}$	0.822	1.084
FFMI (PCA + demo)	$14.093 - 3.536*\text{pc4} - 3.335*\text{pc10} + 4.013*\text{pc12} - 5.218*\text{pc13} + 7.87*\text{pc16} + 7.814*\text{pc19} - 5.581*\text{pc21} + 0.176*\text{age} - 0.05*\text{height} + 0.126*\text{weight} + 0.692*\text{BMIZ}$	0.946	0.599

demo: R² and RMSE were calculated using only demographic variables

PCA: R² and RMSE were calculated using only the PCA coefficients derived from the active shape model

PCA + demo: R² and RMSE were calculated using both PCA & demo.

R² adi: the coefficient of determination adjusted for the number of parameters used in the model equation.

Table 5.4. Prediction equations, R² adj. (see definition below table), and root-mean-square error (RMSE), for demographic variables, FFMI, FMI and Percent Fat from PCA modes and demographic information using the girls' data.

Variable (method)	Girls Prediction equation	R ² adj	RMSE
% Fat (demo)	23.586 + 5.257* BMIZ	0.606	3.830
% Fat (PCA)	24.998 + 17.594* pc0 - 7.372* pc1 + 11.857* pc3 + 18.405* pc5 + 19.104* pc10	0.586	3.926
% Fat (PCA + demo)	23.577 + 7.099* pc0 + 19.925* pc10 - 18.239* pc15 - 21.687* pc16 - 32.043* pc17 + 4.111* BMIZ	0.691	3.392
FMI (demo)	4.217 - 0.0002422* height ² + 0.137* weight + 0.913* BMIZ	0.851	0.795
FMI (PCA)	4.766 + 7.609* pc0 - 1.022* pc1 + 2.038* pc2 + 3.375* pc3 + 2.599* pc4 + 7.732* pc5 + 6.181* pc6 + 8.311* pc10 - 5.523* pc13 - 5.651* pc17	0.886	0.694
FMI (PCA+demo)	5.19 + 1.43* pc0 + 5.079* pc10 - 3.931* pc12 - 4.834* pc15 - 4.907* pc16 - 6.405* pc17 - 5.28* pc19 - 0.00032333* height ² + 0.153* weight + 0.586* BMIZ	0.895	0.667
FFMI (demo)	10.767 + 0.165* age - 0.00029077* height ² + 0.173* weight	0.881	0.712
FFMI (PCA)	13.288 + 6.962* pc0 + 1.807* pc1 + 2.258* pc2 + 8.859* pc5 + 4.099* pc6 + 9.11* pc15 + 9.64* pc16	0.732	1.069
FFMI (PCA + demo)	10.649 - 3.135* pc10 + 5.363* pc17 + 0.192* age - 0.00028224* height ² + 0.166* weight	0.892	0.679

demo: R² and RMSE were calculated using only demographic variables

PCA: R² and RMSE were calculated using only the PCA coefficients derived from the active shape model

PCA + demo: R² and RMSE were calculated using both PCA & demo.

R² adj: the coefficient of determination adjusted for the number of parameters used in the model equation.

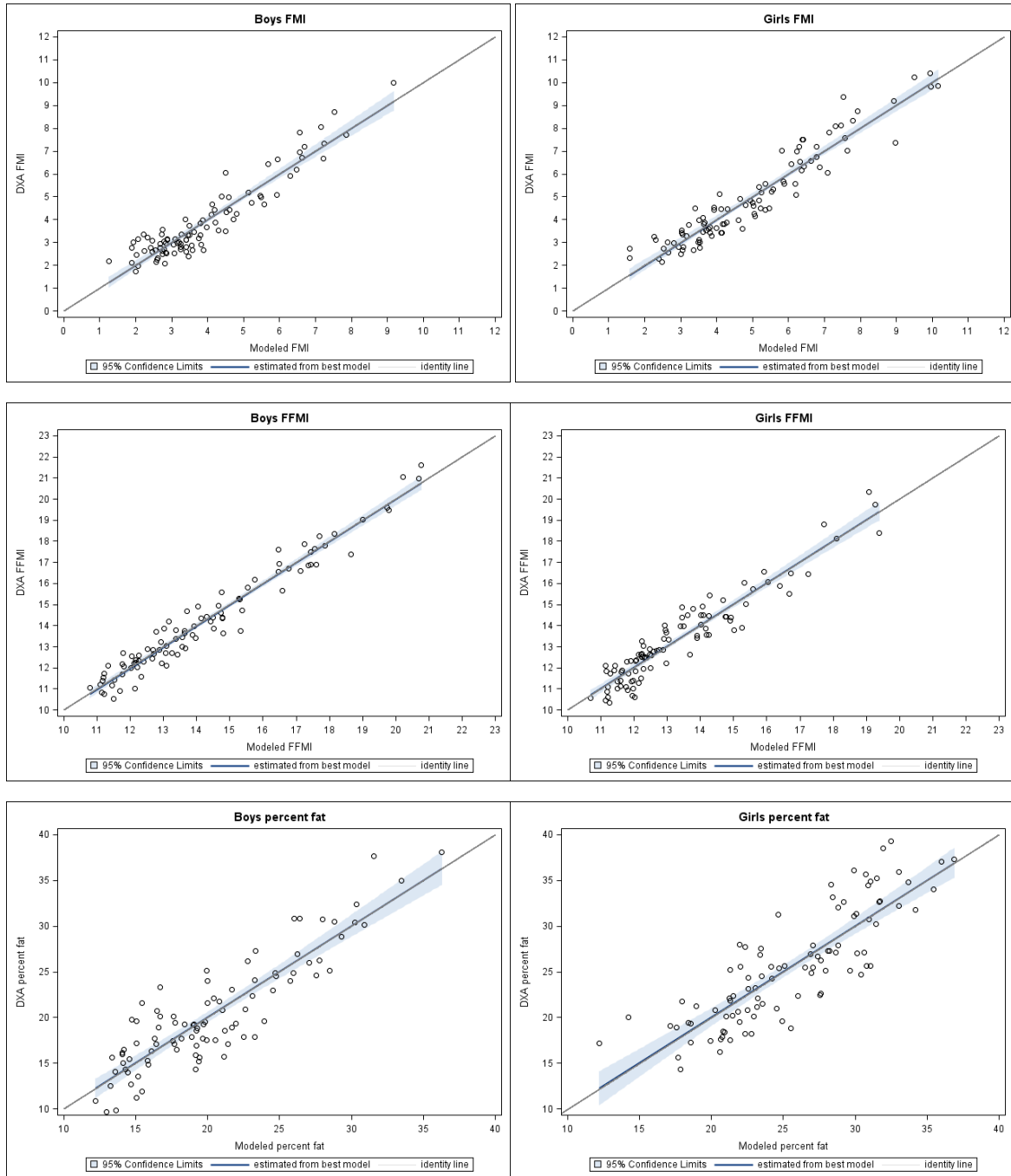


Figure 5.4. Comparison between FMI (top), FFMI (middle), and percent fat (bottom) values acquired from DXA scans and predicted by the PCA models constructed from silhouettes with boys (left) and girls (right). The associated R^2 adj. values are found in Table 3 and 4.

Discussion

In this study, we evaluated the possibility of using silhouettes, or whole body shadow images, to estimate fat and lean body composition indices. We found that the addition of the shape descriptors in the form of principal components did improve on the estimates of body composition over a demographics-alone model for both boys and girls. Additionally, the demographics-only and the PCA-only models had comparable R^2 adj. and RMSE, with the exception of girls' FFMI. Even though these silhouettes were made from DXA whole-body scans, this study suggests that shadow imaging using simpler optical imaging devices, such as simple cell phone cameras, could be used to generate similar silhouettes and associations to body composition. To our knowledge, this is the first study of its kind to show that the shape of silhouettes can be used to quantify body composition measures.

Clearly, some principal components generated by our analysis were related to the positioning of the individual. DXA whole-body scans are acquired with standardized positioning, but the standardization was not intended for direct image registration. It would easily be possible to eliminate many of the positioning variation modes (leg abduction/adduction, torso twisting, arm raising, etc.) if the DXA scans were acquired with this detail in mind. Likewise, for an optical acquisition protocol, positioning of the arms and legs could be more tightly controlled to reduce the contribution of positioning to the overall total variation or omitted if it is found that they provide little to no benefit in the model. In DXA scans, there is a tendency to not repeat a scan if there are minor positioning issues because of radiation exposure.

This study was a pilot demonstration and not intended to be a final model since, ultimately, it is not useful to use DXA images as the primary data source for silhouettes.

Silhouette models should be derived for a specific imaging technology, since magnification and projection differences may change the presentation of the silhouette. The silhouettes used in this study were low spatial resolution compared to cell phone cameras. The DXA-based silhouette images were created with a maximum of 21,800 pixels (1.0 x 6.5 mm² pixel size), or in common camera terminology, the equivalent to a 0.022 megapixel resolution. This resolution is worse than that of the cheapest 640x480 (i.e. 0.31 Megapixel) cell-phone camera. Most current cell phones have cameras with resolution of 1 megapixels or above. Besides spatial resolution, one must also consider the pose (position + orientation) of subjects, their clothing, and the imaging background. These three factors require standardization for optical imaging as it was for the DXA imaging to create a successful ASM. For optical imaging, clothing would have to be thinly layered and fit snugly so as to not significantly alter patients' body outline. In addition, patients should be optically imaged using standardized anatomical positioning to minimize the variance unrelated to body composition (as seen in some of the PCA modes). Unlike DXA, repositioning and re-imaging could be performed repeatedly until an ideal image is acquired. The distance between the imaging plane and the camera would also need to be equivalent across all images. To adjust for differences in optical characteristics of different cameras, a calibration object of known dimensions (e.g. a meter stick or piece of letter-size paper) may be placed coplanar with the subject. Post-acquisition scaling can then be performed to normalize pixel dimensions. Lastly, a "green screen" technique could be used to insure the removal of background was consistent. Given that the above mentioned factors are mitigated, cell phone images should perform equally or better than DXA images for generating silhouettes. The

optical extension of this study could be useful in clinical applications, low resource settings (e.g., point-of-care centers) or when traveling with light equipment is desired (e.g., visiting patients' homes to acquire adiposity measurements). Three-dimensional optical images, such as available from the Microsoft Kinect[104], may be advantageous to 2D images in that they collect more detail on body curvature, especially that curvature that cannot be seen in a silhouette. The strengths and limitations of 2D versus 3D approaches for fitness and nutritional assessment have yet to be explored.

This study had several limitations. First, the participants were imaged in a supine position. We envision that the practical application will use a standing position. Body shape will be different for standing versus supine, but all the concepts derived here should be just as applicable. There is the possibility of over-fitting, given the number of variables included in our models. To address this, we used a cross-validation (leave one out) approach. Ideally, future validations of the optical imaging approach should use separate populations. Additionally, we did not address body shape difference by ethnicity. The sample size for each ethnicity was small. A larger and more diverse sample (separated into ethnicities) will be used in future studies to determine if there are unique body shapes by ethnicity.

We have demonstrated the potential to derive FMI, FFMI, and percent fat estimates from whole body silhouettes that could be useful for the assessment of adiposity and muscularity. The technique presented here may be appropriate to apply to images acquired with simple cell-phone cameras.

Chapter 6 Future Directions

The three-compartment breast technique is still in early development, though it has applications in other modalities as well. The concept of using a three-compartment model for tissue compositions can be applied in dual-energy computed tomography and magnetic resonance imaging as well. There have already been applications in CT by Ding *et al.*[105-107] Since CT has a sweep angle of 180° , the total thickness can be computed easily without any external phantoms. Their studies have shown that it is feasible to apply the 3CB technique to CT. In MRI, the total thickness can also be easily computed, since MRI is also a 3D imaging modality. In addition, chemical composition is already possible with MRI, so water, lipid, and protein signatures can be estimated. 3CB can also be implemented in digital breast tomosynthesis, and preliminary work has been done in this thesis. If it is shown possible to obtain accurate breast thickness estimates from tomosynthesis projections, one would still need to consider performing I_0 corrections, however.

As shown, one limitation of the 3CB technique is how prone it is to errors. It would be valuable to assess the detectability of lesions using the 3CB technique. For X-ray applications, a contrast detail mammography (CDMAM) phantom made from 3CB materials could elucidate 3CB limits. In addition, a separate CDMAM phantom made from biological materials would be even more informative, though precise manufacturing of such a phantom could be impractical.

Recently, investigations combining the 3CB technique and quantitative imaging have revealed promising results for discriminating between benign and malignant

legions during diagnostic imaging. The positive predictive value (PPV) was 32.1% (35 of 109; 95% CI: 23.9% - 41.3%) with a sensitivity of 100% for diagnostic digital mammography and 49% (34 of 70; 95% CI: 36.5% - 58.9%; $p < .001$) with a sensitivity of 97% and 35.8% (39 of 109) fewer total biopsies ($p < .001$) for combined mammography radiomics plus quantitative 3CB image analysis. Further developments could lead to lowering unnecessary breast biopsies.[108]

Chapter 7 Conclusions

The work in this dissertation focused on further developing the three-compartment breast composition technique, initially developed by Laidevant *et al.* in Dr. John Shepherd's Lab, for use in clinical practice. Major efforts were made in correcting sources of error, which initially had impractical compositional thickness estimates. Another major task was to do initial developments for 3CB applications in digital breast tomosynthesis. Lastly, a novel technique for measuring body composition from 2D optical images to help monitor and maintain healthy body weight was covered. The conclusions for each of these works are summarized here.

Three major sources of error were discovered that made the 3CB technique susceptible to incorrect compositional estimates. All three error sources have direct ties to minimizing differences between patient and calibration images; that is, all three sources should be corrected according to specific energies at which 3CB images are acquired. Attenuation coefficient differences in biological materials—for which 3CB is estimating compositional estimates—and their calibration equivalents relied on creating linear mappings between material spaces with bovine and chicken phantoms at specific kVps. Secondly, an empirical flat-fielding model was created to remove nonuniformities in FFDM from X-ray source spectra, making it so that I_0 would be position-independent along the detector plane. Thirdly, both I_0 correction models made it possible to obtain similar log-signal values between breast and calibration images, and both were made for specific kVps. Energy-based errors seemed to have limited the 3CB technique from

becoming clinically practical in FFDM, and efforts should be made to minimize differences between all patient and calibration imaging conditions.

To make the 3CB applicable to DBT, two areas were investigated. Firstly, dose measurements and estimates were made for HE 3CB DBT images. It was found that a copper filter of 0.4064 mm (16 mils) seems to be optimal in terms of meeting dose requirements, availability, and CNR. In addition, imaging at 71 mAs seems to optimize CNR while satisfying dose requirements. Secondly, investigations sought to derive potential variables of interest as predictors of breast thickness from raw DBT projections. It was found that variables derived from sinograms could be potentially useful in estimating breast thickness from raw DBT projections. Though these two efforts have advanced 3CB DBT, there still remain many challenges. Indeed, many efforts will most likely focus on minimizing differences between patient and calibration images.

The last topic discussed in this thesis focused on developing a novel body composition technique from optical images. This proof-of-concept study showed that it may be possible to determine fat mass index, fat-free mass index, and percent-fat from 2D optical images. For breast cancer applications, this could aid in monitoring adipose and muscular tissues to monitor and maintain a lean weight to reduce risk of cancer for postmenopausal women.

In Summary, two of the three major works in this study advanced the 3CB imaging technique to become more clinically practical in dual-energy absorptiometry applications. The last focus of this thesis may make it easier to monitor body composition in low-resource settings.

References

1. Bray, F., et al., *Global cancer statistics 2018: GLOBOCAN estimates of incidence and mortality worldwide for 36 cancers in 185 countries*. 2018.
2. Society, T.A.C. *Early History of Cancer*. The History of Cancer 2014 [cited 2018 12 April 2018]; Available from: <https://www.cancer.org/cancer/cancer-basics/history-of-cancer/what-is-cancer.html>.
3. Ariel, I.M. and J. Cleary, *Breast cancer, a historical review: is the past prologue*. Breast cancer diagnosis and treatment. McGraw-Hill, New York, 1987: p. 3-26.
4. Horsley III, J.S. and G.W. Horsley, *Twenty years' experience with prophylactic bilateral oophorectomy in the treatment of carcinoma of the breast*. Annals of surgery, 1962. **155**(6): p. 935.
5. Lakhtakia, R., *A brief history of breast cancer: Part I: Surgical domination reinvented*. Sultan Qaboos University Medical Journal, 2014. **14**(2): p. e166.
6. Society, A.C. *Breast Cancer Facts and Figures 2017-2018*. 2017 [cited 2018 12/15/2018]; Available from: <https://www.cancer.org/research/cancer-facts-statistics/breast-cancer-facts-figures.html>.
7. Program, I.o.M.C.t.R.t.D.o.D.s.B.C.R., *A Review of the Department of Defense's Program for Breast Cancer Research. Washington (DC) | Chapter 2, Breast Cancer: Biology and Medicine*. 1997: National Academies Press (US).
8. Clinic, M., *Atypical hyperplasia of the breast - Symptoms and causes*. 2018.
9. Fletcher, S.W.J.E.r., *Breast cancer screening: a 35-year perspective*. 2011. **33**(1): p. 165-175.
10. Lerner, B.H.J.C.B.o.M.H., *"To See Today with the Eyes of Tomorrow": A History of Screening Mammography*. 2003. **20**(2): p. 299-321.

11. Kuhl, C.K., et al., *Mammography, breast ultrasound, and magnetic resonance imaging for surveillance of women at high familial risk for breast cancer*. 2005. **23**(33): p. 8469-8476.
12. Prevention, C.f.D.C.a., *Health, United States, 2017, Table 70*. 2017.
13. U.S. Department of Health and Human Services, C.f.D.C.a.P., National Center for Health Statistics, *National Ambulatory Medical Care Survey: 2015 State and National Summary Tables, table 21*. 2015.
14. Prevention, C.f.D.C.a. *Breast Cancer Screening Guidelines for Women*. 2016 [cited 2018 11/14/2018]; Available from:
<https://www.cdc.gov/cancer/breast/pdf/BreastCancerScreeningGuidelines.pdf>.
15. Ebell, M.H., T.N. Thai, and K.J.J.P.h.r. Royalty, *Cancer screening recommendations: an international comparison of high income countries*. 2018. **39**(1): p. 7.
16. Mushlin, A.I., R.W. Kouides, and D.E.J.A.j.o.p.m. Shapiro, *Estimating the accuracy of screening mammography: a meta-analysis*. 1998. **14**(2): p. 143-153.
17. Nelson, H.D., et al., *Screening for breast cancer: an update for the US Preventive Services Task Force*. 2009. **151**(10): p. 727-737.
18. D'Orsi, C.J., *ACR BI-RADS atlas: breast imaging reporting and data system*. 2013: American College of Radiology.
19. Bassett, L.W.J.R.C.o.N.A., *Mammographic analysis of calcifications*. 1992. **30**(1): p. 93-105.
20. Whitehead, J., et al., *Wolfe mammographic parenchymal patterns. A study of the masking hypothesis of Egan and Mosteller*. 1985. **56**(6): p. 1280-1286.
21. Sala, E., et al., *Mammographic parenchymal patterns and mode of detection: implications for the breast screening programme*. 1998. **5**(4): p. 207-212.
22. van Gils, C.H., et al., *Mammographic breast density and risk of breast cancer: masking bias or causality?* 1998. **14**(4): p. 315-320.

23. Knopp, M., et al., *Pathophysiologic basis of contrast enhancement in breast tumors*. 1999. **10**(3): p. 260-266.
24. Tagliafico, A.S., et al., *Diagnostic performance of contrast-enhanced spectral mammography: systematic review and meta-analysis*. 2016. **28**: p. 13-19.
25. Kuhl, C.J.R., *The current status of breast MR imaging part I. Choice of technique, image interpretation, diagnostic accuracy, and transfer to clinical practice*. 2007. **244**(2): p. 356-378.
26. Lobbes, M., et al., *Contrast enhanced mammography: techniques, current results, and potential indications*. 2013. **68**(9): p. 935-944.
27. Stacul, F., et al., *Contrast induced nephropathy: updated ESUR contrast media safety committee guidelines*. 2011. **21**(12): p. 2527-2541.
28. Orel, S.G., et al., *Suspicious breast lesions: MR imaging with radiologic-pathologic correlation*. 1994. **190**(2): p. 485-493.
29. Weinreb, J.C. and G.J.R. Newstead, *MR imaging of the breast*. 1995. **196**(3): p. 593-610.
30. Berg, W.A., et al., *Diagnostic accuracy of mammography, clinical examination, US, and MR imaging in preoperative assessment of breast cancer*. 2004. **233**(3): p. 830-849.
31. Berg, W.A., et al., *Combined screening with ultrasound and mammography vs mammography alone in women at elevated risk of breast cancer*. 2008. **299**(18): p. 2151-2163.
32. Wienbeck, S., J. Lotz, and U.J.C.i. Fischer, *Review of clinical studies and first clinical experiences with a commercially available cone-beam breast CT in Europe*. 2017. **42**: p. 50-59.
33. O'Connell, A.M. and D.J.J.o.c.i.s. Kawakyu-O'Connor, *Dedicated cone-beam breast computed tomography and diagnostic mammography: comparison of radiation dose, patient comfort, and qualitative review of imaging findings in BI-RADS 4 and 5 lesions*. 2012. **2**.
34. Laidevant, A.D., et al., *Compositional breast imaging using a dual-energy mammography protocol*. *Medical physics*, 2010. **37**(1): p. 164-174.

35. Lewin, J.M., et al., *Dual-energy contrast-enhanced digital subtraction mammography: feasibility*. Radiology, 2003. **229**(1): p. 261-268.
36. Shepherd, J.A., et al., *Measurement of breast density with dual X-ray absorptiometry: feasibility*. Radiology, 2002. **223**(2): p. 554-557.
37. Carton, A.-K., et al., *Dual-energy contrast-enhanced digital breast tomosynthesis—a feasibility study*. The British journal of radiology, 2010. **83**(988): p. 344-350.
38. Genant, H.K. and D. Boyd, *Quantitative bone mineral analysis using dual energy computed tomography*. Investigative radiology, 1977. **12**(6): p. 545-551.
39. Lehmann, L., et al., *Generalized image combinations in dual KVP digital radiography*. Medical physics, 1981. **8**(5): p. 659-667.
40. Ding, H., J.L. Ducote, and S. Molloi, *Breast composition measurement with a cadmium-zinc-telluride based spectral computed tomography system*. Medical physics, 2012. **39**(3): p. 1289-1297.
41. Wang, Z.-M., R.N. Pierson Jr, and S.B.J.T.A.j.o.c.n. Heymsfield, *The five-level model: a new approach to organizing body-composition research*. 1992. **56**(1): p. 19-28.
42. Heymsfield, S.B., et al., *Chemical and elemental analysis of humans in vivo using improved body composition models*. 1991. **261**(2): p. E190-E198.
43. Snyder, W., *Report of the task group on reference man*. 1974, Pergamon Press; Oxford.
44. Prince, J.L.L., Jonathan M., *Medical Imaging Signals and Systems*. 2006: Pearson Prentice Hall.
45. Cardinal, H.N. and A. Fenster, *An accurate method for direct dual-energy calibration and decomposition*. Medical physics, 1990. **17**(3): p. 327-341.
46. Kappadath, S.C. and C.C.J.M.P. Shaw, *Dual-energy digital mammography: Calibration and inverse-mapping techniques to estimate calcification thickness and glandular-tissue ratio*. 2003. **30**(6): p. 1110-1117.

47. Laidevant, A.D., et al., *Compositional breast imaging using a dual-energy mammography protocol*. *Medical physics*, 2010. **37**(1): p. 164-174.
48. Drukker, K., et al., *Mammographic quantitative image analysis and biologic image composition for breast lesion characterization and classification*. *Medical Physics*, 2014. **41**(3): p. 031915.
49. Malkov, S., et al., *Compositional Three-Component Breast Imaging of Fibroadenoma and Invasive Cancer Lesions: Pilot Study*, in *Breast Imaging*. 2014, Springer. p. 109-114.
50. Avila, J., et al., *Energy dependence of water and lipid calibration materials for three-compartment breast imaging*, in *Breast Imaging*. 2016, Springer.
51. Malkov, S., et al. *Calibration procedure of three component mammographic breast imaging*. in *International Workshop on Digital Mammography*. 2016. Springer.
52. Avila, J., et al. *Energy Dependence of Water and Lipid Calibration Materials for Three-Compartment Breast Imaging*. in *International Workshop on Digital Mammography*. 2016. Springer.
53. Malkov, S., et al., *Single x-ray absorptiometry method for the quantitative mammographic measure of fibroglandular tissue volume*. *Medical physics*, 2009. **36**(12): p. 5525-5536.
54. Seibert, J.A., J.M. Boone, and K.K. Lindfors. *Flat-field correction technique for digital detectors*. in *Medical Imaging 1998: Physics of Medical Imaging*. 1998. International Society for Optics and Photonics.
55. Kwan, A.L., J.A. Seibert, and J.M.J.M.p. Boone, *An improved method for flat-field correction of flat panel x-ray detector*. 2006. **33**(2): p. 391-393.
56. Dobbins, J.T.J.M.p., *Tomosynthesis imaging: at a translational crossroads*. 2009. **36**(6Part1): p. 1956-1967.

57. Hu, Y.H., B. Zhao, and W.J.M.p. Zhao, *Image artifacts in digital breast tomosynthesis: Investigation of the effects of system geometry and reconstruction parameters using a linear system approach*. 2008. **35**(12): p. 5242-5252.
58. Gilbert, F., et al., *The TOMMY trial: a comparison of TOMosynthesis with digital MammographyY in the UK NHS Breast Screening Programme-a multicentre retrospective reading study comparing the diagnostic performance of digital breast tomosynthesis and digital mammography with digital mammography alone*. 2015.
59. Gilbert, F.J., L. Tucker, and K.C.J.C.r. Young, *Digital breast tomosynthesis (DBT): a review of the evidence for use as a screening tool*. 2016. **71**(2): p. 141-150.
60. Michell, M., et al., *A comparison of the accuracy of film-screen mammography, full-field digital mammography, and digital breast tomosynthesis*. 2012. **67**(10): p. 976-981.
61. Nosratieh, A., et al., *Mean glandular dose coefficients (DgN) for x-ray spectra used in contemporary breast imaging systems*. 2015. **60**(18): p. 7179.
62. van Aarle, W., et al., *Fast and flexible X-ray tomography using the ASTRA toolbox*. 2016. **24**(22): p. 25129-25147.
63. van Aarle, W., et al., *The ASTRA Toolbox: A platform for advanced algorithm development in electron tomography*. 2015. **157**: p. 35-47.
64. De Pergola, G. and F.J.J.o.o. Silvestris, *Obesity as a major risk factor for cancer*. 2013. **2013**.
65. Carmichael, A.R. and T.J.T.B. Bates, *Obesity and breast cancer: a review of the literature*. 2004. **13**(2): p. 85-92.
66. Lorincz, A. and S.J.E.-r.c. Sukumar, *Molecular links between obesity and breast cancer*. 2006. **13**(2): p. 279-292.
67. Cleary, M.P. and M.E.J.E. Grossmann, *Obesity and breast cancer: the estrogen connection*. 2009. **150**(6): p. 2537-2542.

68. Simone, V., et al., *Obesity and breast cancer: molecular interconnections and potential clinical applications*. 2016: p. theoncologist. 2015-0351.
69. Xie, B., et al., *Accurate body composition measures from whole-body silhouettes*. 2015. **42**(8): p. 4668-4677.
70. Hossain, P., B. Kavar, and M. El Nahas, *Obesity and diabetes in the developing world--a growing challenge*. N Engl J Med, 2007. **356**(3): p. 213-5.
71. Kennedy, G., G. Nantel, and P. Shetty, *Assessment of the double burden of malnutrition in six case study countries*. FAO Food and Nutrition Paper (FAO), 2006.
72. Ohlson, L.-O., et al., *Risk factors for type 2 (non-insulin-dependent) diabetes mellitus. Thirteen and one-half years of follow-up of the participants in a study of Swedish men born in 1913*. Diabetologia, 1988. **31**(11): p. 798-805.
73. Weber, D.R., et al., *A Comparison of Fat and Lean Body Mass Index to BMI for the Identification of Metabolic Syndrome in Children and Adolescents*. The Journal of Clinical Endocrinology & Metabolism, 2014. **99**(9): p. 3208-3216.
74. Stern, M.P. and S.M. Haffner, *Body fat distribution and hyperinsulinemia as risk factors for diabetes and cardiovascular disease*. Arteriosclerosis, 1986. **6**(2): p. 123-30.
75. Goodpaster, B.H., et al., *Subcutaneous abdominal fat and thigh muscle composition predict insulin sensitivity independently of visceral fat*. Diabetes, 1997. **46**(10): p. 1579-85.
76. Wang, Y., et al., *Comparison of abdominal adiposity and overall obesity in predicting risk of type 2 diabetes among men*. Am J Clin Nutr, 2005. **81**(3): p. 555-63.
77. Wells, J.C. and M.S. Fewtrell, *Measuring body composition*. Arch Dis Child, 2006. **91**(7): p. 612-7.
78. Wells, J.C., *A Hattori chart analysis of body mass index in infants and children*. Int J Obes Relat Metab Disord, 2000. **24**(3): p. 325-9.

79. Baumgartner, R.N., S.B. Heymsfield, and A.F. Roche, *Human body composition and the epidemiology of chronic disease*. *Obes Res*, 1995. **3**(1): p. 73-95.
80. Must, A. and S. Anderson, *PEDIATRIC MINI REVIEW Body mass index in children and adolescents: considerations for population-based applications*. *International journal of obesity*, 2006. **30**: p. 590-594.
81. Park, H.W., et al., *Adolescent Build Plotting on Body Composition Chart and the Type of Diabetes Mellitus*. *Journal of Korean medical science*, 2012. **27**(11): p. 1385-1390.
82. Campbell, T.M. and L.A. Vallis, *Predicting fat-free mass index and sarcopenia in assisted-living older adults*. *Age*, 2014. **36**(4): p. 1-13.
83. Kyle, U.G., et al., *Bioelectrical impedance analysis--part II: utilization in clinical practice*. *Clin Nutr*, 2004. **23**(6): p. 1430-53.
84. Kyle, U.G., et al., *Bioelectrical impedance analysis--part I: review of principles and methods*. *Clin Nutr*, 2004. **23**(5): p. 1226-43.
85. Hattori, K., et al., *Chart analysis of body composition change among pre-and postadolescent Japanese subjects assessed by underwater weighing method*. *International journal of obesity*, 2004. **28**(4): p. 520-524.
86. Vescovi, J.D., et al., *Evaluation of the BOD POD for estimating percentage body fat in a heterogeneous group of adult humans*. *Eur J Appl Physiol*, 2001. **85**(3-4): p. 326-32.
87. Sheng, H.P. and R.A. Huggins, *A review of body composition studies with emphasis on total body water and fat*. *Am J Clin Nutr*, 1979. **32**(3): p. 630-47.
88. Wells, J.C.K., et al., *Prediction of total body water in infants and children*. *Archives of Disease in Childhood*, 2005. **90**(9): p. 965-971.
89. Kalkwarf, H.J., et al., *The bone mineral density in childhood study: bone mineral content and density according to age, sex, and race*. *J Clin Endocrinol Metab*, 2007. **92**(6): p. 2087-99.

90. Zemel, B.S., et al., *Revised reference curves for bone mineral content and areal bone mineral density according to age and sex for black and non-black children: results of the bone mineral density in childhood study*. The Journal of clinical endocrinology and metabolism, 2011. **96**(10): p. 3160-9.
91. Weber, D.R., et al., *Fat and lean BMI reference curves in children and adolescents and their utility in identifying excess adiposity compared with BMI and percentage body fat*. The American journal of clinical nutrition, 2013. **98**(1): p. 49-56.
92. Snijder, M.B., et al., *Associations of hip and thigh circumferences independent of waist circumference with the incidence of type 2 diabetes: the Hoorn Study*. Am J Clin Nutr, 2003. **77**(5): p. 1192-7.
93. Nordhamn, K., et al., *Reliability of anthropometric measurements in overweight and lean subjects: consequences for correlations between anthropometric and other variables*. International journal of obesity and related metabolic disorders : journal of the International Association for the Study of Obesity, 2000. **24**(5): p. 652-657.
94. Sampaio, L.R., et al., *Validity and reliability of the sagittal abdominal diameter as a predictor of visceral abdominal fat*. Arquivos Brasileiros de Endocrinologia & Metabologia, 2007. **51**: p. 980-986.
95. Risérus, U., et al., *Sagittal abdominal diameter is a strong anthropometric marker of insulin resistance and hyperproinsulinemia in obese men*. Diabetes care, 2004. **27**(8): p. 2041-2046.
96. Pouliot, M.-C., et al., *Waist circumference and abdominal sagittal diameter: best simple anthropometric indexes of abdominal visceral adipose tissue accumulation and related cardiovascular risk in men and women*. The American journal of cardiology, 1994. **73**(7): p. 460-468.

97. Janssen, I., P.T. Katzmarzyk, and R. Ross, *Waist circumference and not body mass index explains obesity-related health risk*. The American journal of clinical nutrition, 2004. **79**(3): p. 379-384.
98. Finbråten, A.K., et al., *Assessment of body composition in children with cerebral palsy: a cross-sectional study in Norway*. Developmental Medicine & Child Neurology, 2015.
99. Prevention, C.f.D.C.a. *A SAS Program for the 2000 CDC Growth Charts (ages 0 to <20 years)*. January 13, 2014 [cited 2014 February 2]; Available from:
<http://www.cdc.gov/nccdphp/dnpao/growthcharts/resources/sas.htm>.
100. Shepherd, J.A., et al., *A multinational study to develop universal standardization of whole-body bone density and composition using GE Healthcare Lunar and Hologic DXA systems*. Journal of Bone and Mineral Research, 2012. **27**(10): p. 2208-2216.
101. Wilson, J.P., et al., *Dual-energy X-ray absorptiometry-based body volume measurement for 4-compartment body composition*. The American journal of clinical nutrition, 2012. **95**(1): p. 25-31.
102. Cootes, T.F., et al., *Active Shape Models-Their Training and Application*. Computer Vision and Image Understanding, 1995. **61**(1): p. 38-59.
103. Gregory, J.S., et al., *Early identification of radiographic osteoarthritis of the hip using an active shape model to quantify changes in bone morphometric features: can hip shape tell us anything about the progression of osteoarthritis?* Arthritis & Rheumatism, 2007. **56**(11): p. 3634-3643.
104. Tong, J., et al., *Scanning 3d full human bodies using kinects*. Visualization and Computer Graphics, IEEE Transactions on, 2012. **18**(4): p. 643-650.
105. Ding, H., et al., *Breast tissue characterization with photon-counting spectral CT imaging: a postmortem breast study*. 2014. **272**(3): p. 731-738.
106. Ding, H., J.L. Ducote, and S.J.M.p. Molloi, *Breast composition measurement with a cadmium-zinc-telluride based spectral computed tomography system*. 2012. **39**(3): p. 1289-1297.

107. Ding, H., et al., *Breast tissue decomposition with spectral distortion correction: A postmortem study*. 2014. **41**(10).
108. Drukker, K., et al., *Combined Benefit of Quantitative Three-Compartment Breast Image Analysis and Mammography Radiomics in the Classification of Breast Masses in a Clinical Data Set*. 2018.

Appendix A: Code Availability

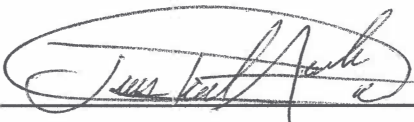
Several software tools and analysis scripts were developed over the course of this dissertation. These pieces of code are maintained in secure repositories on the Shepherd Lab GitHub (<https://github.com/shepherd-lab>). A listing of relevant repositories is provided below. Please direct inquiries to Jesus Avila (jjavila@berkeley.edu) or John Shepherd (johnshep@hawaii.edu).

- **3CB Repository** (https://github.com/shepherd-lab/3c_sxa)
 - MATLAB scripts for automatic processing and reprocessing of 3CB patients for estimating water, lipid, and protein thicknesses of breast lesions annotated by radiologists.
 - ASTRA *Toolbox* scripts in MATLAB for simulating and estimating breast thickness

Publishing Agreement

It is the policy of the University to encourage the distribution of all theses, dissertations, and manuscripts. Copies of all UCSF theses, dissertations, and manuscripts will be routed to the library via the Graduate Division. The library will make all theses, dissertations, and manuscripts accessible to the public and will preserve these to the best of their abilities, in perpetuity.

I hereby grant permission to the Graduate Division of the University of California, San Francisco to release copies of my thesis, dissertation, or manuscript to the Campus Library to provide access and preservation, in whole or in part, in perpetuity.

Author Signature  Date 28 Dec. 2018